Stian Kjønniksen Gaustad

Introduction of Rhenium to surface modified microporous and mesoporous materials.

May 2020

Master's thesis

2020

Master's thesis

Stian Kjønniksen Gaustad

NTNU
Norwegian University of
Science and Technology
Faculty of Natural Sciences
Department of Chemistry

NTNU
Norwegian University of
Science and Technology

NTNU
Norwegian University of
Science and Technology

NTNU

**Norwegian University of
Science and Technology**

Introduction of Rhenium to surface modified microporous and mesoporous materials.

Stian Kjønniksen Gaustad

Acknowledgement

Sammendrag

Et utvalg av ulike mikro- og mesopørse bærermaterialer var syntetisert og modifisert med en organosilan for å introdusere en aminopropylgruppe på innsiden av de porøse materialene. Den introduserte aminopropylgruppen var vellykket som at anker for rhenium. Overflate modifiseringen var vellykket for alle mesoporøse materialer, men flere av de mikroporøse var ikke vellykket. Suksessen hos de mesoporøse materialene var ble regnet som en følge av at den store porestørrelsen ikke hindret reaksjon med organosilane, men problemet for de mikroporøse materialene var enten for små porere for organosilane eller uegnede overflategrupper i materialet.

Rhenium ble introdusert via oppløsning av Re_2O_7 i toluene og introdusere til de modifiserte materialene med denne løsningen. Den beste bæreren oppnådde $9.4\,wt.\%$ rhenium i materialet. Valg av de porøse bærermaterialane virket ikke å ha noen påvirking på det introduserte rheniumet. Benyttet metode kan tilpasses for andre porøse materialer med liten anstrengelse, forutsatt at de har en passende porestørrelse og ikke inneholder brønsted-syresteder

Materialer var karakterisert via flere forskjellige metoder for å undersøke bærermaterialenes egenskaper, effekt av overflate modifiseringen, og effekten av effekten rhenium introduksjon på systemene. Røntgenstrålediffraksjon ble brukt for å bekrefte fasen for de ulike materialene, adsorpsjons-desorpsjonsmålinger ble brukt for å undersøke påvirkning på overflate areal, og ICP-MS ble brukt for å påvise mengden rhenium introdusert til materialene. XAS ble utført for å undersøke det lokale kjemiske miljøet rundt det introduserte rheniumet.

Abstract

A variety of porous micro and mesoporous materials was successfully synthesized, and modified with an organosilane to introduce a aminopropyl group inside the pore network. The introduced aminopropyl was successfully used as a rhenium anchor. All mesoporous materials tested appear suited to this modification, while only some of the microporous materials was successfully modified. The success of mesoporous materials was attributed to their large pore size not limiting the organosilane modification while the failure in some microporous materials was attributed to either too small pores for the organosilane or unsuited surface groups.

Rhenium was introduced to the modified materials through a toluene solution with Re_2O_7 dissolved. The resulting rhenium loading in the materials was up to 9.4 wt.%. The chemical speciation of introduced rhenium appears to be completely independent of the porous material used. The method used could be adapted for other porous materials with little effort, assuming they have a suitable pore size and does not contain brønsted acid sites.

Multiple characterization techniques was used to determine properties of the varies materials and the impact of the rhenium introduction as well as the organosilane modification. X-ray diffraction was used to confirmed the phase of materials, adsorption-desorption measurements was used to investigate impact on surface areas, and ICP-MS was used to detect amount of rhenium retained by the modified materials. XAS was performed to investigate speciation of introduced rhenium.

Contents

Abbreviations

λ -   Wavelength of electromagnetic radiation

θ -   Incident angle of electromagnetic radioation.

A5   -   A sample composed of the zeotype AlPO-5

ACN   -   Acetonitrile

AFAC   -   Amplitude reduction factor

AFI   -   A crystallographic frameworktype corresponding to various zeotypes, e.g. SAPO-5

AlPO   -   Aluminophosphate, a class of zeotypes

AP   -   3-aminopropyl

APD   -   Ambient pressure drying

APTES   -   (3-Aminopropyl)triethoxysilane

BET   -   Method for adsorption surface area determination developed by Brunauer, Emmett, and Teller

BJH   -   Method for pore size determination developed by Barret, Joyner, and Halenda

CBU   -   Composite building unit for zeolitic materials, also known as tertiary unit

CHA   -   Chabazite, a mineral with the same diffraction pattern as SAPO-34

COD   -   Crystallography Open Database, a collection of diffraction patterns

CTAB   -   Cetyltrimethylammonium bromide

DSC   -   Differential scanning calorimetry

E_0 -   Threshold for adsorption energy

E_F -   Fermi energy

EXAFS   -   Extended X-ray adsorption fine structure

HMDS   -   hexamethyldisilazane

HMDSO   -   Hexamethyldisiloxane

IUPAC   -   International Union of Pure and Applied Chemistry

IUPAC   -   International Union of Pure and Applied Chemistry

LCF   -   Linear combination fitting

LN-MCT   -   A IR detector composed of liquid nitrogen cooled mercury cadmium telluride (HgCdTe)

MCM-41   -   A ordered silica material

MFI   -   A crystallographic frameworktype corresponding to various zeolites, e.g. ZSM-5

P123   -   Pluronic P123, Poly(ethylene glycol)-*block*-poly(propylene glycol)-*block*-poly(ethylene glycol)

PBU   -   Primary building unit for zeolitic materials

PDF   -   Powder Diffraction File, diffraction pattern from the International Center for Diffraction Data

PXRD   -   Powder X-ray diffraction

S1   -   A sample composed of the zeolite Silicalite-1

S15   -   A sample composed of SBA-15

S5   -   A sample composed of the zeotype SAPO-5

SA   -   Silicic Acid

SAG   -   Silica Aerogel

SAPO   -   Silicoaluminophophate, a class of zeotypes

SBA-15   -   A ordered silica material

SBU   -   Secondary building unit for zeolitic materials

SCD   -   Supercritical drying

SCXRD   -   Single crystal X-ray diffraction

SDA   -   Structure Directing Agent

SEM   -   Scanning Electron Microscopy

SXG   -   Silica Xerogel

TEA   -   Triethylamine, NEt_3

TEOS   -   Tetraethyl orthosilicate

TGA   -   Thermogravimetric analysis

TGA/MS   -   Thermogravimetric analysis coupled with a mass spectrometer

XANES   -   X-ray adsorption near edge structure

XAS   -   X-ray adsorption spectroscopy

XRD   -   X-ray diffraction

1. Motivation

Research into new catalysts and improvement of current catalysts are vital for reduction of energy cost and pollution from the chemical industry. In the search for new cost-effective catalysts the investigation into uncommon and often expensive metals is highly valuable. Among these promising metals is rhenium, a less used catalytically active metal known about for almost a century. [1,2]

Several catalytic applications of rhenium are through bimetallic catalysts where rhenium acts as a promoter, for example the Re-Co catalysts which is used for hydrogenation of CO. [3] Re-Pt bimetallic catalysts are used for dehydrogenation of cyclohexane to benzene, and conversion of petrol fractions into high-octane petrols. [4,5]

Various forms of rhenium is also viable catalysts on their own. Rhenium oxides like Re_2O_7 show activity for olefin metathesis, [6] while supported ReOx show activity for selective oxidation of methanol to methylal [7] and benzene to phenol. [8] Metallic nanoparticles of Re have shown high activity for the ammonia synthesis, a highly energy consuming process. [9] A unique benefit of Re as a catalyst is the resistance to phosphorus and sulphur poisoning, increasing cost-effectiveness if the feedstock is contaminated with phosphorus or sulphur. [2]

The potential usage for rhenium in catalysis is offset by the high cost. Rhenium composes a very small amount of the earth's crust diffusely spread in a lot of different minerals. [10] Rhenium having several important applications and it's scarcity contribute to it's high cost. To offset the high cost and reduce amount of this scarce metal supporting rhenium on a suitable catalyst support is common. The introduction is usually performed by impregnation, [6] the common material to support rhenium are alumina and silica. [9,11–13] Utilization of supported catalysts also allow control over important features in catalysts like improving lifetime of the catalyst, introducing selectivity to the catalyst, and facilitating formation of smaller particles of the catalyst material.

1

The detriment to rhenium catalysts is that the production of heterogeneous rhenium-containing catalysts prove challenging due to the solubility of rhenium with several solvents. These issues make introduction of rhenium through wet impregnation and ion exchange challenging, a significant downside as methods like ion exchange are quite cheap and easy to scale up.

Tafjord[14] attempted to introduce Re_2O_7 to a variety of porous supports via ion-exchange and incipient wetness methods, a complication of the introduction was rhenium's high affinity for its solvents. In the ion-exchange the water proved a unsuited solvent due to negligible rhenium retention. Acetone and ethanol was also investigated as ion-exchange solvents, acetone had negligible results like the water, while ethanol showed some uptake the relative loading remained low for several samples. Tafjord[14] did have successful introduction of rhenium through incipient wetness (also known as dry impregnation).

In this master thesis an attempt is made to solve the issues Tafjord[14] encountered with low rhenium retention with his ion-exchanged samples by introduction of a "anchor" site inside the pore system of various porous materials. As rhenium show high affinity for amines a post-synthetic approach with amine-containing organosilanes as "anchor" groups would hypothetically retain a majority of introduced rhenium, potentially leading to viable heterogeneous rhenium catalysts. The post-synthetic approach using organosilanes should also make any results transferable to similar systems.

In other works organosilane modification to similar porous materials have been performed, and utilized as intermediate modification steps or as adsorbents for heavy metals or CO_2.[15–17] Rhenium has also been attached to some rhenium complexes by aminopropyl-modified silica nanoparticles.[18] Combining these methods with introduction of Re_2O_7 could potentially make a highly stable, active, and reuseable catalyst, with possibility of reactant size selectivity through variation of the porous support. The primary goal of this thesis was investigating stability of post-synthetic aminopropyl modified porous supports as carriers of ReOx, and the impact of the porous support materials pore size, surface area, and surface chemistry.

2. Theory

2.1 Rhenium

Rhenium was the last stable, non-radioactive, naturally-occurring element to be discovered. Rhenium was first isolated by Noddack and Tacke from Gadolinite in 1925.[1] Rhenium is considered among the rarest metals on Earth, sparsely spread throughout the Earth's crust and is commonly extracted through flue dust from molybdenium smelters.[19]

Most of the worlds refined rhenium is used in alloys, especially in nickel alloys. The addition of rhenium allows "superalloys", also known as high-performance alloys, to operate close to the melting point for longer by slowing diffusion, creep deformation, and fatigue crack initiation.[20,21] Even though the mechanism behind the "Rhenium effect" is still debated some explanations like the very slow diffusion rate and interfacial dislocation interactions with Re appears to show merit.[22,23]

Rhenium is used in both superalloys, which are alloys that can operate at temperatures close to their melting point, and in catalysis.[20] Addition of Re into superalloys is used to strengthen and increase high temperature operation, though the mechanism behind the "Rhenium effect" is still debated some explanations like the very slow diffusion rate and interfacial dislocation interactions with Re appear show some merit.[22,23]

Several catalytic applications of Re are through bimetallic catalysts where Re acts as a promoter, for example the Re-Co catalysts which is used for hydrogenation of CO.[3] Re-Pt bimetallic catalysts are used for dehydrogenation of cyclohexane to benzene, and conversion of petrol fractions into high-octane petrols.[4]

Rhenium oxides like Re_2O_7 show activity for olefin metathesis,[6] while supported ReOx show activity for selective oxidation of methanol to methylal[7] and benzene

3

to phenol.[8] Metallic nanoparticles of Re also show high activity for ammonia synthesis, a highly energy consuming process.[9] A unique benefit of Re as a catalyst is the resistance to phosphorus and sulphur poisoning, increasing cost-effectiveness if the feedstock is contaminated with phosphorus or sulphur.[2]

The potential usage for rhenium in catalysis is offset by the high cost. Rhenium composes a very small amount of the earth's crust, roughly 0.7 ppb, diffusely spread throughout over 300 minerals.[10] Rhenium having several important applications and it's scarcity contribute to it's high cost. To offset the high cost and reduce amount of this scarce metal supporting rhenium on a suitable catalyst support is beneficial. Utilization of supported catalysts also allow control over important features in catalysts like improving lifetime of the catalyst, introducing selectivity to the catalyst, and facilitating formation of smaller particles of the catalyst material.

2.2 Microporous and Mesoporous materials

The properties of any heterogeneous catalysts support material is of great importance. The lifetime of a catalyst can be lengthened by choosing the most appropriate support which could prevent coke formation in the pore network by preventing physical deposition of certain species in the pores.[24] Optimizing the stability of the support to intended reaction is also important to minimize deactivation due to sintering or attrition of the catalyst system.[24]

The chemical environment in the catalyst support materials is also important to control. Strong interaction between metal catalyst and the support would stabilize smaller particles, by stabilizing the high surface energy, and in some cases the metal-support interaction has direct impact on the catalytic activity of certain species.[25,26] Reaction selectivity can also be achieved using certain support materials, either though enhancing a specific reaction pathway by the metal-support interaction or by physical limitation of reagents, intermediates, and products by choosing pore size that only allow permit certain molecules to enter/leave.[27,28]

The various porous materials used in this project is described later in this section, and summarized in Table 2.1. Porous materials have three classifications based on their pore sizes defined by IUPAC, micropores are defined as pores with width$<$2 nm, mesopores are defined as pores within $2\,\text{nm}<\text{width}<50\,\text{nm}$, while macropores are defined as any pores with width$>$50 nm.[29]

Table 2.1: Overview of pore systems, pore sizes, and unique properties of the various support materials synthesized and used in this thesis.

Name	Pore system	Pore Size (nm)	Special properties
Silicalite-1	Microporous, small	0.53x0.57	
AlPO-5	Microporous, large	0.73	
SAPO-5	Microporous, large	0.73	Brønsted Acid sites
Silica Xerogel	Microporous	2≤	
Silica Aerogel	Micro- and mesoporous	6-35^a	
SBA-15	Mesoporous	4-15	

^{a}For the mesopores, micropores similar to that of Silica Xerogel

2.2.1 Zeolites and zeotypes

Zeolites are a class of microporous and crystalline materials containing aluminium and silicon. Zeolites are defined as crystalline aluminosilicates, structures containing elements other than aluminium, silicon, and oxygen are called zeotypes, and are structural analogs to corresponding zeolites. Zeolites structure is formed by Si or Al bonded in a tetrahedra with oxygen.[30]

The tetrahedrally coordinated cations are called T-atoms with oxygen's forming bridges between these T-atoms. The structural units of zeolites and zeotypes are divided into three, the smallest is the primary building unit (PBU), [TO$_4$], where T is either Si or Al.

Combinations of PBU's are called secondary building units (SBU) which are larger structures composed of one type of PBU repeating in space. The composite building units (CBU) are the largest units.[31] The pore shape and size of zeolites and zeotypes depend on their SBU's and CBU's. A variety of PBU's, CBU's and a few zeolite structures is illustrated in Figure 2.1

Zeolites and zeotypes can have the same framework and topology while possessing different elemental compositions. Zeolites with the same framework share topology, pore size, and pore volume. The various zeolite frameworks are represented by a 3-letter code, e.g. CHA or AFR.[33,34]

Introduction of other tetrahedral PBU's produce zeotypes. A zeotypes consisting of [AlO$_4$] and [PO$_4$] tetrahedras are known as aluminophosphates (AlPO), where the [Al-O-P] bridges form the SBU's. The alternating Al and P introduce a charge distribution in the network while maintaining a neutral framework. Introduction
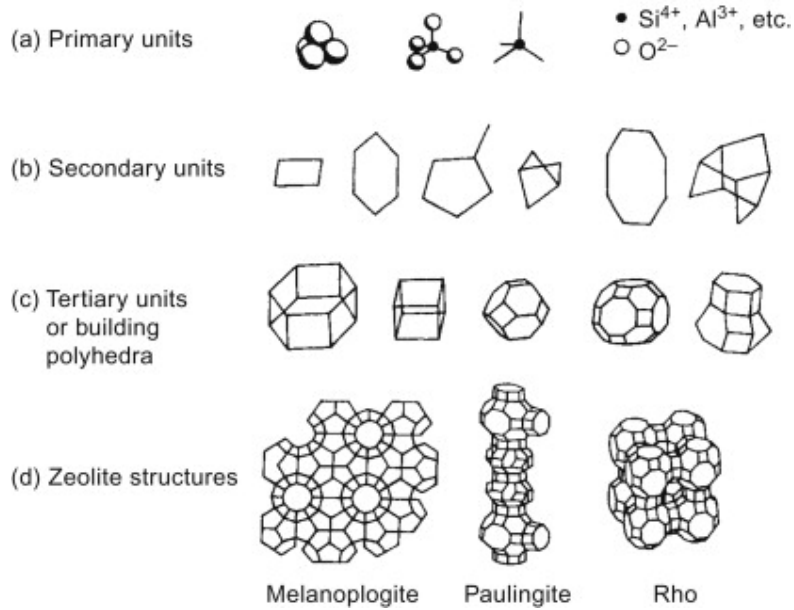
Figure 2.1: Composition of zeolite stuctures with illustrations of the primary, secondary and tertiary units. Reused with permission Qinhua and Aizhen[32].

of $[SiO_4]$ to a neutral AlPO framework results in a silicoaluminophophate (SAPO), the charge generated by the substitution is compensated by protons in brønsted acid sites.[30]

The added silicon is introduced into the AlPO in three possible mechanisms; by replacing a phosphorus with a silicon, replacing a aluminium with a silicon, or replacing two adjacent aluminium and phosphorus with two silicons.[35] Due to the overall negative charge of SAPO frameworks, replacement of phosphorus with silicon is the main mechanism while replacement of adjacent aluminium and phosphorus with silicon can occur in certain conditions.[36]

During synthesis the formation of pores and cages in the zeolite framework is facilitated by bulky organic molecules, often amines, called structure directing agents (SDA). After synthesis and crystallization the SDA is usually removed from the poresystem by calcination at high temperatures.

AFI framework

The AFI framework, illustrated in 2.2(a), contain a 1D pore structure of straight, parallel pores. The pores are formed by 12-PBUs, and have a diameter of 0.73 nm.[33] The AFI framework is found in both the SAPO-5 and AlPO-5 zeotypes.
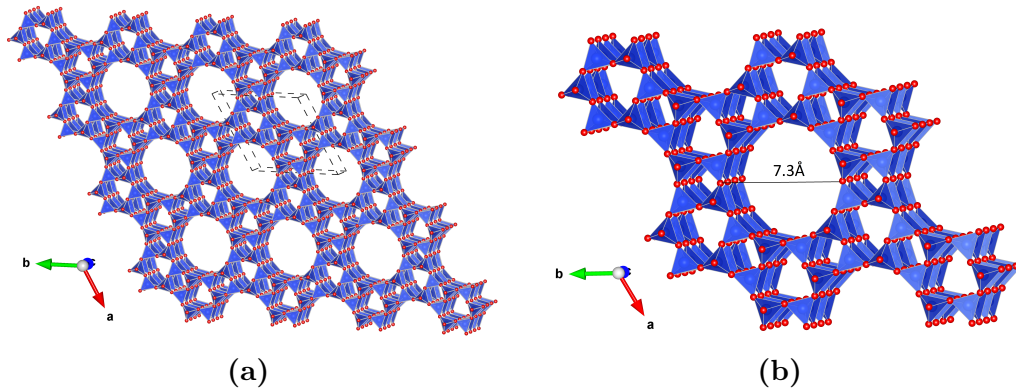

Figure 2.2: VESTA illustration of the AFI type framework. a) The pore system of the AFI framework with crystal unit cell marked. b) Pore dimension of the AFI framework.

In this work both SAPO-5 and AlPO-5 will be used as a support material, so that different behaviour between SAPO-5 and AlPO-5 can be attributed to the presence of brønsted acidity only found in the SAPO-5.

MFI framework

The MFI framework, illustrated in Figure 2.3, contain both straight parallel pores and perpendicular sinusoidal pores, where the perpendicular sinusoidal pores form bridges between two adjacent straight pores. The straight pores have a size of 0.54×0.56 nm. Notable zeolites possessing the MFI-type framework is ZSM-5 and Silicalite-1.

In this work only the silicalite-1 will be used from the MFI framework group of materials. The silicalite-1 will provide insight into the effect of small, straight, interconnected pores for the post-synthetic modification, in contrast to the small, irregular pore shape of the silica xerogel.
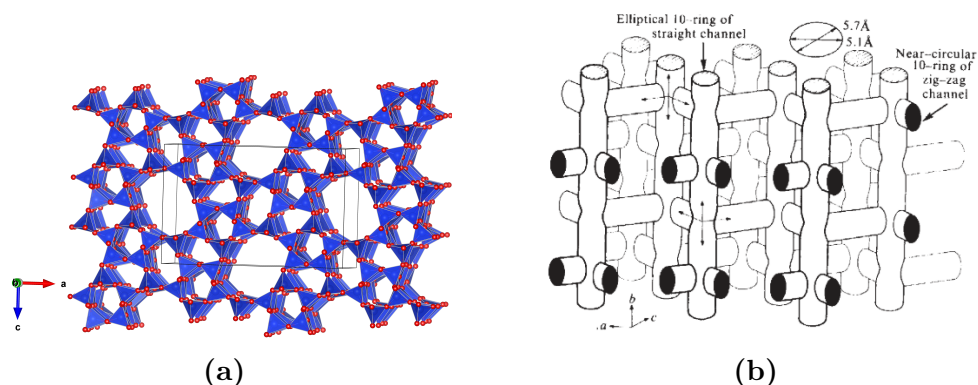
(a)   (b)

Figure 2.3: a) VESTA illustration of the MFI type framework. b) Illustration of the Silicalite-1 structure showing both the straight and the sinusoidal pores. Reused with permission [37]

2.2.2 SBA-15

SBA-15 is a ordered silica material, with 1-dimensional mesopores in the range of 50-300 Å and a high surface area (600-1000 $m^2\,g^{-1}$), the SBA-15 pore structure is illustrated in Figure 2.4. SBA-15 is usually synthesized by using the amphiphilic triblockpolymer $PEtO_{20}-PPrO_{70}-PEtO_{20}$ (Poly(ethylene glycol)-*block*-poly(propylene glycol)-*block*-poly(ethylene glycol)), commonly known as Pluronic P123, as a template in acidic media. [38] The silica structure is formed by self-assembly of silica-surfactant species with simultaneous condensation of the inorganic species. [38] Utilizing additives and/or co-surfactants alter the particle morphology, while varying synthesis conditions (e.g. temperature) impact pore size, wall thickness, and surface area. [39,40] SBA-15 also have high hydrothermal stability due to increase wall thickness compared to similar materials like the MCM-41. [41] The high hydrothermal stability and customizable pore properties makes the SBA-15 a versatile material with multiple potential applications.

Commonly the SBA-15 has no Brønsted acidity, as the structure is entirely made of $[SiO_4]$ tetrahedrons. However it is possible to create a SBA-15 doped with Aluminium, [43] which adds Brønsted acidity to the SBA-15 due to the same mechanism as in the SAPO-5 covered in 2.2.1.
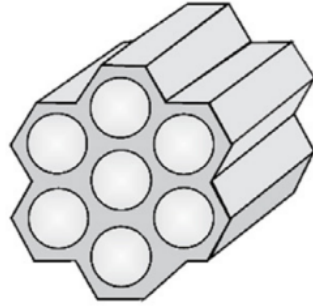
8

Figure 2.4: An illustration of the mesoporous SBA-15 material. Reused with permission Pinto *et al.*[42].

2.2.3 Silica Aerogels and Xerogels

Silica aerogels are a class of materials composed of a micro- and mesoporous gel where the dispersed phase is replaced by a gas.[44] A similar structure to the aerogel is the xerogel where the gel structure collapse after removal of the swelling agent.[45] A silica aerogels was first synthesized in 1931 by Kistler[46], who demonstrated that the gel structure was independent of the liquid phase. Silica aerogels are used for multiple applications, like as an adsorbent, as a sensor, or as a catalyst carrier.[47] Silica xerogels on the other hand has been known since the 1600s, commonly refered to as silica gel, with its first practical application in 1919 for use as an adsorbent of gases and vapors for gas masks.[48] Xerogels are often used as desiccants due high water adsorption capacity and as stationary phase in chromatography.[49,50] As silica aerogels and xerogels are rather similar in structure and certain properties, the focus will be on the aerogels while mentioning key difference between aerogels and xerogels when the properties are discussed.

Silica aerogel are used in many applications due to their wide range of interesting properties. The material provides high surface area ($500\text{-}1200\,\text{m}^2\,\text{g}^{-1}$), high porosity (80-99 %), low thermal conductivity ($0.001\text{-}0.005\,\text{W}\,\text{m}^{-1}\,\text{K}$), low density ($0.003\,\text{g}\,\text{cm}^{-3}$), and very low dielectric constant (k=1.0-2.0), all these properties can be exploited in a wide range of applications.[51] The silica xerogel is similar in multiple ways, however due to the collapse of pores the density increase while pore sizes decrease.[52]

The aerogel structure is composed of silica nanoparticles, usually 2-5 nm in size that are called primary particles.[51] The primary particles will agglomerate with other primary particles into the secondary particles. The packing of primary particles

will contain some irregularities which creates the micropores of the aerogel and xerogel. Secondary particles bond together into longer interconnected chains to form the complete gel network. Voids between these interconnected chains of secondary particles produce the mesopores of the aerogel, and to a lesser extent the xerogel. As the xerogel is produced by collapsing the gel network these voids between secondary particle chains are significantly reduced, this is why a xerogel will be primarily microporous with very few mesopores.

The traditional method of removing the swelling agent without shrinking the pore structure is using supercritical drying (SCD). The swelling agent (H_2O) is replaced with alcohol (for high-temperature SCD) or CO_2 (for low-temperature SCD), the temperature and pressure is adjusted to change the alcohol into a supercritical phase. As there are no liquid-gas barrier in the supercritical liquid there are no capillary forces, and the structural integrity of the gel network remain while the swelling agent can be evacuated. [51] The problem with SCD cost and the challenge of scaling due to the requirements for pressure and temperature. [53]

A cheaper alternative to SCD is ambient pressure drying (APD). In APD the surface of the gel is modified to reduce surface tension, aiming to retain most of the pore network during the drying process. [53] While the APD method is not as effective as SCD, APD is significantly cheaper and rather easy to scale up. When using the APD method the gel is modified with a silylation agent, e.g. hexamethyldisilazane (HMDS), which alter the surface from hydrophilic silanol groups to hydrophobic trimethylsilane groups. The pore solvent is then exchanged from water to n-hexane due to easy removal and low surface tension, after this pore water exchange the aerogel can be obtained by slow evaporation of the n-hexane. For xerogels there is no need to change solvent as high surface tension contributes to the pore collapse as desired for xerogels.

If the drying program is gentle enough the pore network can retain most of its structure while removing the liquid (in the APD method), and a aerogel is formed. Using a quicker drying program puts further strain on the pore network when removing the liquid, this would lead to stronger collapse of the pore network and reducing in mesopores.

Two important parameters for aerogel and xerogel synthesis is the pH of the gel solution, and the previously mentioned drying method. The pH has direct impact on the condensation rate of the silica, as illustrated in Figure 2.5.

At lower pH the condensation of the silanol is acid-catalyzed, proceeding through a quick protonation of the silanol, seen in 2.1. After the first step a protonated
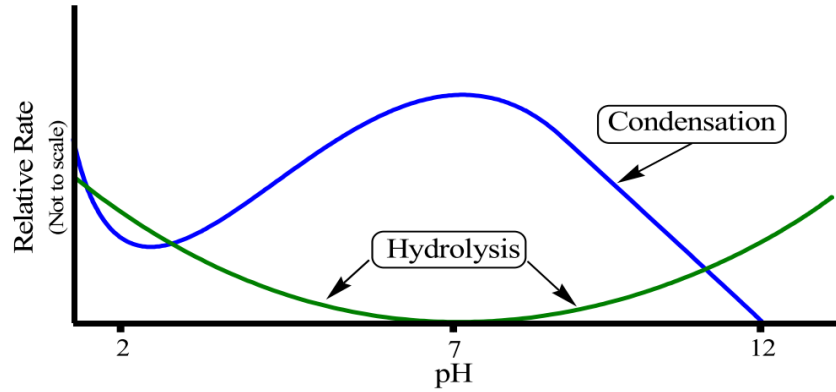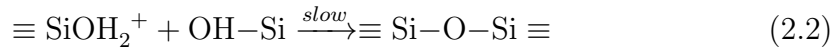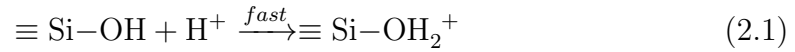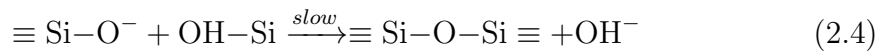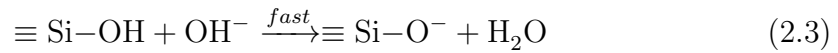
Figure 2.5: Illustration of pH on reaction rate on hydrolysis and condensation of silica.[54]

and unprotonated silanol will condensate, seen in 2.2, to form the siloxane bridge and regenerates the hydronium ion.

$$\equiv \text{Si−OH} + \text{H}^+ \xrightarrow{fast} \equiv \text{Si−OH}_2{}^+ \tag{2.1}$$

$$\equiv \text{SiOH}_2{}^+ + \text{OH−Si} \xrightarrow{slow} \equiv \text{Si−O−Si} \equiv \tag{2.2}$$

At higher pH the condensation of the silanol is base-catalyzed, proceeding through a deprotonation of the silanol, seen i 2.3. A deprotonated and silanol would then condensate, seen in 2.4, to form the siloxane bridge and regenerate the hydroxide ion.

$$\equiv \text{Si−OH} + \text{OH}^- \xrightarrow{fast} \equiv \text{Si−O}^- + \text{H}_2\text{O} \tag{2.3}$$

$$\equiv \text{Si−O}^- + \text{OH−Si} \xrightarrow{slow} \equiv \text{Si−O−Si} \equiv + \text{OH}^- \tag{2.4}$$

Both the acid-catalyzed and the base-catalysed form the siloxane bridges, however the resulting gel network turns out differently. The high pH of the base-catalyzed leads to ionization of the silica and the solubility of silica remains high, leading to growth by monomer linking of highly condensed silica species by Ostwald ripening. For the acid-catalyzed the solubility of silica is low and the growth proceed through aggregation with highly condensed and less condensed silica species by aggregation. Acid-catalyzed gels therefore construct a network of fibrous silica chain while the base-catalyzed gels construct a network of largers particles with significant branching. These two different networks are illustrated in Figure 2.6
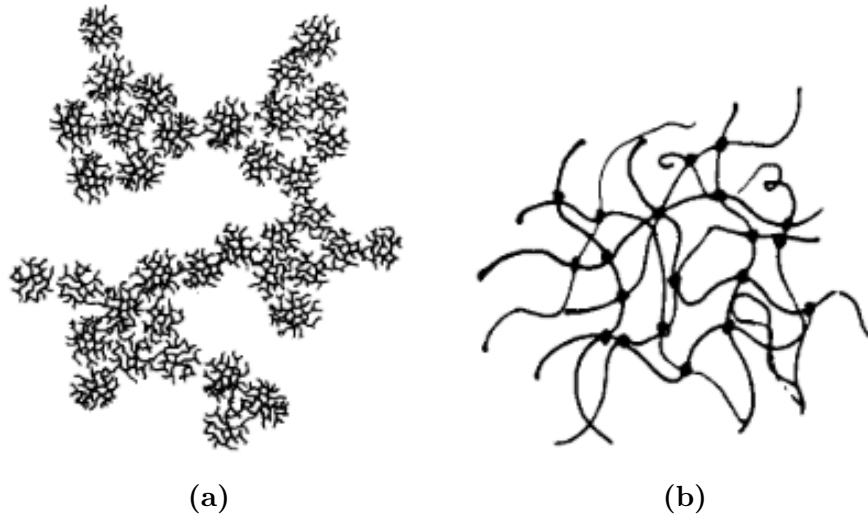
11

(a)   (b)

Figure 2.6: The structure of wel gel networks from a) base-catalyzed condensation and b) acid-catalyzed condensation. Reused from Brinker and Scherer[55] with permission.

In this thesis, the silica aerogel and xerogel is synthesized using base-catalyzed gelation.

2.3   Organosilanes

Organosilanes are a class of reagents that feature a organic tail and a silane head, usually triethoxysilane or trimethoxysilane. The ethoxy or methoxy groups on the head of the organosilane groups are highly reactive, and the interchangeable nature of the organic tail group makes organosilanes a highly flexible option for surface treatments and coatings. In this work only the (3-aminopropyl)triethoxysilane (APTES) will be used (shown in Figure 2.7a), three examples of organosilanes are shown in Figure 2.7.

Organosilanes can also rapidly polymerize if the ethoxy or methoxy groups are hydrolyzed, to optimize the reaction with the materials surface H_2O free conditions are optimal.[56]

Functionalization of porous materials using organosilanes has been performed on a variety of materials with various organosilanes. Shahbazi *et al.*[15] used
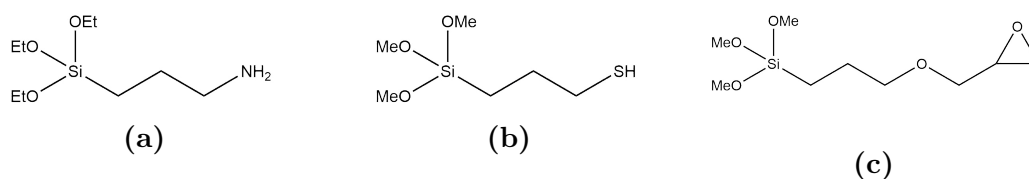
Figure 2.7: Structure of three organosilane molecules. a) (3-aminopropyl)triethoxysilane (APTES), b) (3-mercaptopropyl)trimethoxysilane, c) (3-glycidoxypropyl)dimethyl-ethoxysilane.

APTES as an intermediate step to functionalize SBA-15 with a melamine-based dendrimer. Malhis *et al.*[16] functionalized both silicalite-1 and MCM-48 with both APTES and (3-mercaptopropyl)trimethoxysilane. Ahmed and Sakthivel[57] introduced APTES *in-situ* to SAPO-5 in a hydrothermal synthesis.

2.4 X-ray diffraction

X-ray diffraction (XRD) is a versatile and powerful characterization method that utilize monochromatic x-rays. A collimated beam of X-rays is sent towards the sample and as the x-rays hit the sample the x-rays are diffracted by the long range order of the sample. The diffraction occur according to Bragg's Law[58,59] (2.5) and generate constructive interference maximas that are detector by an external sensor. This constructive interference occur when path length between layers in the sample is equal to an integer of the wavelength, illustrated in Figure 2.8.[58]

$$n\lambda = 2d \sin \theta \tag{2.5}$$

where λ is the wavelength of the x-rays, n is a positive integer, d is the path length between reflecting layers illustrated in Figure 2.8, and θ is the incident angle of the inbound x-rays.

XRD can be applied to either powered samples or single crystals. Single crystal X-ray diffraction (SCXRD) allows for identification of the 3D structure of a material or molecule. This technique require extensive preparation due to the single crystal requirement, and is extensively used when attempting to elucidate structure of novel molecules and materials. SCXRD will neither be discussed further nor used in this work.

Another method of XRD is the powder X-ray diffraction (PXRD) developed by Peter Debye and Paul Scherrer, where a powder is subjected to the monochromatic
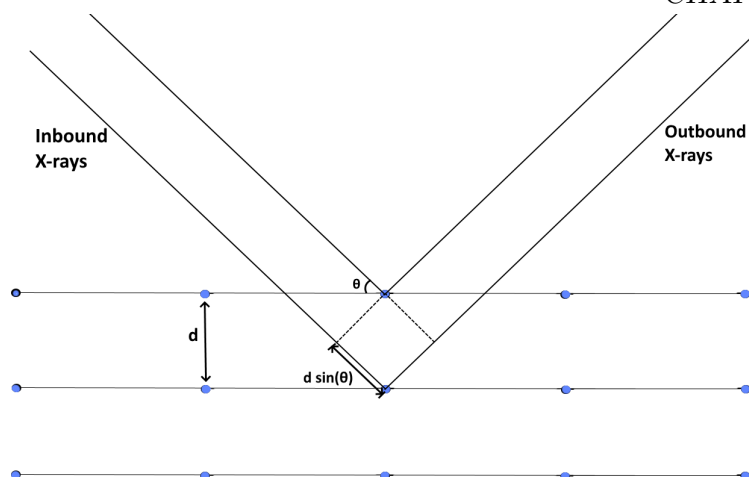
Figure 2.8: The principle for X-ray diffraction. When the path length, $d \sin \theta$, between the two planes is equal to an integer of λ, $n\lambda$, constructive interference will occur.

X-rays. PXRD assumes that at least some crystallites in the powder will be appropriately aligned with the X-ray for diffraction.[59] PXRD allows for identification of crystalline phases in the sample by comparing the recorded reflections and their intensities with diffraction pattern of previously identified structures. Multiple databases of diffraction patterns exist, where the largest and most commonly used is the Powder Diffraction Files (PDF)[60] and the Crystallographic Open Database (COD).[61] This work will make use of powder X-ray diffraction (PXRD) to identify crystalline phases and check amorphous materials for crystalline phases.

In this work the ideal diffraction patterns for the SAPO-5 and AlPO5, and the Silicalite-1 is the AFI and MFI respectively. The calculated diffractograms for the AFI and MFI framework types was collected from the Atlas of Zeolite framework types,[33] and is shown in Figure 2.9. Presence of other reflections then those in the theoretical diffractogram would mean presence of foreign crystalline phases which is unwanted. For the SBA-15, the silica Aerogel, and the silica Xerogel the presence of distinct reflections would indicate unwanted phases as these materials are amorphous, and should therefore not have any sharp, distinct reflections due to their lack of long range ordering.
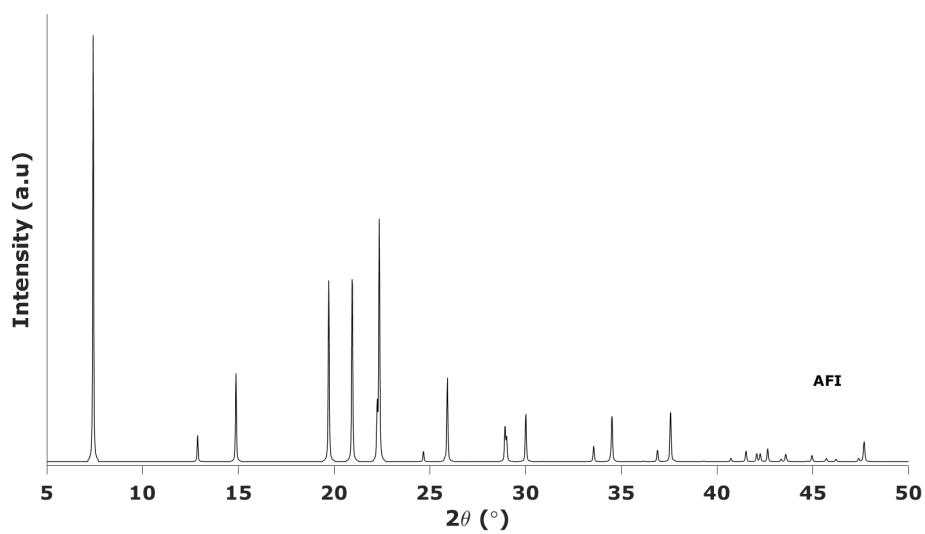
(a)
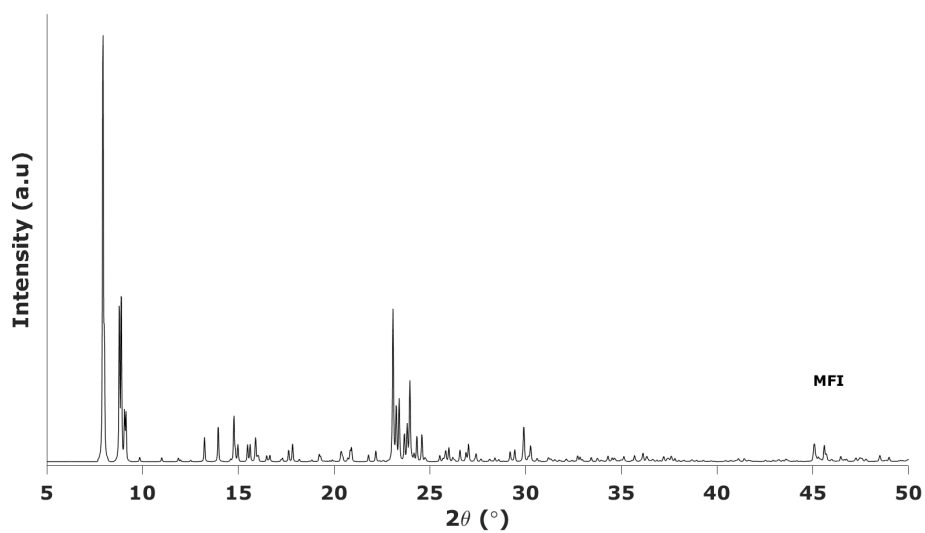
(b)

Figure 2.9: Calculated diffractograms of a) AFI and b) MFI frameworks, from the Atlas of Zeolite framework types.[33]

2.5 Nitrogen physisorption

N_2 physisorption can provide information regarding both surface area, pore volumes and pore distribution. As high surface area is often desired for catalyst supports to

15

allow for high dispersion of active material, using physisorption experiments is a widespread and highly utilized method of determining surface area, pore distribution, and pore volume. Specific surface area of a powder is usually determined using the Brunaer, Emmett, and Teller (BET) method. BET utilize a linearized physisorption curve, Equation 2.6, from the monolayer-adsorption area to determined the surface area occupied by the adsorbent.[62]

$$\frac{p}{V(p_0 - p)} = \frac{1}{V_m c} + \frac{c-1}{V_m c} \times \frac{p}{p_0} \tag{2.6}$$

where p is the equilibrium partial pressure of the gas with the surface, p_0 is the saturation pressure, V is gas volume absorbed at STP, V_m is volume of monolayer-coverage at STP, and c is a constant related to the heat of adsorption.[62] Due to monolayer-adsorption requirement the BET equation is usually limited to 0.05-0.35 p/p_0.[28]

Most inert gases (i.e. N_2, Ar, or Kr) can be used for physisorption measurements, however N_2 is the most common due to high availability and low cost. Physisorption measurements are therefore usually performed at 77 K, the condensation temperature for N_2 at 1 atm.[28]

The materials pore size and composition results in varying surface measurement isotherms. These isotherms have been classified by IUPAC, and provide a rapid method to gauge a materials pore structure. The six IUPAC defined isotherms is shown in Figure 2.10a.

Two isotherms, Type I and Type IV, are of particular relevance for this work. Type I isotherms are found in microporous materials with small external surfaces, where limit to N_2 uptake is controlled by the accessible micropore volume rather then the internal surface area. Type I isotherms are expected for zeotypes like SAPO-5,AlPO-5, and Silicalite-1. Type IV isotherms are found in mesoporous materials. The hysteresis loop is caused by capillary condensation, with limited uptake at high p/p_0. Point B in Figure 2.10(a) indicate transition from monolayer adsorption to multilayer adsorption. The type IV isotherm is expected for the mesoporous materials,[63] like the SBA-15 and the aerogels.

The shape of the hysteresis loop from physisorption measurements are attributed to adsorption metastability or network effects,[64] while the hysteresis existence is attributed to capillary condensation in mesopores.[63] H1 hysteresis loops are attributed to materials with narrow, uniform pores with minimal network effects, and is therefore expected for SBA-15.
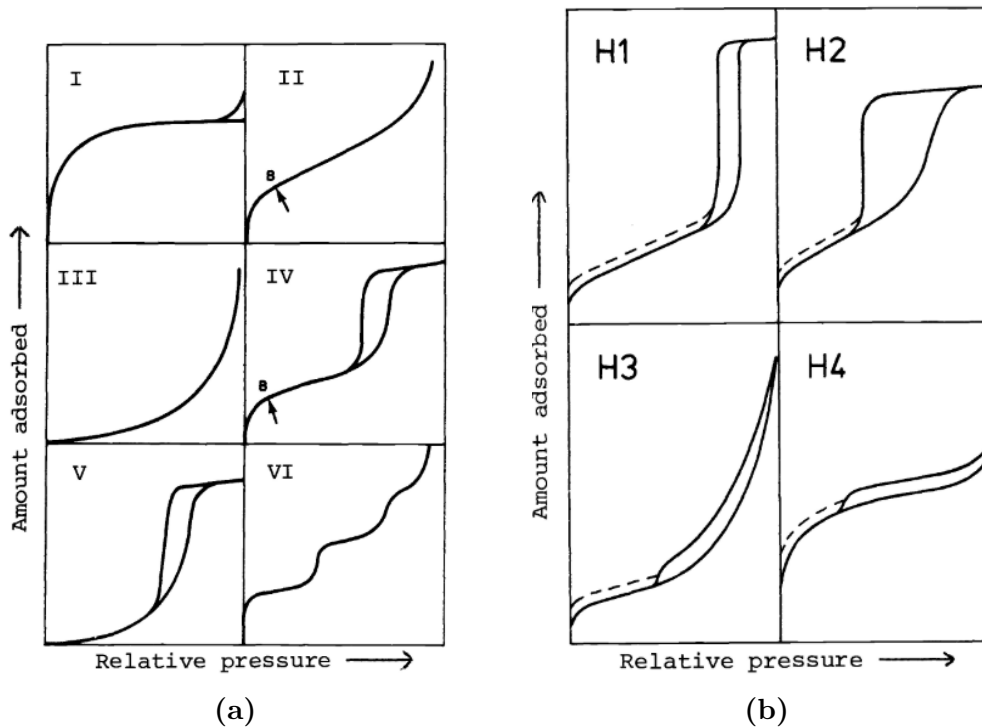
Figure 2.10: a) The six adsorption isotherms for surface measurement from BET, as classified by IUPAC.[63] b) The four adsorption hysteresis for multilayer physisorption, as classified by IUPAC.[63]

2.6 X-ray absorption spectroscopy

X-ray adsorption spectroscopy (XAS) is a spectroscopic technique that study matter while X-rays are adsorbed. Adsorption spectra are obtained by varying X-ray energy close to the energy required to excite and ionize the various atoms, the characteristic adsorption energies correspond to the binding energy of the elements inner-shell electrons. As the adsorption energies are characteristic for each element the X-ray beam can target specific elements in the sample by scanning across the adsorption edge of the desired element, deviation from an elements adsorption energies provide information regarding oxidation state and the local environment.[65] As an adsorption phenomenon the adsorption of X-rays is described by Lambert's law:

$$I_{\mathrm{t}} = I_0 e^{-\mu(E)x} \tag{2.7}$$

where I_{t} is transmitted intensity and I_0 is intensity of incident X-rays, $\mu(E)$ is the X-ray adsorption coefficient as a function of energy which relates to the probability of adsorption, and x is the thickness of the sample.[66,67] The adsorption coefficient

depends on the sample density, ρ, the atomic number, Z, the atomic mass, A, and the X-ray energy, E:[66]

$$\mu \approx \frac{\rho Z^4}{AE^3} \tag{2.8}$$

Adsorption edges, as illustrated in Figure 2.11 for rhenium,[68] are described by a marked increase in the $\mu(E)$, the position of this feature is often called the E_0 which describes the adsorption energy threshold of the sample. The adsorption edge correspond to the ionization of core electrons in the element due to the X-ray having the same energy as the core electrons binding energy. When the X-ray energy and core electron binding energy is equal a photoelectron is emitted due to the photoelectric effect.[66]

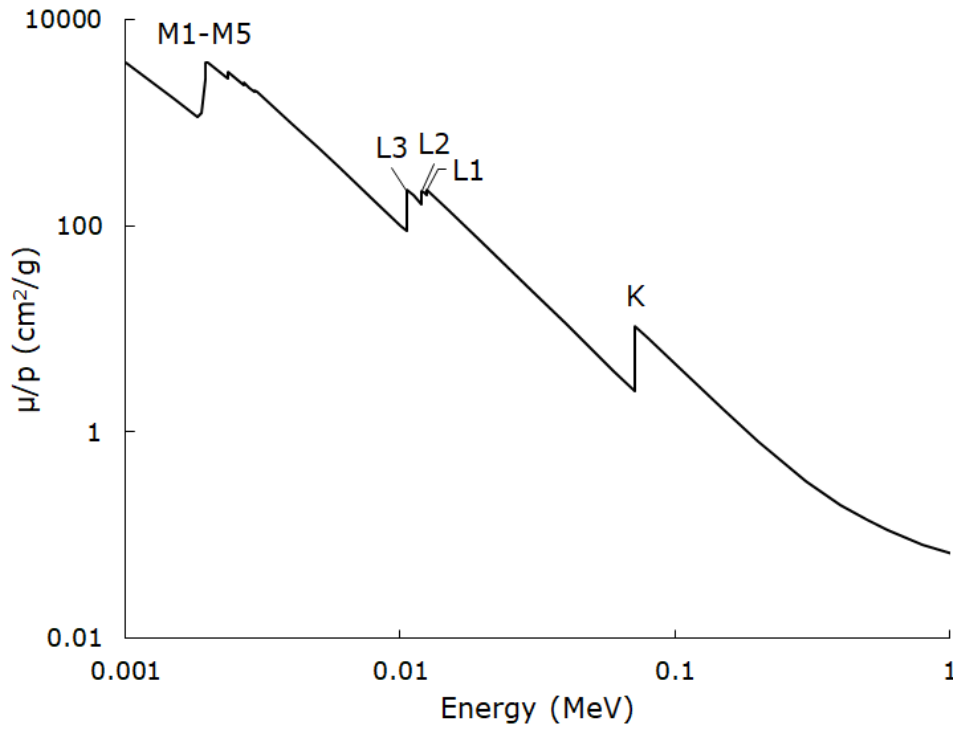
Figure 2.11: The mass attenuation coefficient (μ/p) as a function of energy for rhenium (Z=75), with indicators on the edges.[68]

The dependence of $\mu(E)$ on both Z^4 and E^3, show in 2.8, allows for good contrast of elements of differing mass by adjustment of the X-ray energy.[66] Since the core electron binding energies are well-defined the X-rays energy can be selected to

18

correspond to specific elements, making XAS a element specific technique. The choice of adsorption edge utilized depend on the mass of the element; the K edge is the most common measurement edge while the L edges are used for heavier atoms with hard X-rays[66] For this project the target element is rhenium, where the XAS is usually recorded around the L_{III}-edge at $10\,535\,\text{eV}$.[68,69]

Analysis of XAS is split between two primary areas. The X-ray adsorption near edge structure (XANES) contain the features of the immediate area by the adsorption edge. XANES can offer qualitative information like oxidation state and the local chemical environment. While XANES focuses on the features of the edge and immediate surrounding area the Extended X-ray Adsorption Fine Structure (EXAFS) investigate the fine structure after the edge. EXAFS provides detailed information about the local chemical environment. These two areas are illustrated in Figure 2.12.
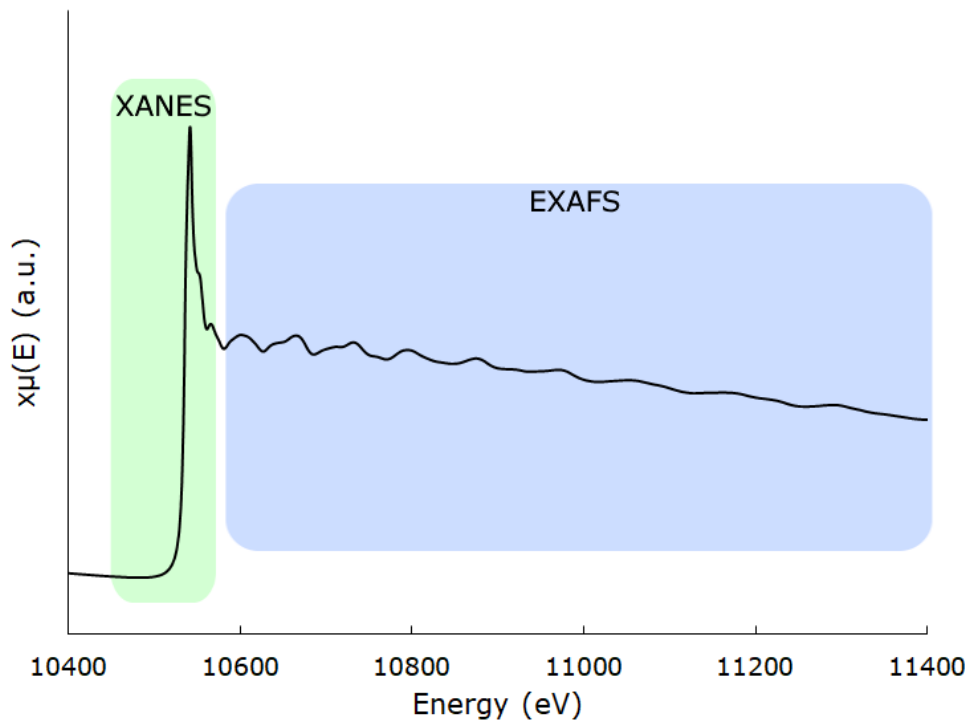

Figure 2.12: Division of a XAS spectrum of rhenium foil (Re(0)) into the two primary areas, the XANES and the EXAFS.

2.6.1   X-ray Adsorption Near Edge Structure (XANES)

The X-ray adsorption near edge structure (XANES) contain the immediate area before and a bit after the adsorption edge. For most elements this area would be 5-10 eV before the edge and 30-50 eV after the edge.[65] XANES is usually utilized for a qualitative description of samples by comparisons to well known reference samples. The XANES region cover the energy range sufficient for excitation of electrons to unoccupied electronic states close to the Fermi level. As this excitation would be highly influenced by the electronic state of the adsorbing atom any difference in electronic state would have an impact on the XANES spectrum. The primary origin of changes to the electronic state would be oxidation state or chemical environment (i.e. coordination to neighbouring atoms or identify of ligands). The excitation can also contain a pre-edge for K-edge spectra, indicating octahedral or tetrahedral coordination due to the Laporte rule, however for the L_{III} edge used for rhenium there are no pre-edges. This makes XANES a versatile "fingerprint region" that can quickly identity known phases of compounds.[66]

As mentioned the electronic state has significant impact on the XANES spectrum, this can be explained as a shift in the effective nuclear charge of the adsorbing atom. A high oxidation state samples will have lower shielding effects on the electrons, increasing attraction to the nucleus and increasing the energy required to excite the electron. Thus oxidation states are usually identifiable by E_0 shift, however for rhenium and other third d-block elements this shift is small and often not linear which makes E_0 derived oxidation state uncommon for these samples.[70] For rhenium the intensity of the white line, the sharp feature at the top of the edge, can be a indicator of oxidation state, making white line analysis a more suited method to indicate oxidation state for rhenium samples.[71,72]

2.6.2   Extended X-ray Adsorption Fine Structure (EXAFS)

Initially recognized in the 1920s, the EXAFS phenomenon was not employed until the tunable X-rays from synchrotrons became available in the 1970s.[73,74] The EXAFS region start at the end of the XANES region can stretch as far as 1000 eV from the edge. The energy being higher then the edge leads to ionization of the sample by photoelectron emission. When the excited electron leaves in the form of the photoelectrons it can be considered a wave, this wave would scatter off neighbouring atoms and generate a backscattered wave. As the primary photoelectron wave and the backscattered wave interact a fine structure appear in the XAS, seen as a oscillation, due to the interference. Assuming single-scatter, where the electron wave moves directly between adsorber and backscattering

neighbour, and plane-wave calculations can be preformed to model the EXAFS.[66] Therefore the EXAFS area will contain information regarding interatomic distance, coordination number for the adsorbing atom, type of backscattering neighbour, and the disorder of the bonding lengths.[66] An illustration of the interaction between emitted photoelectron wave and backscattered wave can be seen in Figure 2.13.
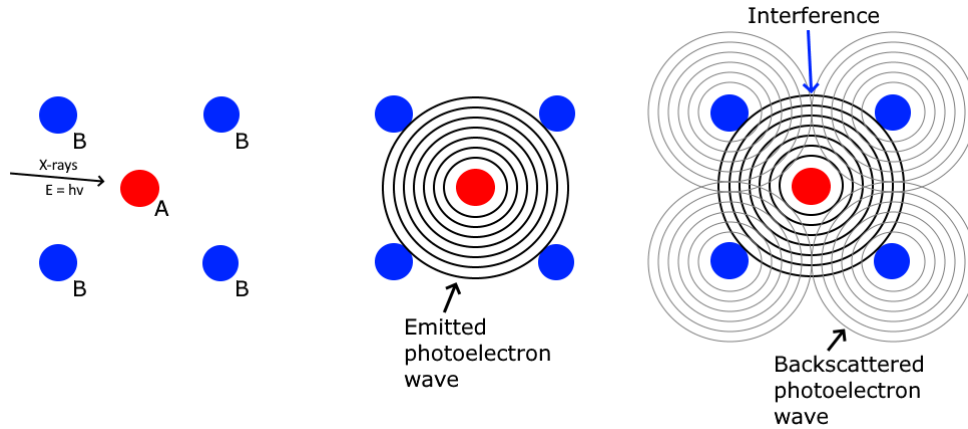

Figure 2.13: Simple illustration of the behaviour of emitted photoelectron waves after X-ray adsorption. The emitted photoelectron is backscattered and cause interference.

As the EXAFS is modeled as a wave, the X-ray energy is commonly converted to the wave number of the photo-electron, k. The convertion is done using the following equation:

$$k = \sqrt{\frac{2m(E - E_0)}{\hbar^2}} \tag{2.9}$$

where k is the wave number of the emitted photo-electron, $\hbar$ is the reduced Planck constant, m is the electron mass, and E_0 is the adsorption edge energy.[66,72]

Extraction of the information contained in the fine structure in EXAFS is done by comparing a theoretical oscillating curve, $\chi^{theory}(k)$, with the experimentally gathered curve, $\chi^{exp}(k)$. Since numerical solutions to complex oscillating curves can overvalue certain parameters some assumptions regarding the local environment of the sample should be applied. The $\chi^{theory}(k)$-curve is calculated using the EXAFS equation, 2.10, selecting the best fit based on the least-square approach to minimize difference in theoretical and experimental curves.

$$\chi(k) = S_0^2 \sum_j \frac{N_j A_j}{r_j^2} e^{(-2r_j/\lambda)} e^{(-2\sigma_j^2 k^2)} \sin\left(2kri + 2\phi i(k)\right) \tag{2.10}$$

21

where S_0^2 is the passive electron reduction factor, j is the "j^{th}" neighbouring shell, N is the coordination number, A is the amplitude function of the scattering atom, r is the interatomic distance, λ is the photoelectron mean-free path, σ_j is the disorder for the jth-shell also known as the Debye-Waller factor.[75]

2.7 Diffuse Reflectance Infrared Fourier Transform Spectroscopy

Diffuse Reflectance Infrared Fourier Transform Spectroscopy (DRIFTS) is an method of infrared (IR) spectroscopy which allow observation of adsorbed IR via induced vibrations of chemical bonds in molecules. IR spectra frequently present the wavenumber, reciprical centimeters (cm^{-1}), as the x-axis. As bands in the IR spectra correspond to distinct functional groups, these spectra can be used to determine functional groups in the sample. In this work DRIFTS will be used to detect the presence of brønsted acid sites in the SAPO-5.

2.8 Thermogravimetric analysis

Thermogravimetric analysis (TGA) is a versatile method which measure the weight of the sample as a function of time and temperature. The weight loss from the sample can correspond to desorption of adsorbed gases, evaporation of liquids in the sample, or decomposition of the material. TGA is commonly used to determine thermal stability in samples, but has multiple applications e.g. quantification of residual solvents.

TGA is often coupled to qualitative analysis methods, combining the quantitative weight measurements of TGA with qualitative methods allows for identification of species leaving the sample at certain temperatures or over time. In this work, TGA coupled with MS (TGA/MS) will be utilized to quantitatively determine amount of attached aminopropyl groups on the surface of the materials.

Assuming only aminopropyl combust the total mass loss would be described by the mass Δ_m:

$$\Delta_m = wt\%_{start} - wt\%_{end} \tag{2.11}$$

where the wt%$_{start}$ is the mass wt% where combustion begin, and wt%$_{end}$ is the wt% after combustion of AP groups. This Δ_m can then be used to estimate AP amount:

$$n = \frac{\Delta_m \times m_{sample}}{\text{Mm}_{AP}} \qquad (2.12)$$

where n is the mols of AP in the sample, m$_{sample}$ is the total mass of the TGA sample, and Mm$_{AP}$ is the molar mass of the aminopropyl group. Performing this estimation will also allow stochimetric evaluation of the rhenium introduced samples by comparing amount rhenium in the sample to amount AP on the surface.

A common method coupled in TGA measurements is the differential scanning calorimetry (DSC), which measure the heat required to increase the temperature of the sample.[59] This method allows detection of endothermic or exothermic reactions and phase transitions. In this work DSC is coupled to the TGA measurements but are not used for anything other then quick indication for the heat of reaction, which for a combustion reaction is exothermic.

2.9 Scanning electron microscopy

Scanning electron microscopy (SEM) is a imaging technique capable of resolution down to 5 nm. The SEM utilize an electron beam to scan across the sample, resulting secondary electrons and back-scattered electrons are detected and used to generate the image.[28,76]

SEM requires that the sample is conductive to prevent charging effects in the material, which would interfere with the imaging. For non-conductive samples the surface is often coated with a conductive material, e.g. gold or graphite. As all materials in this work is non-conductive SEM use required a surface coating of the samples.

3. Experimental

3.1 Synthesis of support materials

3.1.1 SAPO-5 and AlPO-5

SAPO-5 and AlPO-5 was produced using a one-pot hydrothermal synthesis based on previous work by Tafjord[14], without addition of Si-precursor to the AlPO-5. The specific synthesis of one SAPO-5 sample (S5-7) is reported here, while molar ratios for all SAPO-5 and AlPO-5 samples are listed in Table 3.1, and the synthesis route is illustrated in Figure 3.1. Pseudoboehmite (Al_2O_3, Sasol Catapal B, 2.0069 g) was slowly added to a phosphoric acid (H_3PO_4, 85% 3.26 g) and water (H_2O, 25.44 g) mixture, the solution was then stirred for 3 h. For the SAPO-5 Ludox® AS-40 (SiO_2, 40wt% Sigma-Aldrich, 0.90 g) was added dropwise and solution was further stirred for 20 min. Triethylamine (TEA,1.74 g) was added dropwise and the solution was stirred for 30 min before it was transferred to a teflon-lined autoclave (100 ml) and crystallized at 200 °C for 24 h/72 h.

The product was washed and centrifuged, then dried at 70 °C over night. XRD was used to determine the phase of dried samples. Phase-pure samples were calcined at 550 °C for 16 h and 1 °C min^{-1} heating.
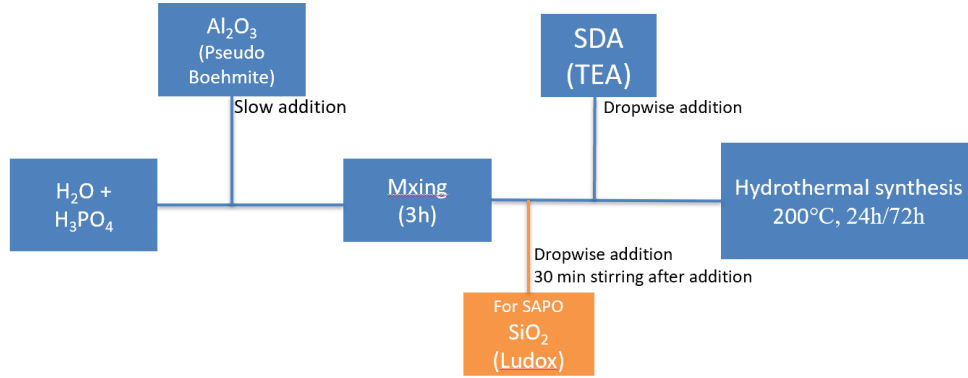
Figure 3.1: Illustration of the synthesis route for the synthesis of both AlPO-5 and SAPO-5. The orange insert indicate addition only for SAPO-5.

Table 3.1: All synthesized SAPO-5 (S5-n) and AlPO-5 (A5-n) samples. Molar ratios of precursors are calculated based on aluminium amount. Crystallization time is also given for each sample, all samples were crystallized at 200 °C.

Sample ID	Al	P	Si	TEA	H$_2$O	Crystallization Time [h]
S5-1	1.0	1.2	0.2	0.6	27.2	24
S5-2	1.0	0.8	0.2	1.0	50.0	24
S5-3	1.0	0.8	0.2	1.0	50.0	24
S5-4	1.0	1.0	0.2	0.8	49.8	72
S5-5	1.0	1.0	0.2	0.6	50.0	72
S5-6	1.0	1.0	0.2	0.4	50.1	72
S5-7	1.0	1.0	0.2	0.6	50.1	24
S5-8	1.0	1.0	0.2	0.6	30.0	72
S5-9	1.0	1.0	0.2	0.6	30.0	24
S5-10	1.0	1.0	0.2	0.6	29.6	24
S5-11	1.0	1.0	0.2	0.6	50.0	24
S5-12	1.0	1.0	0.2	0.6	50.1	24
S5-13	1.0	1.0	0.2	0.6	50.0	24
S5-14	1.0	1.0	0.2	0.6	50.0	24
A5-1	1.0	0.8	-	1.0	50.0	24
A5-2	1.0	0.8	-	1.0	50.0	24
A5-3	1.0	1.0	-	0.8	50.0	72
A5-4	1.0	1.0	-	0.6	50.0	24
A5-5	1.0	1.0	-	0.6	50.2	24
A5-6	1.0	1.0	-	0.6	50.1	24
A5-7	1.0	1.0	-	0.6	49.8	24

3.1.2 Silicalite-1

The synthesis of Silicalite-1 was based on Guth *et al.*[77]. In short; H_2O, ammoniumfluroide (NH_4F, Sigma-Aldrich), and Tetrapropylammonium bromide (TPAB, 98%, Sigma-Aldrich) was mixed for 1 h. The Si-source, either TEOS or colloidal silica, was added dropwise to the solution. The mixture was then stirred for 45 min. The mixtures was then transferred to a teflon lined autoclaves, and subjected to hydrothermal synthesis at 200 °C for 2 d or 15 d, depending on amount of NH_4F. The synthesis route is also illustrated in Figure 3.2
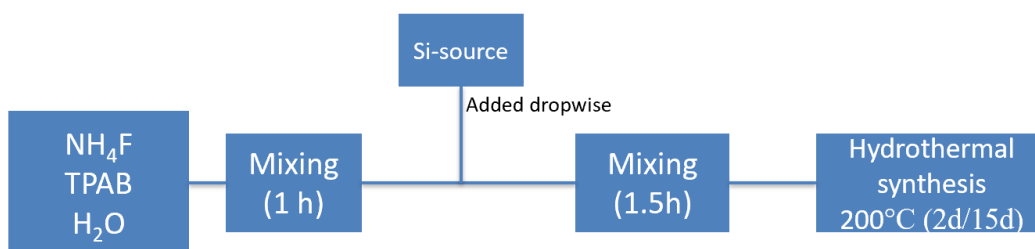

Figure 3.2: Illustration of the synthesis route for the synthesis of Silicalite-1. Si-source was either colloidal silica (Ludox AS-40) or TEOS.

Samples were subsequently washed with H_2O and centrifuged. Phase-pure samples were calcined in air for 16 h at 550 °C, the heating was from 25 °C to 550 °C with $1\,°C\,min^{-1}$ temperature ramp rate. Molar ratios reactants and crystallization time for all samples is given in Table 3.2.

Table 3.2: Molar ratio of reactants with regard to SiO_2 added to synthesize Silicalite-1. Hydrothermal synthesis time is given as time.

Sample ID	Si-source	TPAB	NH_4F	H_2O	Time [h]
S1-1	TEOS	0.08	1.00	20.12	48
S1-2	TEOS	0.08	0.04	19.92	360
S1-3	Ludox AS-40	0.08	1.00	20.00	48
S1-4	Ludox AS-40	0.08	0.04	19.87	360

3.1.3 SBA-15

Two methods were used to synthesize SBA-15, the methods diverged in stirring process. Pluronic® P123 (0.5 g) was dissolved in HCl (60 ml, 1.5 M) while CTAB

(0.6 g, 1.37 mmol) was dissolved in H_2O (25 ml). After both mixtures was completely dissolved the solutions were mixed and heated to 40 °C. Ethanol (20 ml, 0.34 mol) was then added slowly and tetraethylorthosilicate (TEOS, 10 ml, 45.12 mmol) was added dropwise to the mixture. The preferred method was decided based on surface area achieved, and multiple samples was then made using the preferred method.

For method 1, the solution was mixed at 35 °C for 45 min, then transferred to a teflon autoclave liner. The autoclave was heated to 80 °C for 18.5 h, then the temperature was elevated to 140 °C for 4 h. The product was rinsed with H_2O.

For method 2, the solution was heated to 40 °C and mixed for 24 h. The solution was transferred to a teflon autoclave liner and heated to 140 °C for 24 h. The product was rinsed with H_2O and subsequently calcined in air at 550 °C for 10 h, with 1 °C min^{-1} heating.
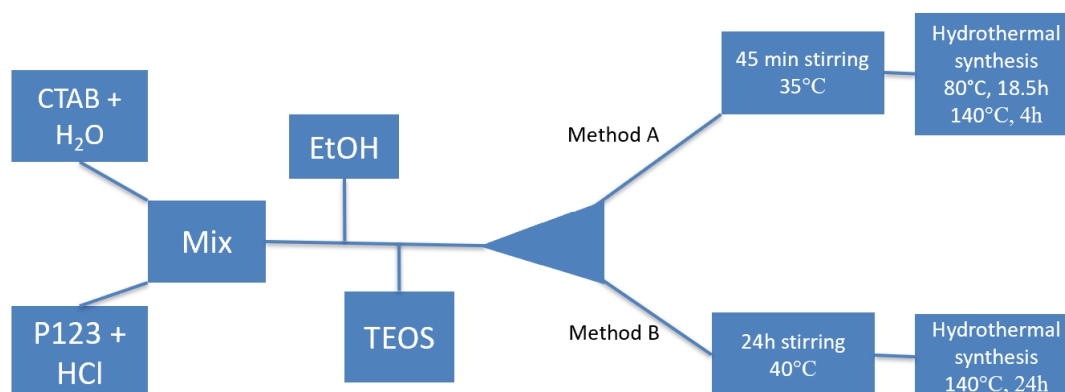

Figure 3.3: Illustration of the synthesis route for the synthesis of SBA-15. The diverging method A and method B indicate split of route for the two attempted synthesis routes. Method A was used for samples later post-synthetically modified.

Table 3.3: BET surface area, average pore size, and pore volumes for all synthesized SBA-15 samples after calcination.

Sample ID	Synthesis method	Mixing time [h]	Autoclave temperature [°C]
S15-1c	1	0.75	80/140
S15-2c	1	0.75	80/140
S15-3c	2	24	140
S15-4c	2	24	140
S15-5c	1	0.75	80/140
S15-6c	1	0.75	80/140
S15-7c	1	0.75	80/140
S15-8c	1	0.75	80/140
S15-9c	1	0.75	80/140
S15-10c	1	0.75	80/140

3.1.4   Silica Aerogel and Xerogel

The synthesis of Silica Aerogel (SAG) was based on Bhagat *et al.*[78] using sodium silicate ("water glass", 155.78 g, 27.2wt.%) ion-exchanged with Amberlite IR-120 into silicic acid (SA). The SA was diluted with H_2O to 8wt.% SA. Hexamethyldisiloxane (HMDSO, 21.78 g) and hexamethyldisilazane (HMDS, 20.72 g) was simultaneously added and the mixture was vigorously stirred until significant gelation occurred, subsequently the mixture was left to age for 1 h. The hydrogel was then submerged in n-heptane for 24 h exchange the solvent, then dried with Program 1 shown in Figure 3.5. The described synthesis route is also illustrated in Figure 3.4

Silica Xerogel (SXG) synthesis method was similar to the SAG synthesis. The "water glass" (308.14 g, 27.3wt.%) was ion-exchanged with Amberlite IR-120 and diluted to 8 wt.% SA. NH_3 (5 M) or NaOH (2 M) was added until gelation occurred. Samples where then dried with Program 2 shown in Figure 3.5.
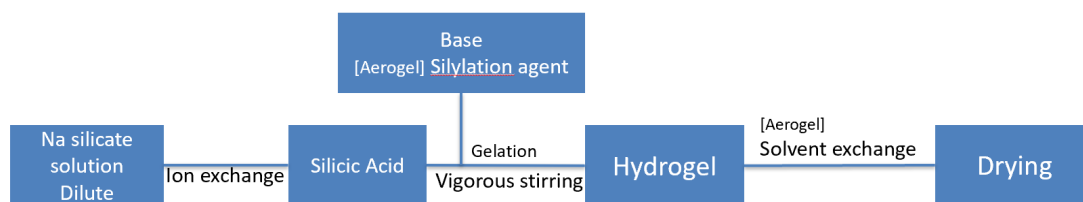
Figure 3.4: Illustration of the synthesis route for both the silica Aerogel and the silica Xerogel using water glass (sodium silicate). Addition of silylation agent and solvent exchange is only performed for the aerogel, for the xerogel these actions were skipped to ensure a collapse of the pore network.
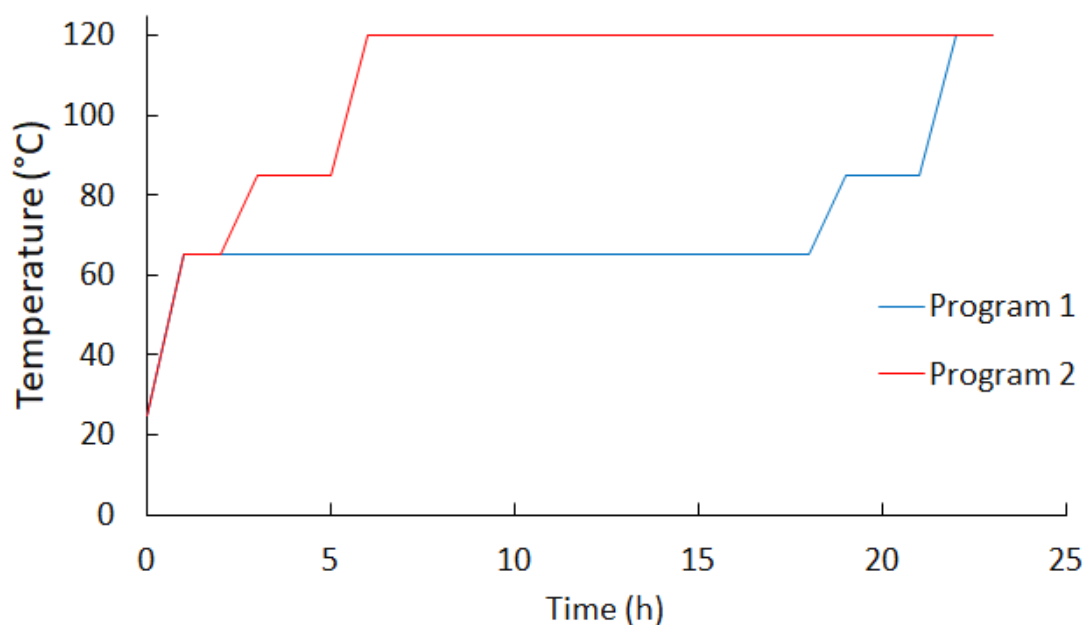

Figure 3.5: Temperature programs used for drying of wet gels. Program 1 used for SAG-01 and SXG-01, while Program 2 used for SXG-02, SXG-03, and SXG-04. All heating rates were $5\,^{\circ}\mathrm{C}\,\mathrm{min}^{-1}$.

3.2 Surface modification

Samples used for post-synthetic modification were selected based on having the correct phase and largest surface area, with consideration for pore size distribution on mesoporous materials.

Surface modification of the materials was done using (3-aminopropyl)triethoxysilane (APTES) in accordance with Shahbazi *et al.*[15] which modified SBA-15 with APTES as an intermediate step. Approximately 0.6 g of material was degassed at 150 °C under reduced pressure (0.0018 mbar) for 12 h, then suspended in dry toluene (25 ml). APTES (0.7 ml, 2.99 mmol) was slowly added to the suspension and the mixture was heated to 120 °C for 24 h under N_2 atmosphere. Synthesized material was collected by filtration and washed with dry toluene, then dried under reduced atmosphere.

Larger surface modification was carried out on the S15-9c and SAG-01 systems, where approxmately 2.0 g of sample was put through the same process as previously described, using 75 ml toluene and 2.3 ml APTES.

3.3 Rhenium introduction

The amine-functionalized support was weighed out, and a Rhenium(VII) Oxide (Re_2O_7) amount corresponding to 10-12wt% Re was transferred to roundbottom flask. The Re_2O_7 was dissolved in acetonitrile (ACN, 25 ml), and the previously weighed sample was added to the solution. The solution was subjected to a nitrogen atmosphere, and heated to 90 ° °C for 24 h. All materials except the Xerogel and Aerogel was collected by filtration and rinsed with ACN. The Xerogel and Aerogel was washed in a centrifuge using EtOH to re-suspend the gels three times. Materials were then completely dried under reduced pressure.

3.4 Characterization of porous materials

3.4.1 XRD

PXRD was performed on a Bruker D8 A25 DaVinci X-ray Diffractometer with CuKα (λ=1.5406 Å) radiation, with a LynxEye™ SuperSpeed Detector in Bragg-Brentano geometry mode. Samples were characterized with one of two programs, the first program was 5-75° with a 6 mm variable divergent slit, 30 min counting time, and a 0.013° step size. This program was used for the majority of sample, including all crystalline samples, surface modified, and rhenium introduced samples. The second program was 5-75° with a 6 mm variable divergent slit, 15 min counting time, and a 0.045° step size. This second program was used for as synthesized

aerogel, as synthesized SBA-15, and calcined SBA-15, with the exception of the SBA15-3 (S15-3as and S15-3c) which used the first program.

3.4.2 Surface area and pore distribution

Surface area determination and pore size distribution was determined on a Micromeritics TriStar 3000 Surface Area and Porosity Analyzer, using N_2 as the probe molecule with a non-ideality factor of 0.0000620. Calcined samples without post-synthetic modification were degassed *in vacuo* at 200 °C overnight before measurements, while APTES modified and Re_2O_7 introduced samples were degassed *in vacuo* at 150 °C for 24 h before measurements.

The measurements included 51 points for adsorption and 35 points for desorption, with higher density of measurement points at high p/p_0. Mesopore characterization was done with BJH derived surface area and pore volume based on cumulative surface area or pore volume between 17 Å and 3000 Å. The micropore characterization was based on t-plot using Harkins and Jura equation and a thickness range from 3.5 Å to 5.0 Å, with the exception of all silicalite-1 samples which used a thickness range from 4.3 Å to 7.0 Å.

3.4.3 FTIR

DRIFTS of functionalized materials was performed on a Bruker VERTEX 80 with a 4 mm liquid nitrogen cooled mercury cadmium telluride (HgCdTe, LN-MCT). The detector used a 2 cm^{-1} resolution and a 4000-700 cm^{-1} spectral range at 40 kHz. The samples were diluted with KBr to 5wt% and sieved to ensure particles between 212-425 µm.

The flow rate of He in the DRIFTS chamber was $13.56 \text{ mL min}^{-1}$ during spectra recording. The heating program contained several steps. First a heating to 150 °C with a ramp rate of 5 °C min^{-1} then held at 150 °C for 2 h to dehydrate the sample, after this dehydration the heat was increased to 450 °C at 5 °C min^{-1} heating then held at 450 °C for 2 h. After this high temperature hold the sample was cooled down over night at a 5 ml min^{-1} He flow rate. The heating program is illustrated in Figure 3.6.
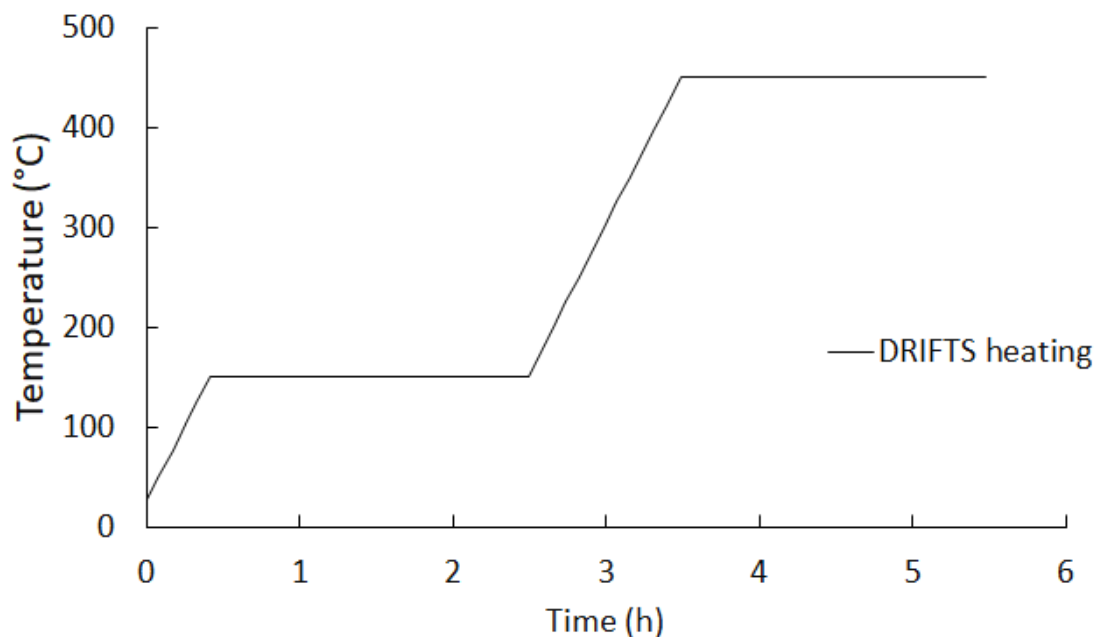
Figure 3.6: Heating program used during DRIFTS of calcined SAPO-5 and APTES modified SAPO-5.

3.4.4 TGA/MS

TGA of samples was performed on a Netzsch STA 449C Jupiter, with a Netzsch Aërlos QMS 403C MS attached for MS analysis of evolved gases. A porcelain crucible (10-30 mg) was filled with sample and heated from $35\,°C$ to $800\,°C$ with a heating rate of $5\,°C\,min^{-1}$. The sample was then held at $800\,°C$ for $1\,h$. Gas flow was set at $40\,mL\,min^{-1}$ synthetic air and $20\,mL\,min^{-1}$ Ar protective flow. The MS was set to register specific masses characteristic of oxidation of hydrocarbons, with a dwell time of $0.2\,s$. The temperature for %wt associated with the AP group was determined based on the TGA/MS signal. The AP loss range was set as 175-450 °C and 175-400 °C for the SBA15-AP and the Aerogel-AP respectively.

3.4.5 SEM

SEM was performed on a Hitachi S-3400N. Samples were placed on a sample holder and held in place with carbon tape, excess sample was removed to blowing air onto the sample. The samples were coated with gold using vacuum sputtering before placement in the S-3400N.

3.4.6 XAS

Data acquisition

X-ray Absorption Spectroscopy data was collected at the Balder beamline at the MAX IV synchrotron. The filling mode of the synchrotron was in multibunch with a current of 249 mA. The data was collected at the Re L_{III}-edge (10 535 eV). The beamline was positioned at wiggler with a double crystal monochromator, Si(111) for EXAFS data collection. The XAS data were recorded in transmission mode and the incident and transmitted beam intensities (I_0 and I_1) were detected in ion chambers filled with I_0 (30 cm) with 400 mbar N2 + 1.1 bar He, I_1 (30 cm) with 2.5 bar N2 for the rhenium L_{III}-edge.

Samples were placed in aluminium sample holders and reference compounds (Re-foil, NH_4ReO_4, $KReO_4$, $Re(VI)O_3$, $Re(IV)O_2$) were diluted in boron nitride for optimum absorption. Two scans were recorded, one only containing the XANES and one containing both XANES and EXAFS regions (referred to as "EXAFS". The XANES only scan at the Re L_{III}-edge was measured as a fly scan with 1400 points from 10 495 eV to 10 635 eV with 0.01 seconds per point. The EXAFS scan at the Re L_{III}-edge was measured as a fly scan with 4095 points from 10 285 eV to 11 735 eV with 0.01 seconds per point.
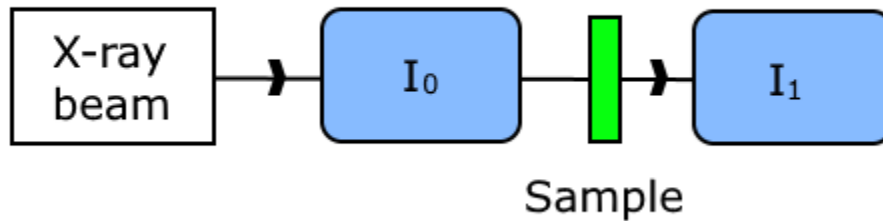

Figure 3.7: An illustration of the positioning of sample, detectors, and references while collecting XAS data. The X-ray beam is monochromatic X-rays generated by a synchrotron, the I_n is various detectors.

For both XANES and EXAFS data multiple scans were performed and summed to minimize impact of noise. All samples were energy corrected using rhenium foil (10 535 eV) as a calibration standard. Rebinning was also performed to increase signal to noise ratio. The scan summation, energy correction, and rebinning was

33

performed in the Athena software.[79]

3.4.7   XAS data analysis

Recorded XAS spectra were opened in the Athena software,[79] which is designed as a plotting and analysis program for XAS. Athena transformed the recorded spectra into k-space, $\chi(k)$, by using 2.7. The $\chi(k)$ was also further Fourier transformed into R-space, $\chi(R)$, which shows the radial distribution of backscattering shells. A k^3-weighting was utilized for all samples during Athena processing.

Unusual datapoints with sudden and intense energy shifts, referred to as glitches, was removed by point deglitching. The data was truncated until the $\chi(k)$ curve showed a consistent oscillating signal. After deglitching and truncation samples with multiple scans were merged, with the exception of spectra which deviated significantly from the other spectra. The calibration on the Re foil was performed by setting the highest point of the derivative $\mu(E)$ to $10\,535\,\text{eV}$. The E_0 for all other samples were adjusted to the 0.5 value of the normalized $\mu(E)$, using a normalization range between 30 and 150.

E_0 values of references and samples were exported, and linear regression on the references was applied to calculate oxidation state for all samples. Peak fitting was applied to the whiteline of all samples and references, using a atan step function and gaussian peak function to achieve the best possible fit. Peak heights and areas were used to estimate oxidation state for all samples, based on linear regression of the peak height/area and known oxidation state of the references. Linear combination fitting was applied to all samples, using the references as standards in the fit range of -20 to 30. At most 4 standards per sample was applied, all weights was forced to sum to 1.

EXAFS scans were normalized for the range 150 to end of spectrum. The $\chi(k)$ curve was exported to the DL_EXCURVE, hereby referred to as "excurve" software, developed by Tomic *et al.*[80] at Davesbury laboratories. Excurve produce a theoretical χ-curve which is compared to the experimentally derived χ-curve. The excurve software was set to k^2 or k^3-weighting and the k-space was varied based on the quality of the experimentally derived χ-curve. References was refined with a constant multiplicity, N, while varying Debye-Waller factor, σ^2, the distance to neighbor, R, and Fermi energy, E_F. For each reference the amplitude reduction

factor, AFAC, was also refined. For samples the AFAC of the most similar reference was applied and N, σ^2, R, and E$_F$ was refined.

4. Results

4.1 Materials

Sample naming

Sample naming is standardized for all samples to include the material type, the batch number for each sample, and the thermal treatment. The generalized sample name is as follows;

$$[\text{Material ID}] - [\text{Batch number}]X$$

where the [Material ID] is a material specific abbreviation, [Batch number] is the sequential numbering of each material produced, and X indicate as synthetized (as) or calcined (c) samples. The material specific abbreviations are listen in Table 4.1. The following example shows the naming of a calcined 4th SAPO-5 sample: S5-4c.

Table 4.1: Abbreviations used for the various materials in this thesis.

Material	Abbreviated name
Silicalite-1	S1
AlPO-5	A5
SAPO-5	S5
SBA-15	S15
Silica Aerogel	SAG
Silica Xerogel	SXG

4.1.1 SAPO-5 and AlPO-5

A summary of XRD and N_2 physisorption results for all synthesized AFI-type zeotypes is given in Table 4.2. For the SAPO-5 samples the common contaminant

phase was CHA, corresponding to presence of SAPO-34, with the exception of S5-6, which possessed a SAPO-5 and a Boehmite phase. Both increase of hydrothermal crystallization time and increased water content appear to promote SAPO-34 formation. For the AlPO-5 samples all contaminants were from Boehmite. The XRD of S5-4as is given in Figure 4.1 as a typical example of SAPO-34 contamined SAPO-5. S5-7 was phase pure AFI, which prompted 4 samples of same reactant ratios to be synthesized, S5-11 to S5-14, the XRD of S5-7 is given in Figure 4.2. Synthesis ratios for all AFI-type zeotypes are found in Table 3.1.
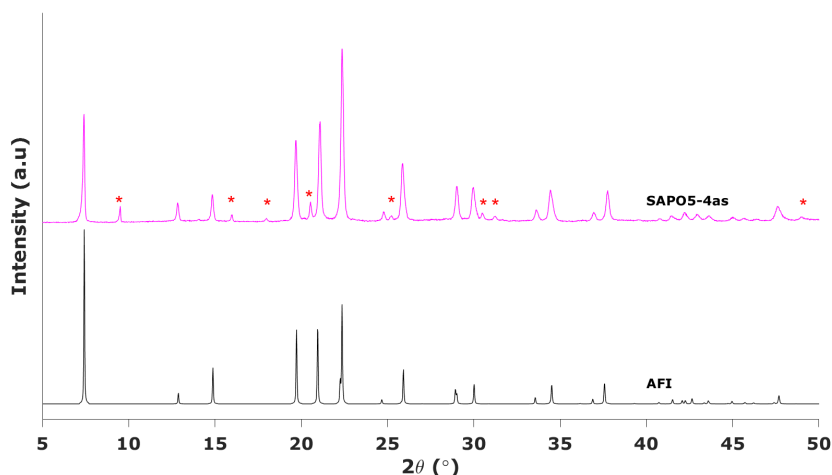
Figure 4.1: PXRD of as synthesized SAPO-5 (S5-4as) with a foreign phase and theoretical diffractogram of AFI phase (AFI).

N_2 physisorption of the SAPO-5 (S5-11c) had a isotherm reminiscent of the Type I typically expected of microporous solids with small external surfaces. The hysteresis appear as a H4 type associated with narrow slit-like pores for Type I isotherm.[81] The BJH inset shows no clear mesopores in the material. The N_2 physisorption isotherms and the pore size distribution is shown in Figure 4.3.

The N_2 physisorption isotherms and pore size distribution for the AlPO-5 (A5-5c) is similar to the isotherm of the SAPO-5 with a Type I isotherm and a H4 hysteresis, however the hysteresis of the AlPO-5 larger at higher relative pressure compared to the hysteresis of the SAPO-5. The BJH inset shows no clear mesopores in the material. The N_2 physisorption isotherms and the pore size distribution is shown in Figure 4.4.

SAPO-5 and AlPO-5 samples had SEM performed to gain an indication of particle
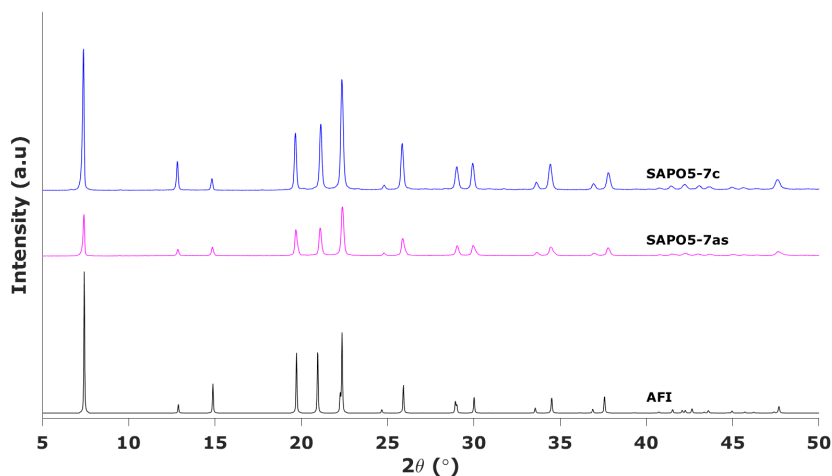
Figure 4.2: PXRD of phase pure SAPO-5, both as synthezised (S5-7as) and calcined (S5-7c)[a]. The reference theoretical diffractogram of an AFI-phase is also included for comparison.

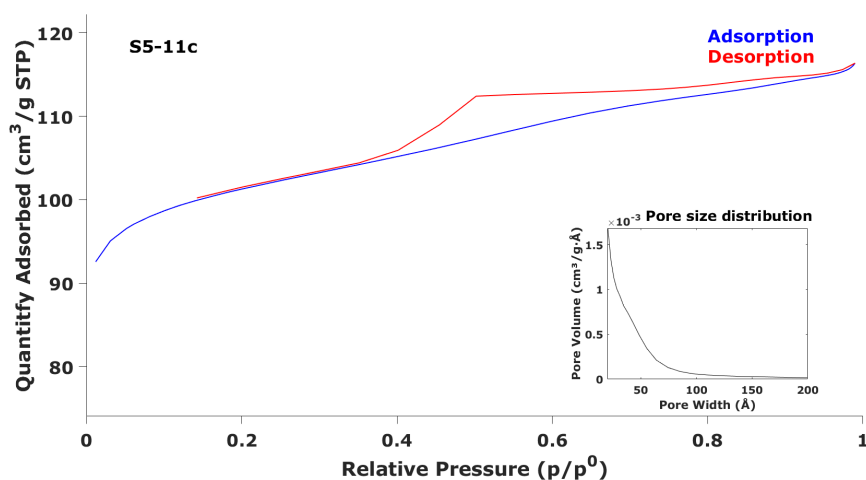[a]Intensity increase due to instrument reconfiguration.

Figure 4.3: The N_2 adsorption isotherms for SAPO5 (S5-11c) with a BJH adsorption based pore size distribution inset.

size. The SEM of SAPO-5 and AlPO-5 are given in Figure 4.5 and Figure 4.6 respectively. The SAPO-5 particles are varied in size, with several large particles around 30 µm diameter and some aggregates of smaller particles. These types of aggregates are considered the cause of the H4 hysteresis type. The AlPO-5 particles appear very similar to the SAPO-5, the primary difference is the longer rod-like

38
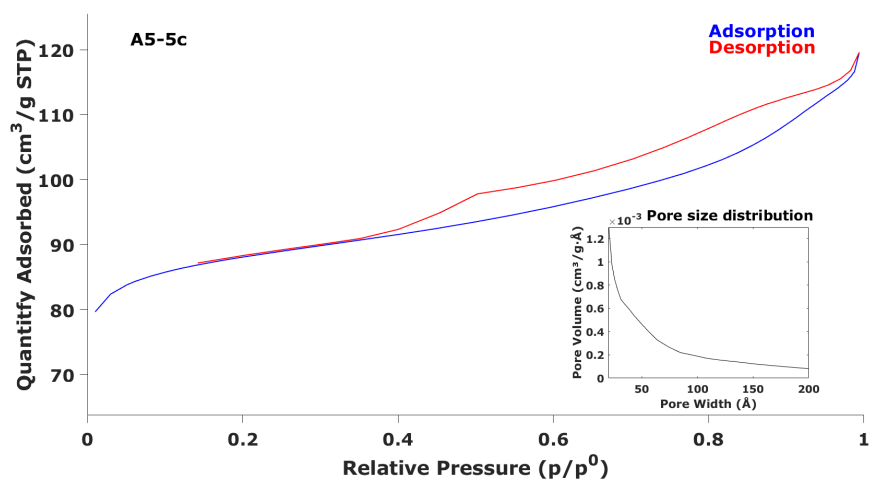
Figure 4.4: The N_2 adsorption isotherms for AlPO5 (A5-5c) with a BJH adsorption based pore size distribution inset.
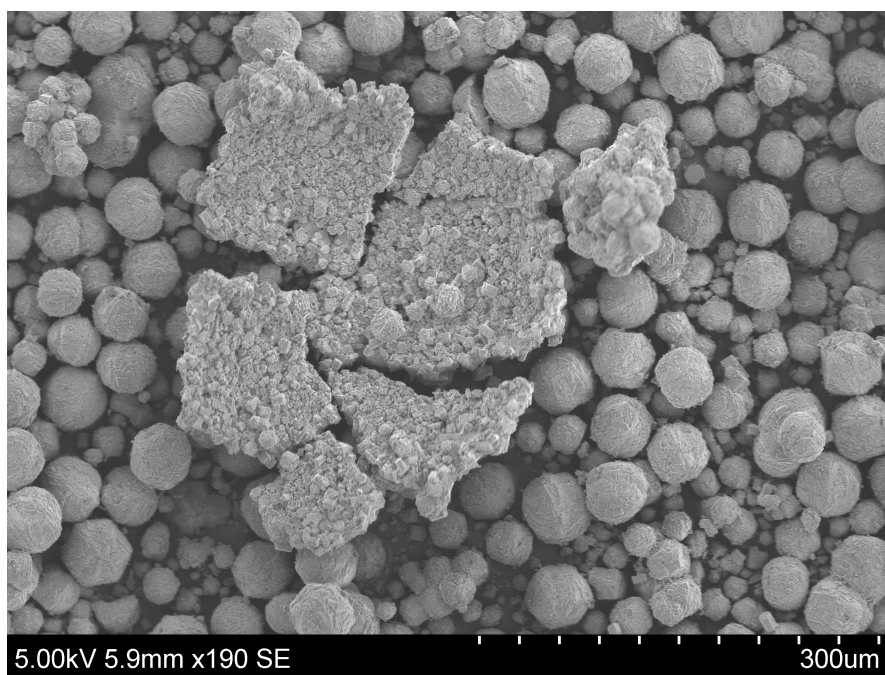
particle aggregates.

Figure 4.5: SEM image with a 190x magnification of a SAPO-5 sample.

Table 4.2: Phase, specific surface area, and pore volume for all synthesized SAPO-5 (S5) and AlPO-5 (A5) materials.

Sample ID	Phase^a	S$_{\text{BET}}$^{b}	Micropore volume [cm^3 g^{-1}]^c
S5-1	AFI+CHA	-	-
S5-2	AFI + Boehmite	-	-
S5-3	AFI+Boehmite	-	-
S5-4	AFI + Boehmite	-	-
S5-5	AFI+CHA	-	-
S5-6	AFI + Boehmite	-	-
S5-7	AFI	-	-
S5-8	AFI+CHA	-	-
S5-9	AFI+CHA	-	-
S5-10	AFI+CHA(-)	-	-
S5-11	AFI	314	0.132
S5-12	AFI	282	0.112
S5-13	AFI	316	0.135
S5-14	AFI	309	0.131
A5-1	AFI+Boehmite	-	-
A5-2	AFI+Boehmite	-	-
A5-3	AFI	-	-
A5-4	AFI+CHA(-)	-	-
A5-5	AFI	274	0.114
A5-6	AFI	297	0.125
A5-7	AFI	282	0.117

^{a}(-) indicate a negligible phase based on intensity of peaks
^{b}BET derived surface area measurement
^{c}Based on t-plot

3.00kV 5.8mm x190 SE   300um
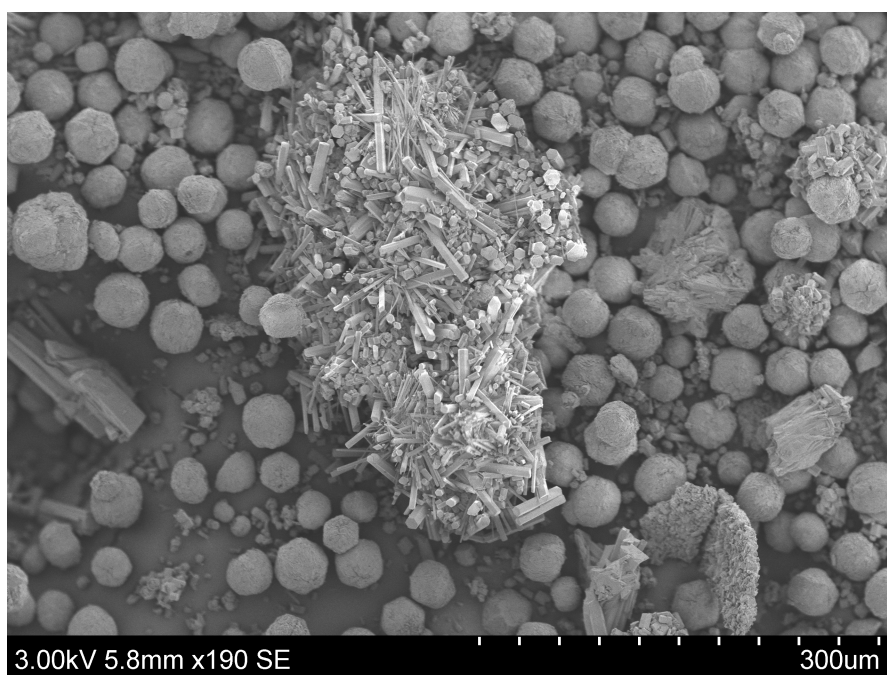
Figure 4.6: SEM image with a 190x magnification of a AlPO-5 sample.

4.1.2 Silicalite-1

A summary of XRD and N_2 physisorption for all silicalite-1 samples is given in Table 4.3. The synthesis using Ludox AS-40 as Si-source yielded phase-pure Silicalite-1, however when using TEOS as Si-source the product was amorphous. PXRD of Silicalite-1 synthesized using TEOS is given in Figure 4.7, the as synthesized and calcined silicalite-1 synthesized with Ludox is given in Figure 4.8 and Figure 4.9 respectively.

Table 4.3: Phase, specific surface area, and micropore volume for all synthesized Silicalite-1 (S1) samples.

Sample ID	Phase	S_{BET}[a] $[m^2\,g^{-1}]$	Micropore volume $[cm^3\,g^{-1}]$[b]
S1-1	Amorphous	-	-
S1-2	Amorphous	-	-
S1-3	MFI	358	0.166
S1-4	MFI	341	0.166

[a]BET derived surface area measurement
[b]Determined by t-plot
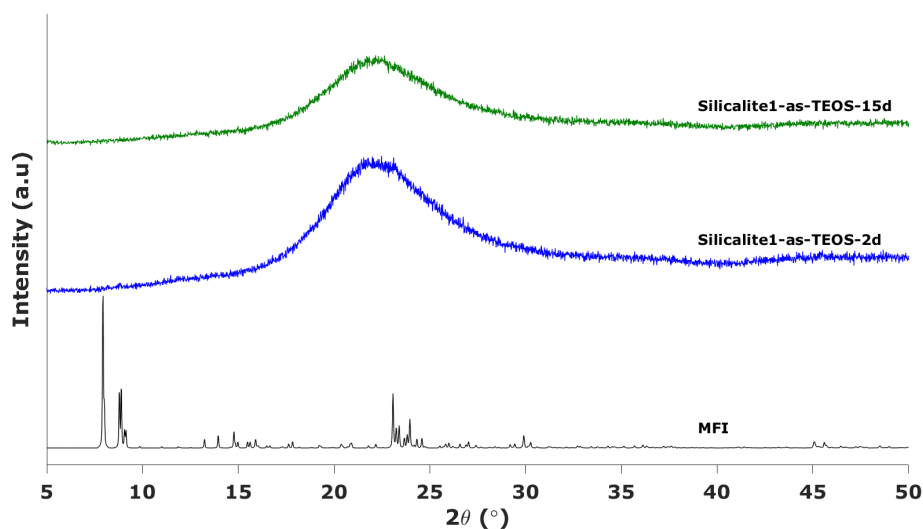
Figure 4.7: PXRD of both silicalite-1 samples (S1-1 and S1-2) synthesized with TEOS as the Si-source, with the associated framework (MFI) displayed at the bottom.
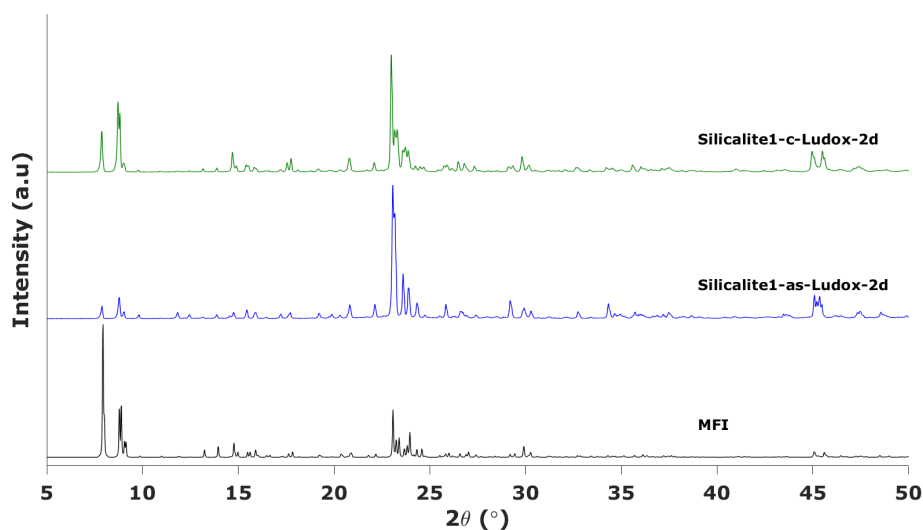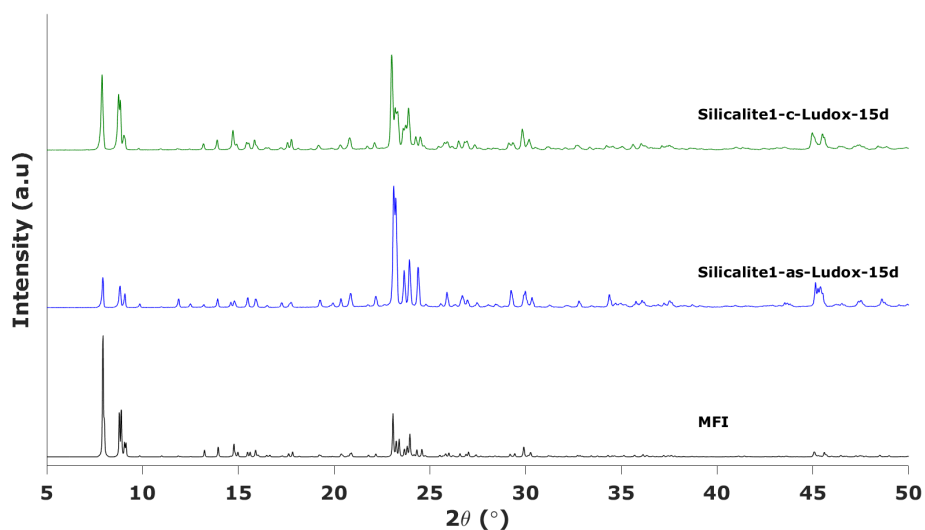
Figure 4.8: PXRD of as-synthesized (as) and calcined (c) silicalite-1 (S1-3) with associated framework (MFI). Si-source was colloidal silica (Ludox AS-40) with a 2 d hydrothermal crystallization time.

S1-1as and S1-2as were discarded due to amorphous phase present in the diffractogram, shown in Figure 4.7. As the only samples with correct phase, both S1-3 and S1-4 were calcined and subjected to N_2 adsorption measurements. The adsorption isotherm and pore distribution for S1-3 and S1-4 is given in Figure 4.10 and Figure 4.11, respectively. The stepped isotherm of both S1-3 and S1-4 is due to a densification of adsorbate previously reported for silicalite-1.[82] The crystalline samples had a specific surface area of approximately $350\,\mathrm{m^2\,g^{-1}}$, within the previously reported range of $350\text{-}450\,\mathrm{m^2\,g^{-1}}$.[83]

The pore size distribution verify that synthesized materials are microporous due to lack of significant pores volumes above 2 nm. The stepped isotherm required a more limited V-t (t-plot) range, from 0.16 to 0.65 p/p$_0$. The limited V-t range yielded a micropore volume of $0.166\,\mathrm{cm^3\,g^{-1}}$.

Figure 4.9: PXRD of as-synthesized (as) and calcined (c) silicalite-1 (S1-4) with associated framework (MFI). Si-source was colloidal silica (Ludox AS-40) with a 15 d hydrothermal crystallization time.
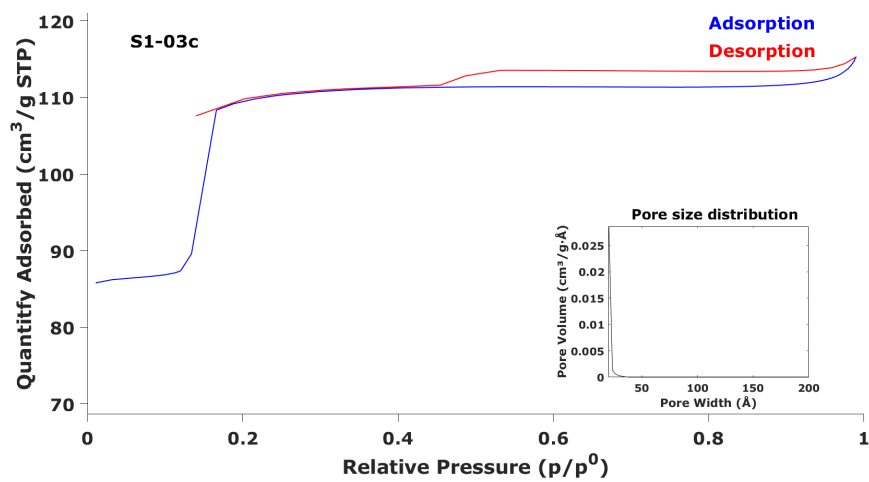

Figure 4.10: The N_2 adsorption isotherms for S1-3c (Silicalite-1 sample 3, calcined) with a BJH adsorption based pore size distribution inset.
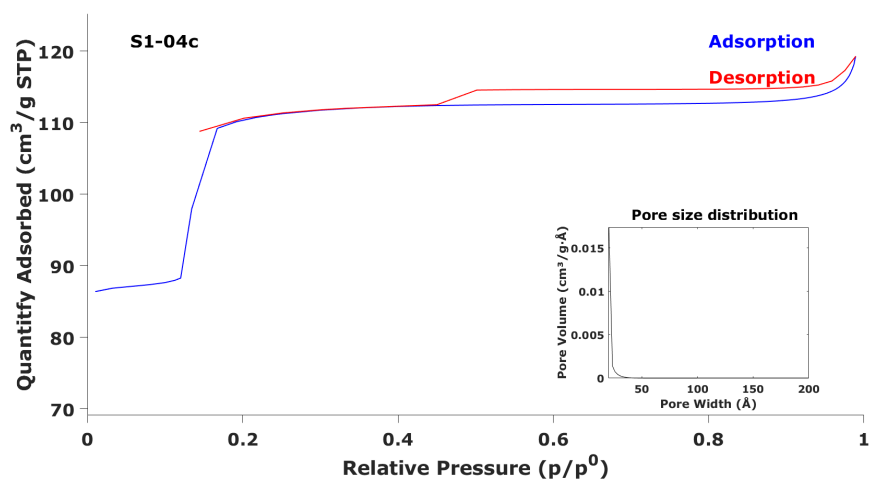
44

Figure 4.11: The N_2 adsorption isotherms for S1-4c (Silicalite-1 sample 4, calcined) with a BJH adsorption based pore size distribution inset.

4.1.3 SBA-15

All PXRD of the SBA-15 samples were considered amorphous due to the absence of sharp distinct reflections, indicating a lack of long range order. The broad reflection centered at 23° corresponds to an amorphous phase due to short-range ordering of the silica. An example of a typical diffractogram for SBA-15 samples are shown in Figure 4.12.
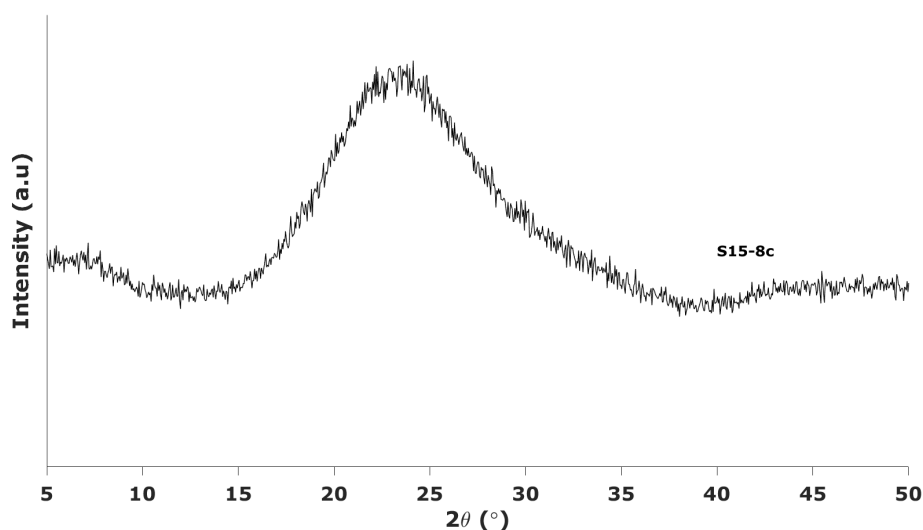

Figure 4.12: X-ray diffractogram of SBA-15 (S15-8c) between 5-50°.

Surface area and pore size for all synthesized SBA-15 samples is given in Table 4.4. Comparing the methods it is clear that synthesis method 1 produce SBA-15 with significantly higher surface area, while method 2 produce SBA-15 with larger average pore sizes. Method 1 was deemed most suited for further use, due to increased surface area and no requirement for pores larger than those obtained with method 1. An example of adsorption isotherm and pore size distribution for the SBA-15 samples are given in Figure 4.13.

As SBA-15 normally have a surface area between 600-1000 $m^2 g^{-1}$ [41] the SBA-15 synthesized via method 1 can be considered a higher surface area SBA-15. The surface area obtained with method 2 is within range, however is within the lower acceptable range for a SBA-15.
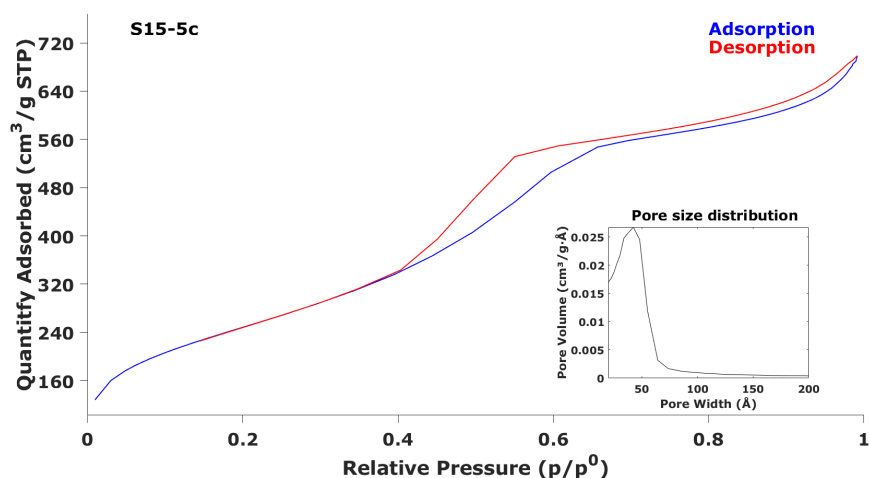
46

Figure 4.13: The N_2 adsorption isotherms for SBA-15 (SBA15-5c) with a BJH adsorption base pore size distribution inset.

Table 4.4: BET surface area, average pore size, and pore volumes for all synthesized SBA-15 samples after calcination.

Sample ID	$S_{BET}{}^a$ ($m^2 g^{-1}$)	Avg. Pore size[b] (Å)	Pore volume[c] ($cm^3 g^{-1}$)
S15-1c	796	35.6	0.83
S15-2c	865	33.4	0.75
S15-3c	603	49.9	0.91
S15-4c	601	49.4	0.91
S15-5c	910	43.8	1.15
S15-6c	891	37.1	0.87
S15-7c	871	37.1	0.83
S15-8c	859	40.1	0.94
S15-9c	828	32.8	0.61
S15-10c	825	34.2	0.61

[a]BET derived surface area measurement
[b]Based on BJH adsorption
[c]Based on BJH adsorption cumulative pore area between 17 Å and 3000 Å

4.1.4 Silica Aerogel and Xerogel

PXRD of silica aerogel and xerogel were considered amorpohus due to absence of sharp distinct reflections, PXRD of silica aerogel and one silica xerogel sample is shown in Figure 4.14 and Figure 4.15 respectively. The broad reflection centered at 23° correspond to the short-range ordering of the silica network.
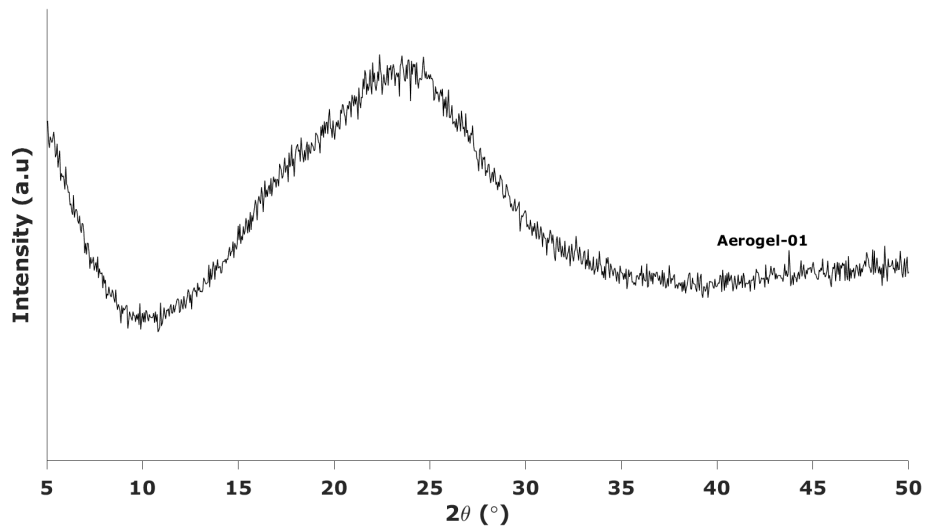
Figure 4.14: PXRD of a silica aerogel (Aerogel-01) synthesized using the APD method.
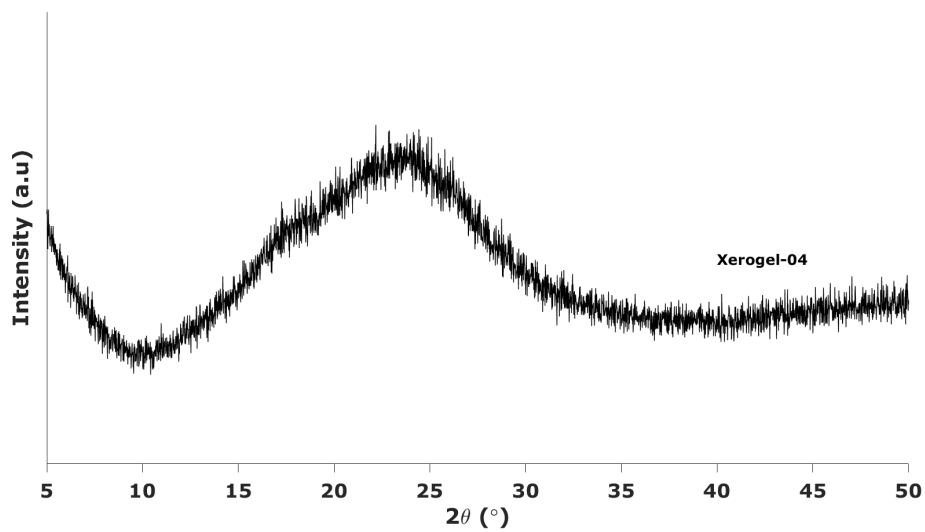

Figure 4.15: PXRD of a silica xerogel (Xerogel-04) synthesized by deliberate collapse of wet silica aerogel network.

Surface area and pore size for all synthesized aerogel and xerogel samples is given in Table 4.5. No plots of isotherms are given for neither aerogel or xerogel due to a non-closing loop consistant for all samples.

Table 4.5: BET surface area and the average pore size of all synthesized silica aerogel and silica xerogel samples.

Sample	$S_{BET}{}^a$ ($m^2\,g^{-1}$)	Avg. pore diameter^b ($m^2\,g^{-1}$)
Aerogel-01	691	33.8
Xerogel-01	46	195.0
Xerogel-02	394	59.6
Xerogel-03	390	67.7
Xerogel-04	538	36.2

^{a}BET derived surface area measurement
^{b}Based on BJH adsorption

4.2 Surface modification

The samples with the highest surface area, most suitable pore distribution, and correct phase was chosen for the surface-functionalization with APTES. From this point the naming of samples have also been simplified to denote the materials, but removing the synthesis number and heat treatment. Materials with multiple samples have been given a small differentiation in the simplified name which reflect the difference between these samples. A list of all simplified names is given in Table 4.6, with a note indicating difference between samples using the same material support.

Table 4.6: Overview of synthesis names and the corresponding new simplified names used after post-synthetic surface modification.

Material	Synthesis name	Simplified name	Note
SBA-15	S15-5c-NH$_2$	SBA15-0.1AP	10% APTES added
SBA-15	S15-6c-NH$_2$	SBA15-AP-T	Test of APTES reaction
SBA-15	S15-8c-NH$_2$	SBA15-AP	
SBA-15	S15-9c-NH$_2$	SBA15-AP-L	Larger amount modified
Silica Aerogel	SAG-01-NH$_2$	Aerogel-AP	
Silica Xerogel	SXG-04-NH$_2$	Xerogel-AP	
SAPO-5	S5-11c-NH$_2$	SAPO5-AP	
AlPO-5	A5-5c-NH$_2$	AlPO5-AP	

The effect of APTES modification of the materials was investigated by both PXRD and N_2 physisorption. From the PXRD all materials retained the crystalline phase (or amorphous phase) of the unmodified material.

The surface area and pore volumes of all materials was significantly changed by the surface reaction with APTES. The changes to the surface area and pore volumes is illustrated in Figure 4.16 and Figure 4.17 respectively. The decrease in surface area for all the mesoporous materials is illustrated in Figure 4.18.
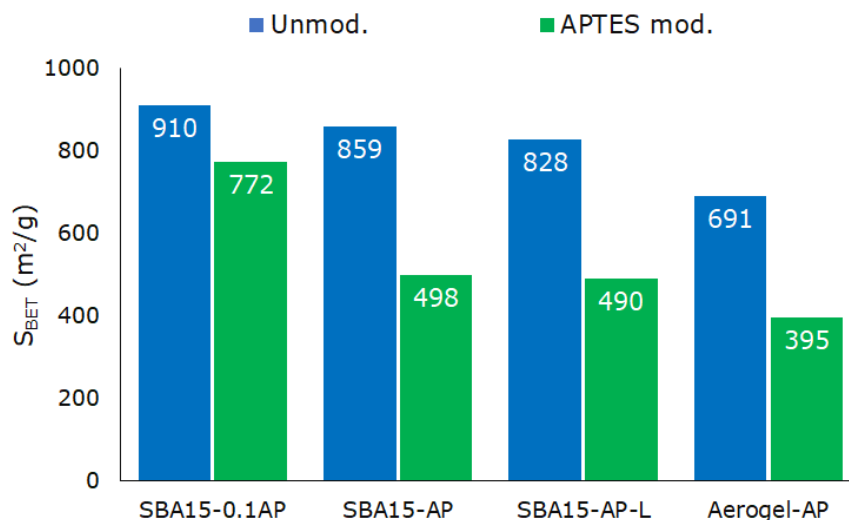

Figure 4.16: N_2 physisorption results for mesoporous samples, comparing the total surface area (S_{BET}) of the unmodified materials and APTES modified materials.

For the mesoporous materials the introduction of the aminopropyl (AP) group via APTES appear to cover some surfaces, seem by the reduced surface area and pore volumes, but the pore systems remain intact. During suspension of the Aerogel is returned to a gel, the drying of this gel was consistent with the drying of the other materials. The change in both surface area and pore volume for the Aerogel can arise from the APTES surface modification or from the new drying process of the gel, however as the reduction in surface area appear consistent with the SBA-15, the reduction will be considered as a result of APTES surface modification, not as a result of the new drying procedure.

The microporous materials, the SAPO-5, AlPO-5, Silicalite-1 and Xerogel, had varying results from the introduction of the APTES. For the SAPO-5 the APTES modified sample turned non-porous, with the micropore surface area approaching zero. Both the AlPO-5 and the Silicalite-1 had a decrease in micropore surface area. The Xerogel experienced an increase in micropore surface area. The increase of micropore surface area for the xerogel could be due to drying procedure, as the xerogel returned to a gel in the solution like previously described for the aerogel.
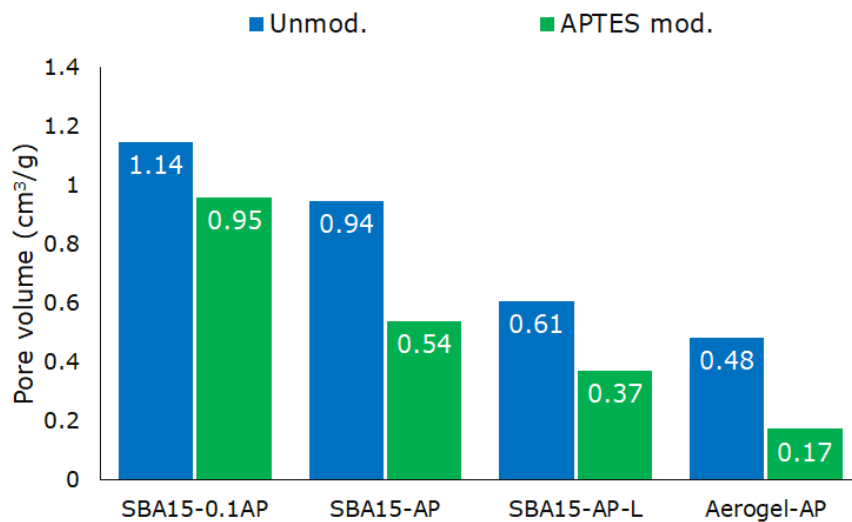
Figure 4.17: N_2 physisorption results for mesoporous samples, comparing the BJH adsorption based pore volume of the unmodified materials and APTES modified materials.
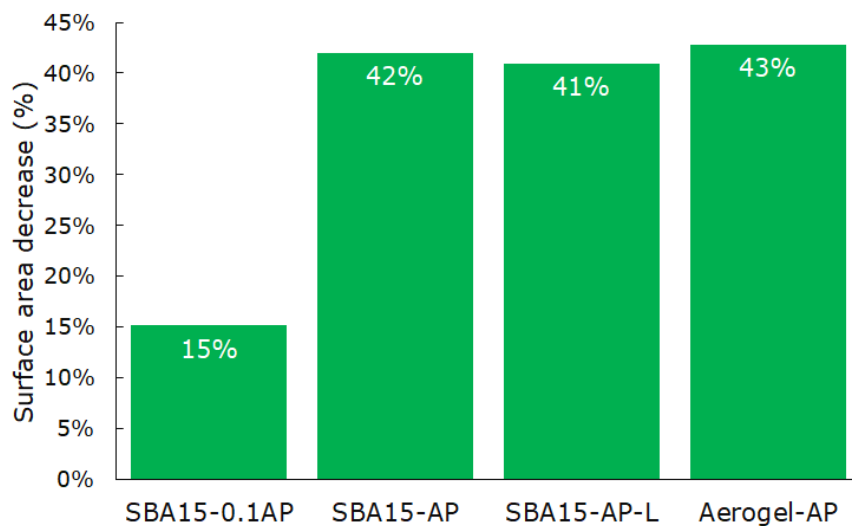

Figure 4.18: The decrease in total surface area, determined from BET, for APTES modified samples.

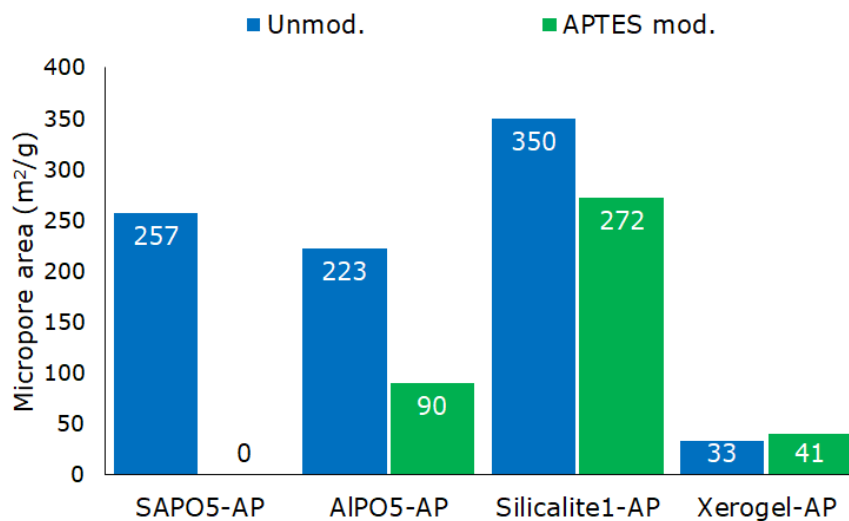Decrease in micropore surface area is illustrated in Figure 4.21.

Figure 4.19: N_2 physisorption results for microporous samples, comparing the t-plot based microporous surface area of the unmodified materials and APTES modified materials.
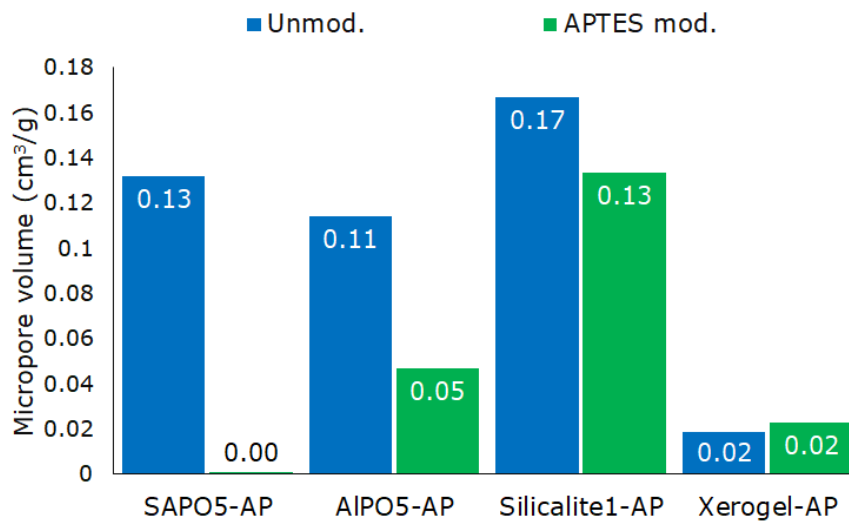

Figure 4.20: N_2 physisorption results for microporous samples, comparing the t-plot based microporous volume of the unmodified materials and APTES modified materials.
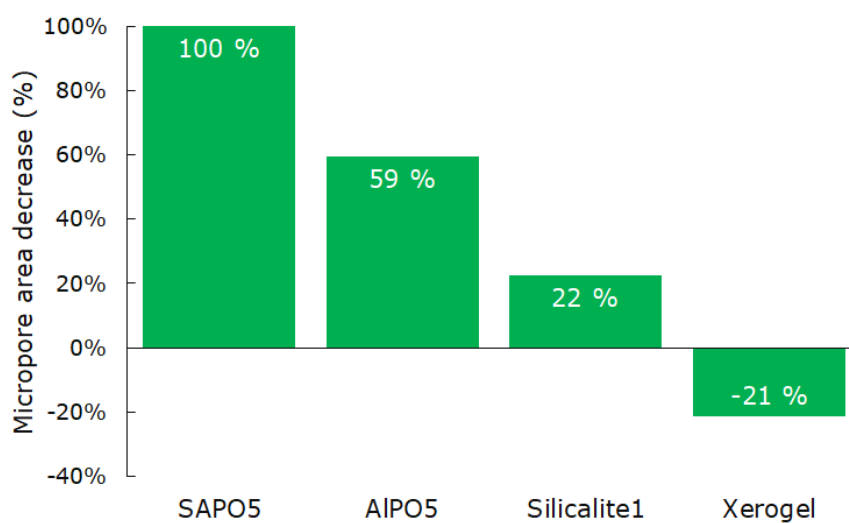
Figure 4.21: The decrease in micropore surface area, determined from t-plot method, for APTES modified samples.

4.2.1 TGA/MS

TGA/MS was applied to two samples, SBA15-AP and Aerogel-AP, to determine the amount of APTES that reacted with these samples. The SBA15-AP appear to have $1.042\,\mathrm{mmol\,g^{-1}}$ loading, significantly lower then the maximum loading of $4.985\,\mathrm{mmol\,g^{-1}}$. The Aerogel-AP had a higher APTES loading of $1.986\,\mathrm{mmol\,g^{-1}}$ and a maximum loading of $4.924\,\mathrm{mmol\,g^{-1}}$. An important factor for the Aerogel is that this TGA-based method will include any silylation groups that are removed around the same temperature as the AP groups, which leads the Aerogel value to be inflated. The APTES determination results are found in Table 4.7, while the TGA plots are given in Figure 4.22 and Figure 4.23 for the SBA15-AP and Aerogel-AP respectively.

Table 4.7: The loading of the APTES in an SBA-15 and a silica aerogel based on TGA/MS using the mass of the leaving aminopropyl group. For reference the mass loss % and the maximum theoretical APTES loading based on synthesis addition is included for both samples.

Sample	Mass loss (%)	Loading ($\mathrm{mmol\,g^{-1}}$)	Maximum loading[a] ($\mathrm{mmol\,g^{-1}}$)
SBA15-AP	6.16	1.042	4.985
Aerogel-AP	11.74	1.986	4.924

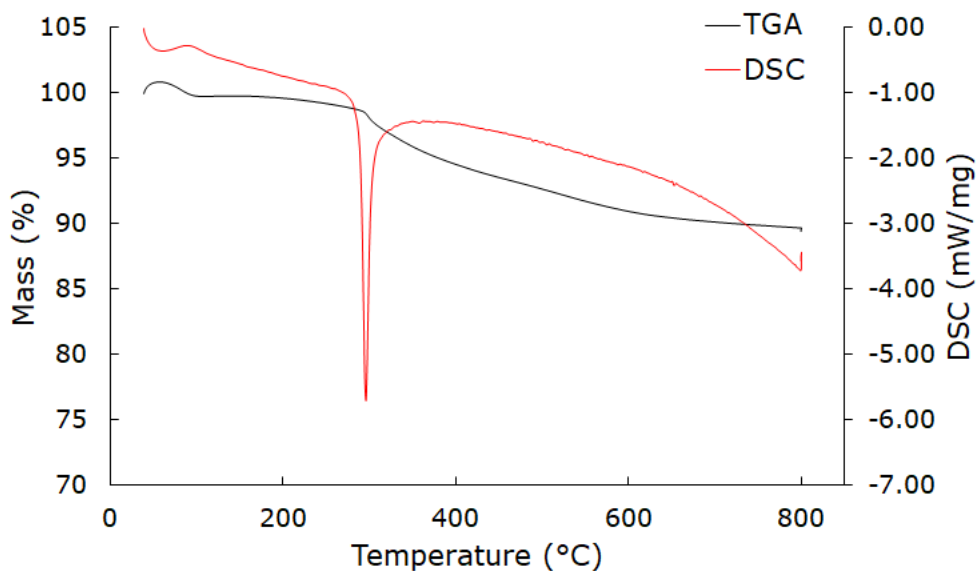[a]Based on synthesis addition

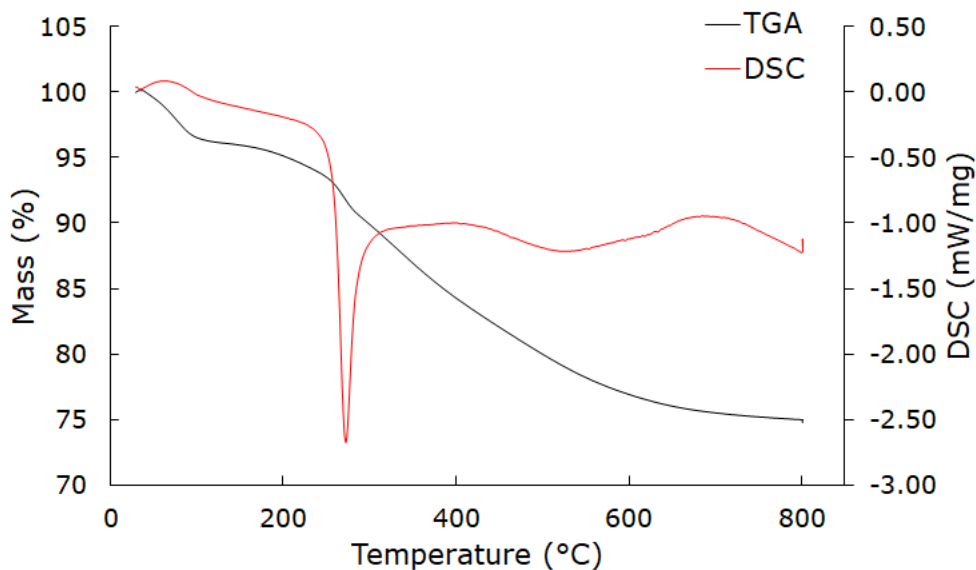**Figure 4.22:** TGA and DSC plot of the SBA15-AP.

Figure 4.23: TGA and DSC plot of the Aerogel-AP.

4.2.2 Investigation of SAPO-5 pore blockage

The removal of the SAPO-5 pore system was discovered by the N_2 physisorption experiments. Since the physisorption cannot determine if the blockage is local to

55

the pore openings or systemic to the SAPO-5 pores, another method was employed to investigate the internal structure in the SAPO-5. Using IR, in DRIFTS, the presence of the brønsted acid sites in both materials were detected.

The presence of the Brønsted acid sites can indicate if the blockage mechanism is by creating a physical APTES plug on the entrance of the pores, a complete pore blockage by the APTES, or by cokeing of the pores by reacting the ethanol byproduct from the APTES with the toluene to synthesize *p*-ethyltoluene, a reaction catalyzed by brønsted acid containing zeolites. [84,85]

The complete FTIR spectra of the dehydrated samples are shown in Figure 4.24, however as we are looking at Brønsted acid sites the 3500-4000 cm^{-1} range of fundamental OH stretching vibrations can be used. A spectra directed at the 3400-3700 cm^{-1} range is shown in Figure 4.25.
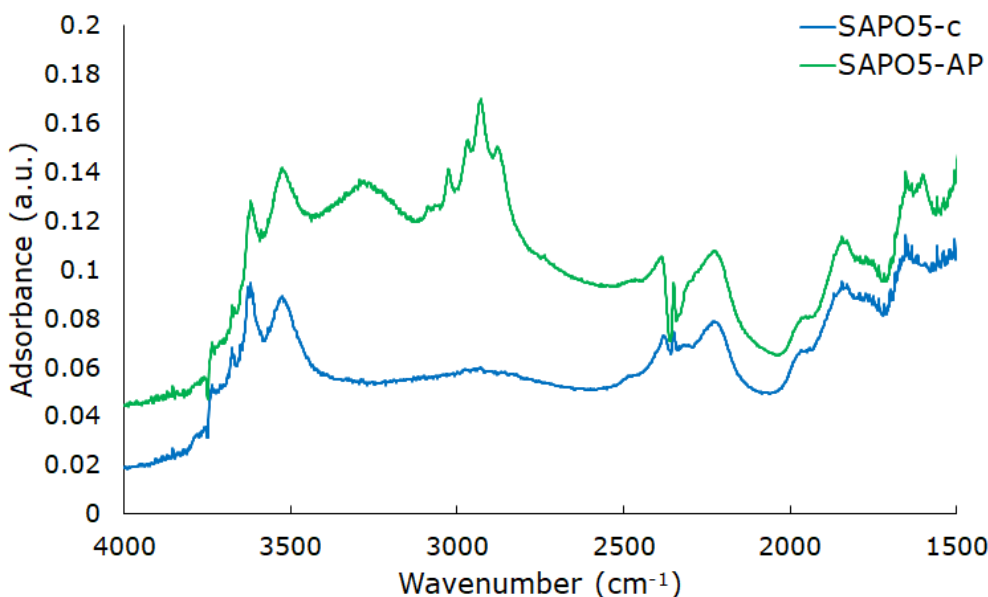

Figure 4.24: FTIR spectra of SAPO5-c and SAPO5-AP at 150 °C in He atmosphere.

In the SAPO-5 framework brønsted acid sites should appear at both 3625 cm^{-1} and 3520 cm^{-1}. These two bands represent two modes of Si-OH-Al, the 3625 cm^{-1} is characteristic for undisturbed Si-OH-Al groups while the 3520 cm^{-1} band is characteristic of Si-OH-Al groups interacting with framework oxygen's. [86] From Figure 4.25 both the 3625 cm^{-1} and 3520 cm^{-1} bands are present for both the un-modified SAPO-5 (SAPO5-c) and the APTES modified SAPO-5 (SAPO5-AP).
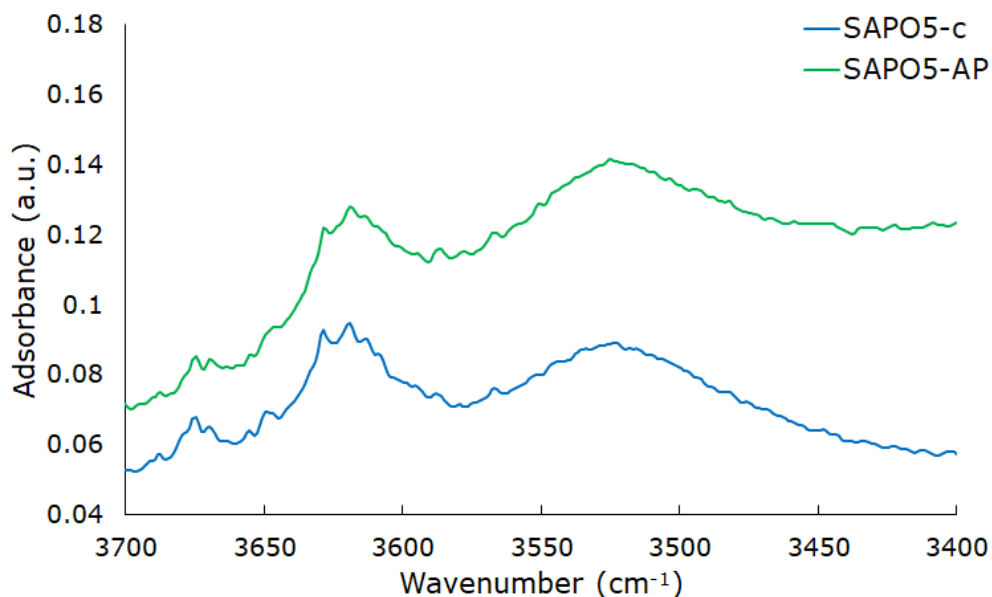
Figure 4.25: FTIR spectra on area centered around the Brønsted acid sites of SAPO5-c and SAPO5-AP at 150 °C in He atmosphere.

As no change in brønsted acid sites was detected a look at the full FTIR spectra over various temperatures would differentiate between the blockage being due to *p*-ethyltoluene cokeing or APTES plug. The spectra at various temperatures indicate that *p*-ethyltoluene is not precent in the SAPO5-AP sample due to no changes over the 100-200 °C range while the *p*-ethyltoluene has a boiling point of 162 °C.[69] As there is no indication of *p*-ethyltoluene in the sample the APTES plug is the best explaination for the blocked pore network. An illustration of the FTIR spectra at 100 °C, 150 °C, and 200 °C is given in Figure 4.26.
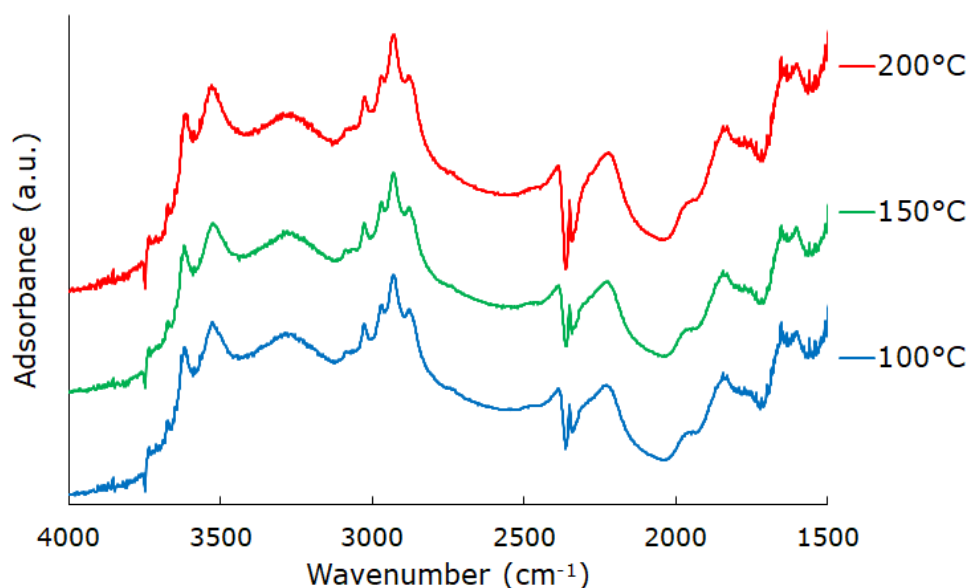
Figure 4.26: Stacked plot of the FTIR spectra of a APTES modified SAPO5 at 100 °C, 150 °C, and 200 °C in a He atmosphere

4.3 Rhenium introduction

Rhenium introduced samples are named in accordance with Table 4.6 with an addition of "Re" in the naming, e.g. SBA15-AP becomes SBA15-AP/Re.

The introduction of rhenium on the surface modified supports was an exceptional success with up to 9.4 wt.% loading for the SBA-15, which is 188 times more than a preceding masterstudent achieved on an ion-exchanged SBA-15.[14] The rhenium loading for based on ICP-MS and theoretical loading based on synthesis additions for all samples are shown in Figure 4.27 and Table 4.8. The three mesoporous SBA-15 samples had remarkably high loading with 7.5-9.5 wt.% rhenium adsorbed, between 70-83 % of their theoretical maximum loading.

Both the Aerogel and Xerogel also adsorbed significant amounts of Rhenium, 6.5 wt.% and 8.8 wt% respectively. The gel which adsorbed the most Rhenium was the Xerogel, with 82 % relative maximum loading compared to the Aerogel with 54 % relative maximum loading.

The rhenium introduction introduced no new reflections on the diffractograms of the samples. The SAPO-5 and AlPO-5 samples maintained the AFI frame-
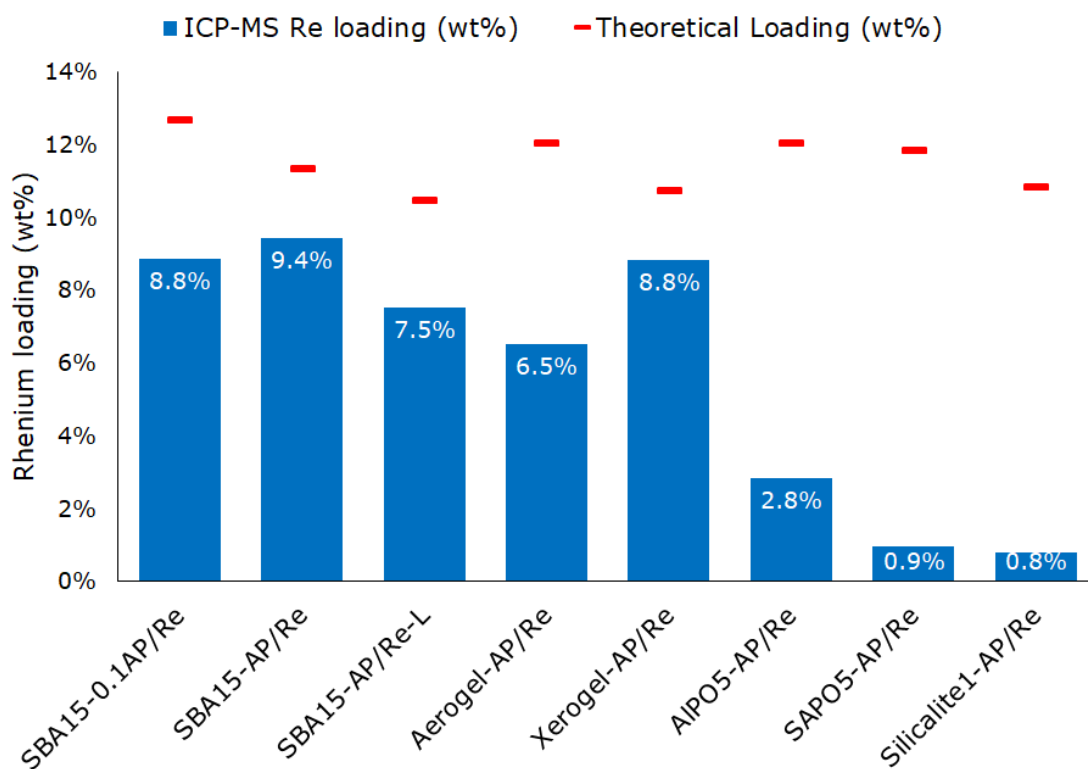
Figure 4.27: Theoretical and actual loading of rhenium on the aminopropyl modified materials. Actual loading determined by ICP-MS analysis.

Table 4.8: The rhenium amount in samples determined by ICP-MS analysis, the relative load of rhenium for each sample, and the maximum rhenium load for all samples.

Sample	Rhenium load^a (mmol g^{-1})	Relative load (wt%)	Max load^b (wt%)
SBA15-0.1AP/Re	88.50	8.85	12.67
SBA15-AP/Re	94.35	9.43	11.33
SBA15-AP/Re-L	75.35	7.54	10.46
Aerogel-AP/Re	65.05	6.51	12.03
Xerogel-AP/Re	88.27	8.83	10.73
AlPO5-AP/Re	28.42	2.84	12.03
SAPO5-AP/Re	9.50	0.95	11.85
Silicalite1-AP/Re	8.07	0.81	10.85

^{a}Determined by ICP-MS
^{b}Based on amount Re$_2$O$_7$ added to solution

work throughout both the AP modification and the rhenium introduction. The diffractogram of SAPO-5 and AlPO-5 are shown in Figure 4.28 and Figure 4.29 respectively.
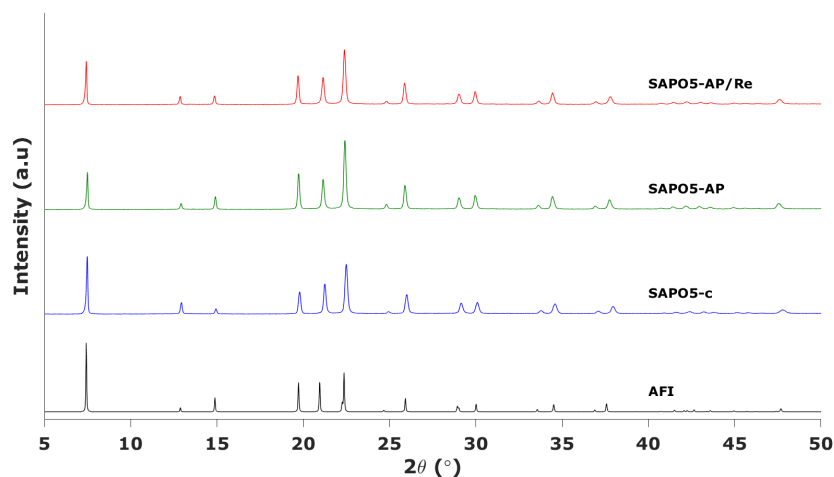

Figure 4.28: Diffractogram pattern of SAPO-5 with calcined (c), aminopropyl modified (AP), and rhenium introduced sample (AP/Re) with the theoretical AFI diffractogram pattern.

Figure 4.29: Diffractogram pattern of AlPO-5 with calcined (c), aminopropyl modified (AP), and rhenium introduced sample (AP/Re) with the theoretical AFI diffractogram pattern.
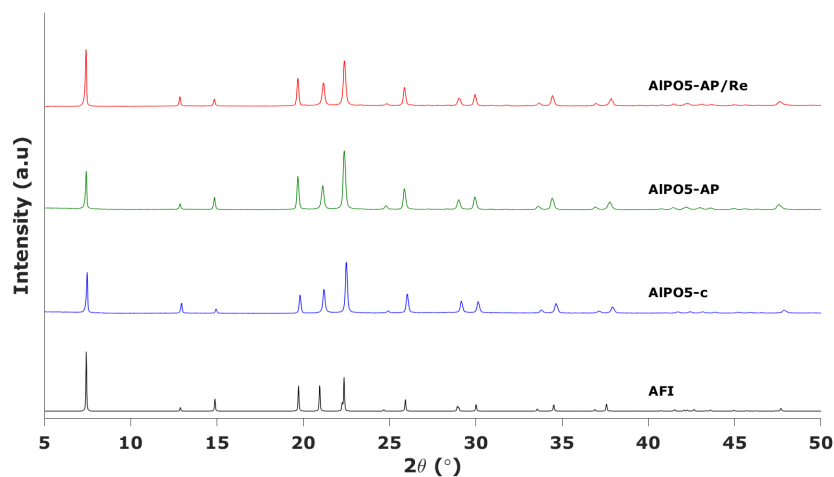
The silicalite-1 sample had similar results in the diffractogram as the AFI zeotypes, with the MFI framework present for calcined, AP modified and rhenium introduced. No new reflections occur after these treatments. The diffractogram of silicalite-1 is shown in Figure 4.30.
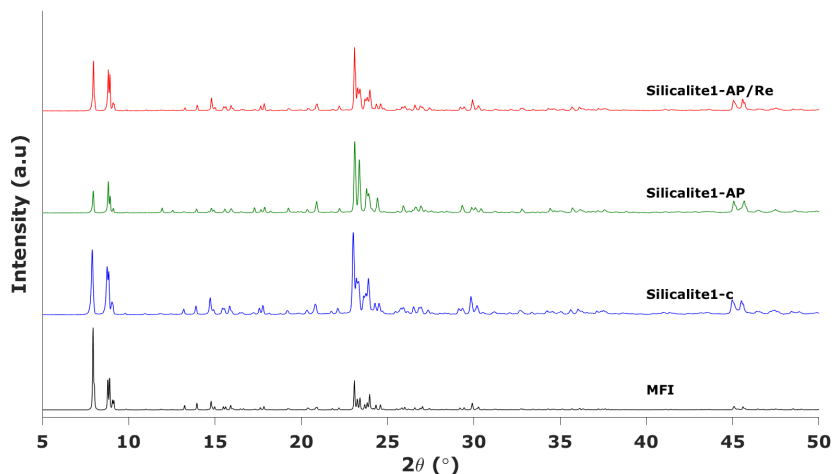

Figure 4.30: Diffractogram pattern of silicalite-1 with calcined (c), aminopropyl modified (AP), and rhenium introduced sample (AP/Re) with the theoretical MFI diffractogram pattern.

The aerogel and xerogel materials showed no new reflections in the diffractograms, maintaining the amorphous diffraction pattern of the original materials. The diffractograms of the aerogel and the xerogel is shown in Figure 4.31 and Figure 4.32.

The three SBA-15 samples show similar diffractograms as the aerogel and xerogel samples. All SBA-15 samples display the amorphous diffraction pattern of the calcined material. The SBA15-0.1AP/Re, SBA15-AP/RE, and SBA15-AP/RE-L are shown in Figure 4.33, Figure 4.34, and Figure 4.35 respectively.

After the rhenium introduction new N_2 physisorption measurements was performed to observe if rhenium introduction caused changes in the pore system. The SBA-15 samples continue a increase in the surface area and pore volume after rhenium introduction. The Aerogel sample has a significant increase in both surface area and pore volume almost back to the values in the unmodified material. The mesoporous surface area and pore volumes are illustrated in Figure 4.36 and Figure 4.37 respectively.
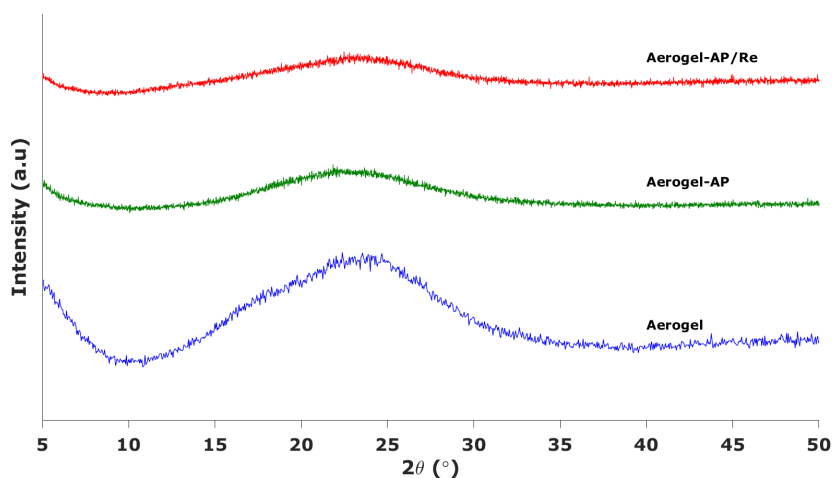
Figure 4.31: Diffractogram pattern of silica aerogel with as synthesized, aminopropyl modified (AP), and rhenium introduced sample (AP/Re).
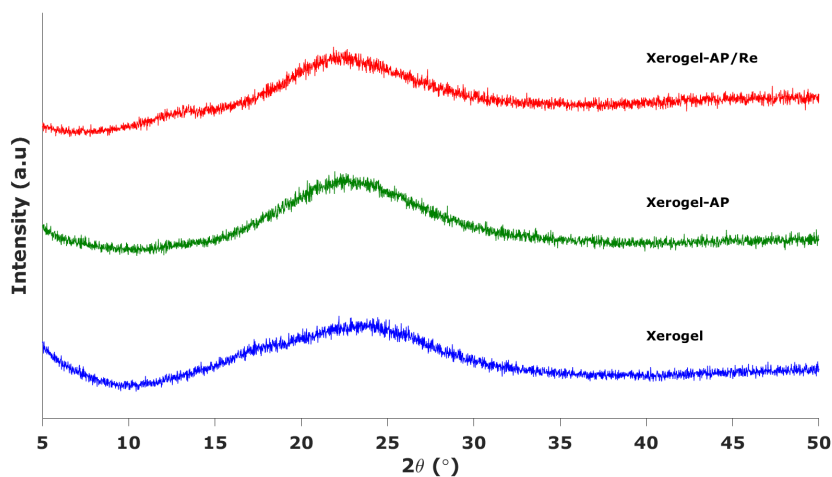
Figure 4.32: Diffractogram pattern of silica xerogel with as synthesized, aminopropyl modified (AP), and rhenium introduced sample (AP/Re).

Only the AlPO-5 and the Silicalite-1 had a enough sample to perform a last N_2 physisorption measurement. The AlPO-5 had a very mall decrease in both surface area and pore volume from the APTES modified sample. The Silicalite-1 had an increase in surface area and pore volume similar to that seen in the Aerogel, where the surface area and pore volume is almost back to the values of the unmodified material. The microporous surface area and pore volumes are illustrated in Figure 4.38 and Figure 4.39 respectively.

Figure 4.33: Diffractogram pattern of the SBA15-0.1AP/Re with calcined (c), aminopropyl modified (AP), and rhenium introduced sample (AP/Re).
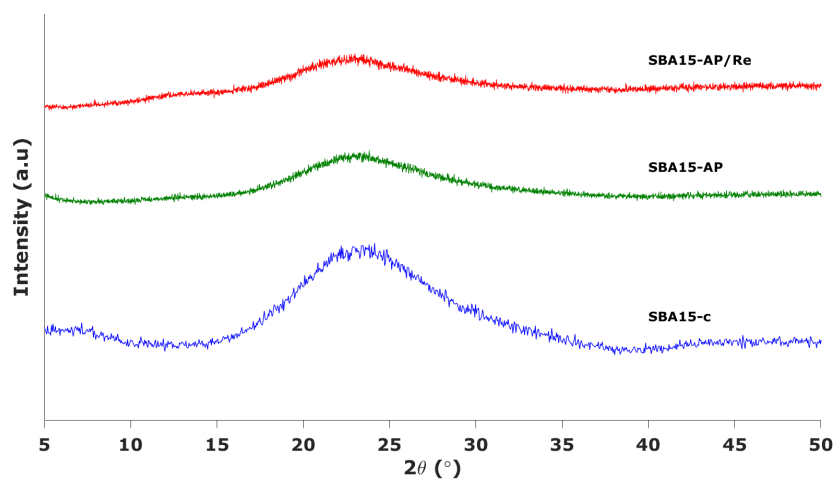
Figure 4.34: Diffractogram pattern of SBA15-AP/Re with calcined (c), aminopropyl modified (AP), and rhenium introduced sample (AP/Re).
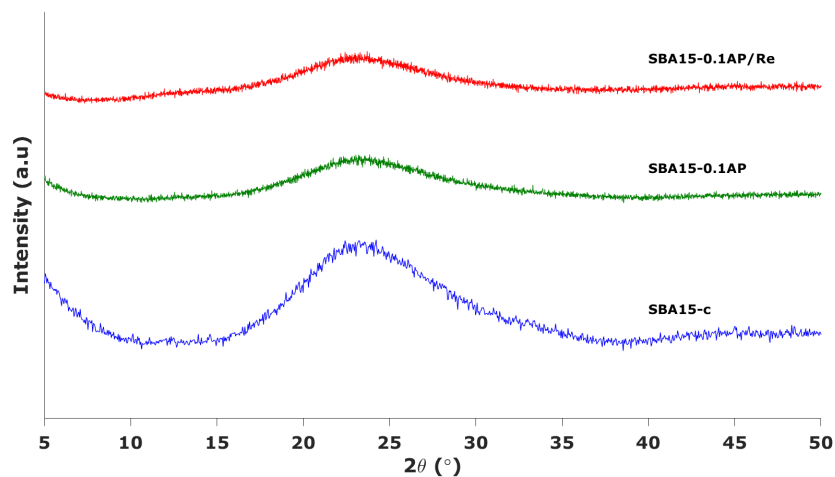
63
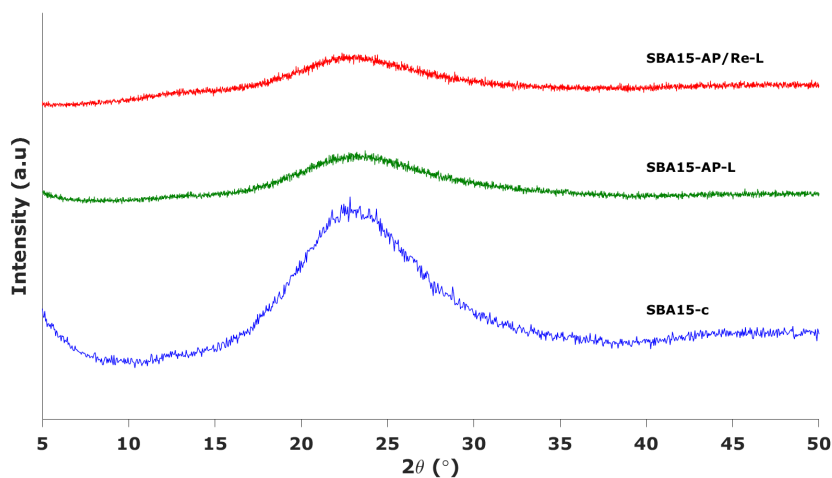
Figure 4.35: Diffractogram pattern of SBA15-AP/Re-L with calcined (c), aminopropyl modified (AP), and rhenium introduced sample (AP/Re).
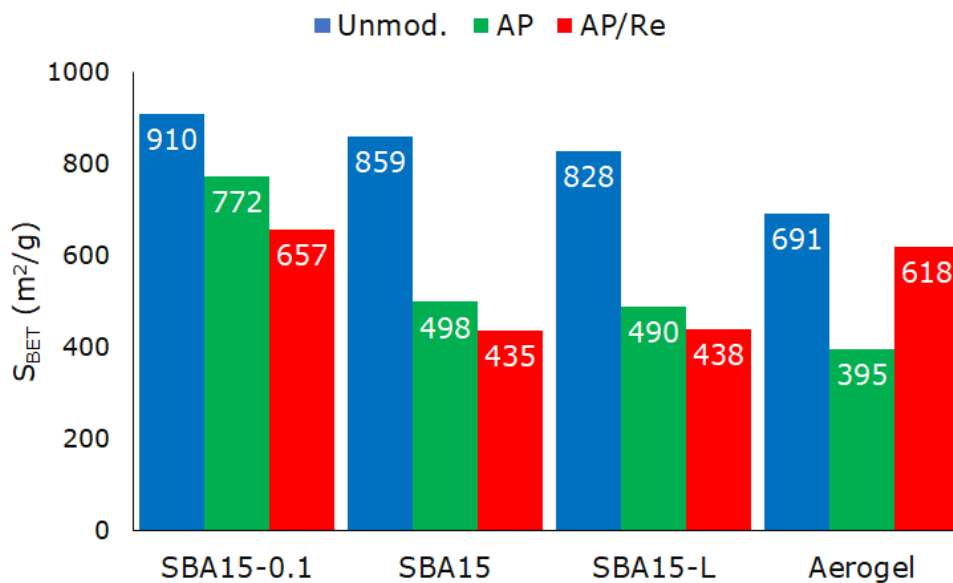
Figure 4.36: N_2 physisorption results for mesoporous samples, comparing the total surface area (S_{BET}) of the unmodified materials, APTES modified, and rhenium introduced materials.
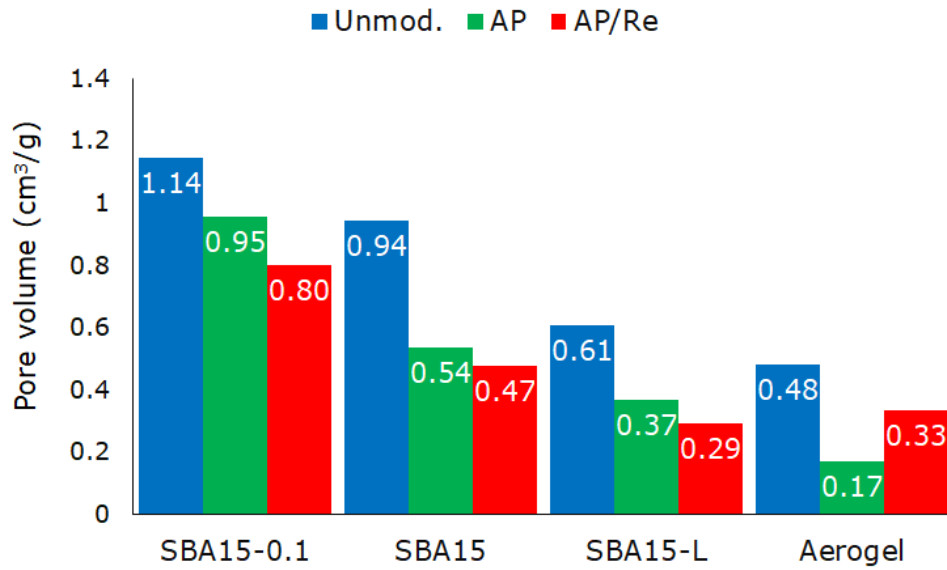
Figure 4.37: N_2 physisorption results for mesoporous samples, comparing the BJH adsorption based pore volume of the unmodified materials, APTES modified, and rhenium introduced materials.
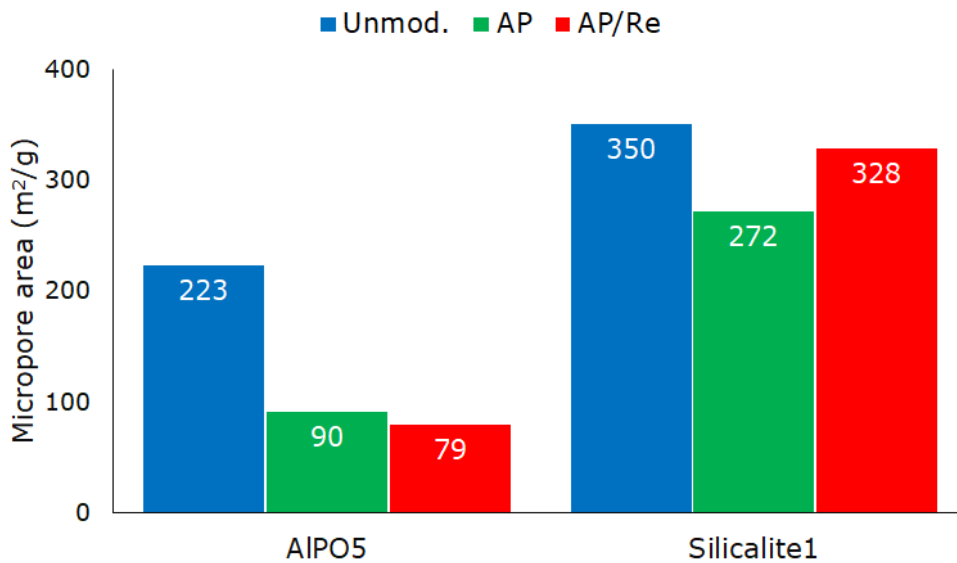
Figure 4.38: N_2 physisorption results for microporous samples, comparing the t-plot based microporous surface area of the unmodified materials, APTES modified, and rhenium introduced materials.
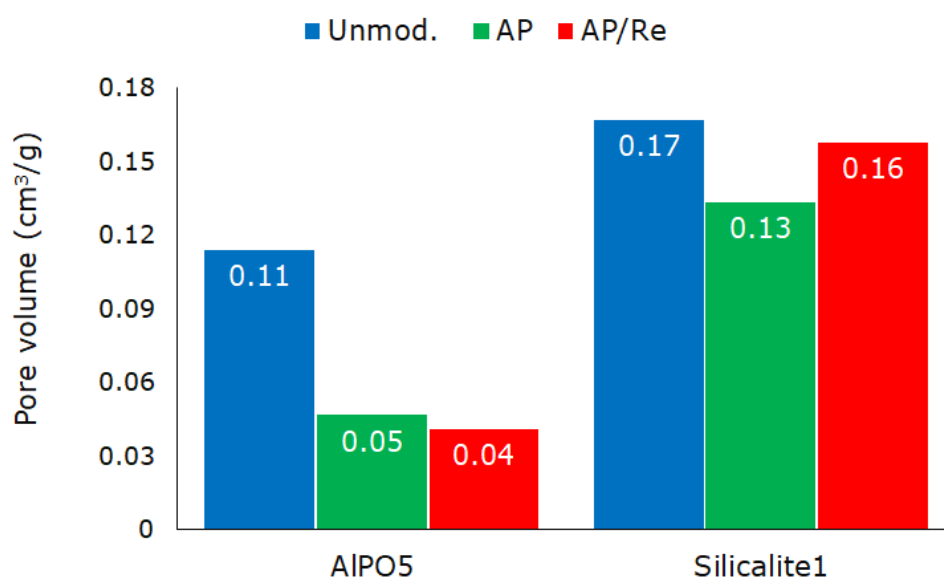
Figure 4.39: N_2 physisorption results for microporous samples, comparing the t-plot based microporous pore volume of the unmodified materials, APTES modified, and rhenium introduced materials.

4.4   XAS

4.4.1   XAS for reference compounds

The normalized and first derivative of the XANES region for the references are shown in Figure 4.40. The determined E_0 values for all references is given in Table 4.9. As illustrated in Figure 4.40 shift in E_0 does not appear correlated to oxidation state of the samples.
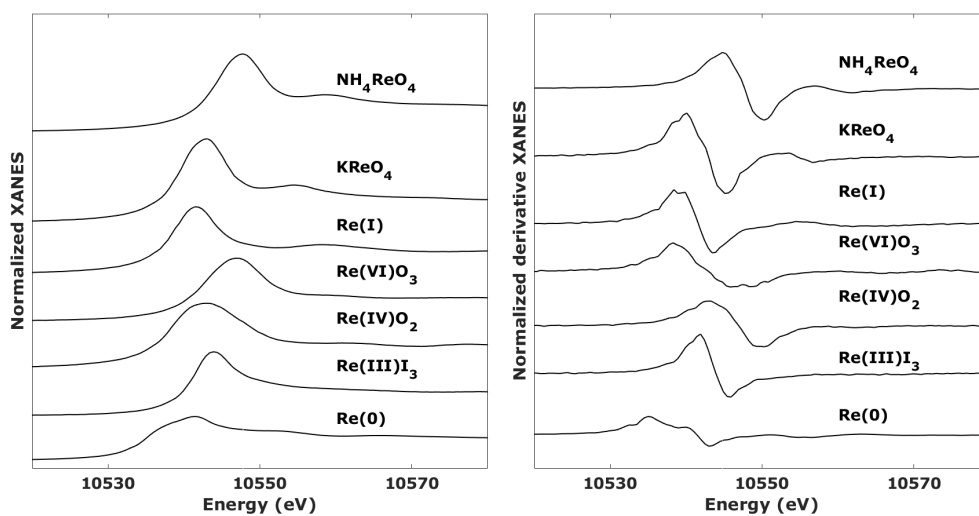
Figure 4.40: The normalized and first derivative XANES region for all rhenium references.

Table 4.9: Oxidation state and determined E_0 for the rhenium samples used as references.

Reference	Oxidation state	E_0 (eV)
Re	0	10535.0
Re(I)	1	10533.9
Re(III)I$_3$	3	10537.5
Re(IV)O$_2$	4	10537.9
Re(VI)O$_3$	6	10533.4
KReO$_4$	7	10534.2
NH$_4$ReO$_4$	7	10538.4

For EXAFS the NH_4ReO_4 samples was used as the reference for all samples, due to the significant contribution of NH_4ReO_4 in all linear combination fittings. The parameters of the references were obtained by keeping the N constant while allowing E_F, R, and the Debye-Waller factor to be refined. After the E_F, R, and Debye-Waller was refined the AFAC was also included in refinement for the first shell. The refinement results of the reference compounds are listed in Table 4.10.
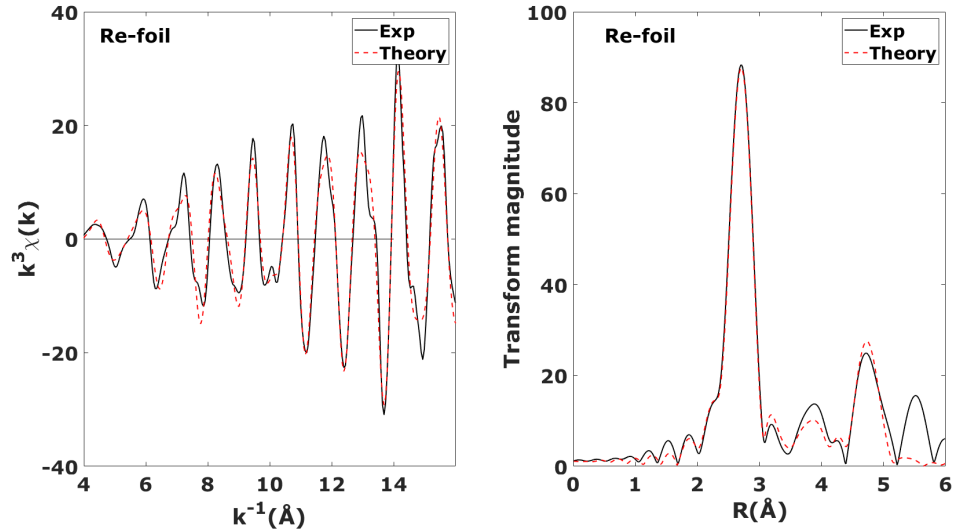
Figure 4.41: Re-foil EXAFS refinement for AFAC, R, E_F and Debye-Waller (σ^2), with N = 12.

Table 4.10: Parameters obtained from EXAFS refinements on Re reference compounds.The identity of 1st scatterer, multiplicity (N), interatomic distance (R), Debye-Waller factor (σ^2), E_0 shift (E_F), k-range, amplitude reduction factor (AFAC), and goodness of fit (R%).

Reference	Scatterer	N	R (Å)	$\Delta\sigma^2$	ΔE_F	Δk	AFAC	R%
Re-foil	Re	12(-)	2.750(3)	0.0079(2)	$-15(1)$	4-16	0.83	23
	Re	6(-)	3.1(2)	0.06(7)				
	Re	2(-)	3.879(9)	0.004(1)				
	Re	18(-)	4.797(7)	0.0096(7)				
NH_4ReO_4	O	4(-)	1.714(6)	0.0016(8)	$-13(1)$	4-10	0.67	24
$KReO_4$	O	4(-)	1.750(6)	0.000 08(166)	$-19(1)$	4-11	0.72	26

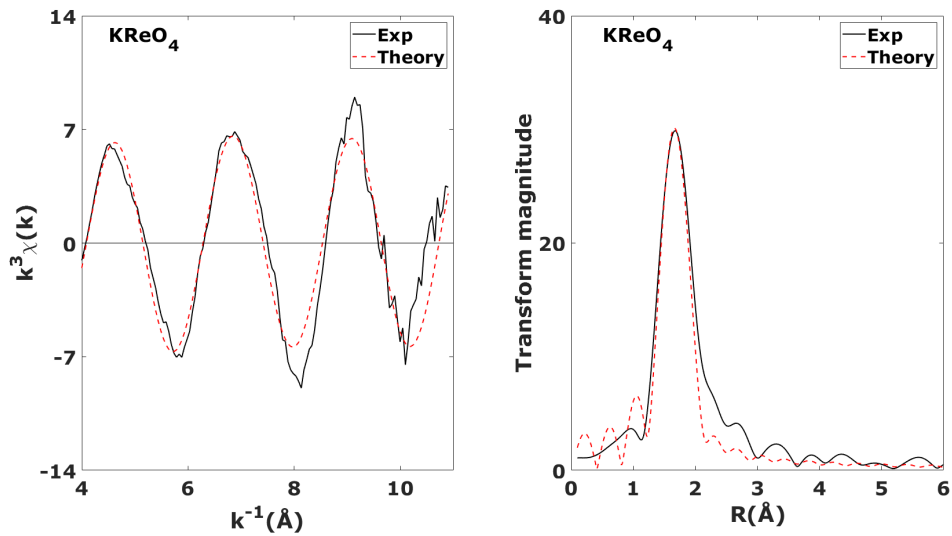**Figure 4.42:** $KReO_4$ EXAFS refinement for AFAC, R, E_F and Debye-Waller (σ^2), with N = 4.
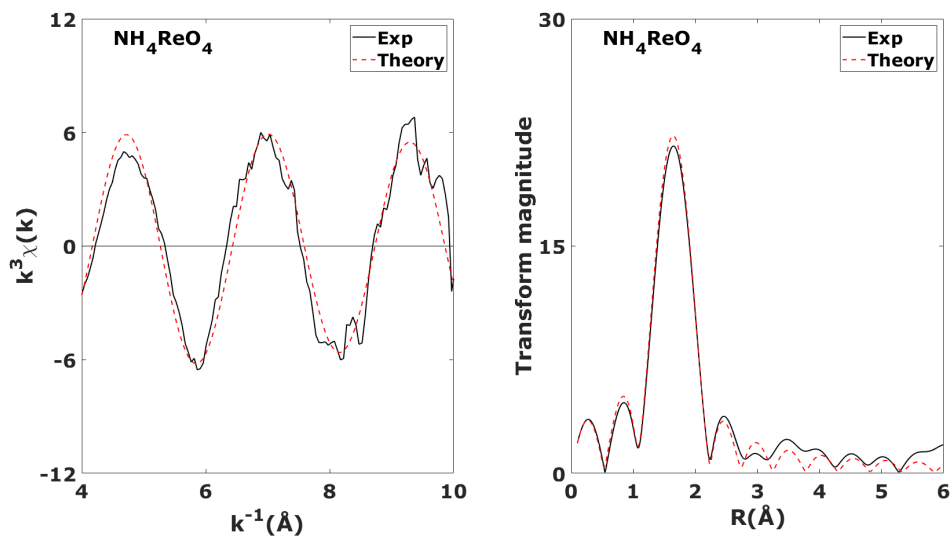

Figure 4.43: NH_4ReO_4 EXAFS refinement for AFAC, R, E_F and Debye-Waller (σ^2), with N = 4.

4.4.2 XANES

In the XANES region of the XAS, the goal was to identify oxidation state and which of our reference materials the samples resembled through spectrum comparison

69

and linear combination fittings (LCF). The initial analysis was comparison of the normalized and normalized first derivative of the XANES region between the references and the samples. This comparison would give a indication of similarity which can be used to evaluate if determined oxidation state and LCF are plausible. Normalized and normalized derivative XANES are shown in Figure 4.40 and Figure 4.44 for the references and samples respectively.
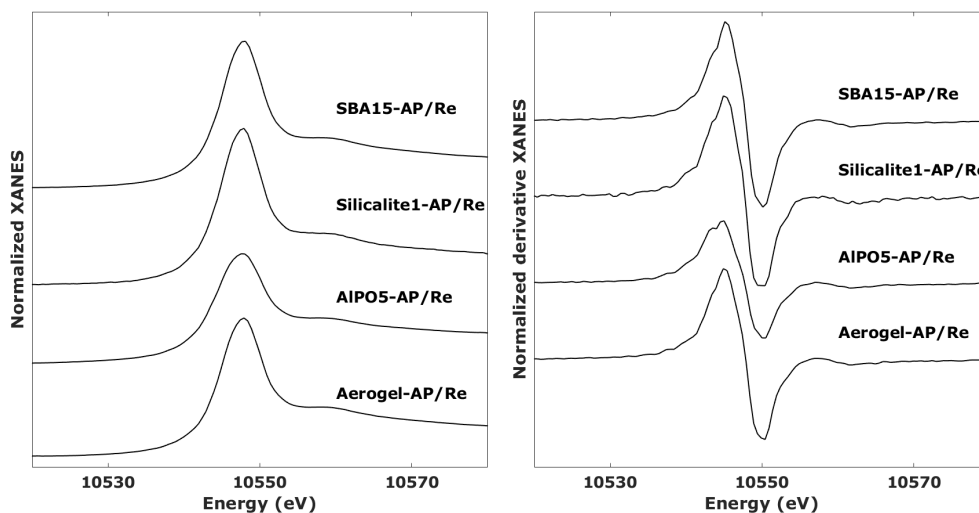
Figure 4.44: The normalized and first derivative XANES region for all rhenium references.

From Figure 4.44 all samples appear similar both for shape of normalized and derivative normalized XANES as well as having a similar whiteline position. Based on whiteline position and the derivative shape the NH_4ReO_4 and $Re(VI)O_3$ references seem to be the closest matches.

Oxidation state determination was attempted using linear regression on the E_0 and oxidation state of the references. Due to their significant deviation from the trend the $Re(VI)O_3$ and $KReO_4$ references was excluded from this linear regression model. Linear regression places all samples around +7, similar to the NH_4ReO_4 reference. Due to the low goodness-of-fit (R^2) and the impact various coordination and ligands have on XANES the determined oxidation states for the samples were rounded to their closest integer value, resulting in +7 for all samples. The illustration of the regression is shown in Figure 4.45, while all data is listed in Table 4.11

Peak fitting was performed on the white line of the samples and references.
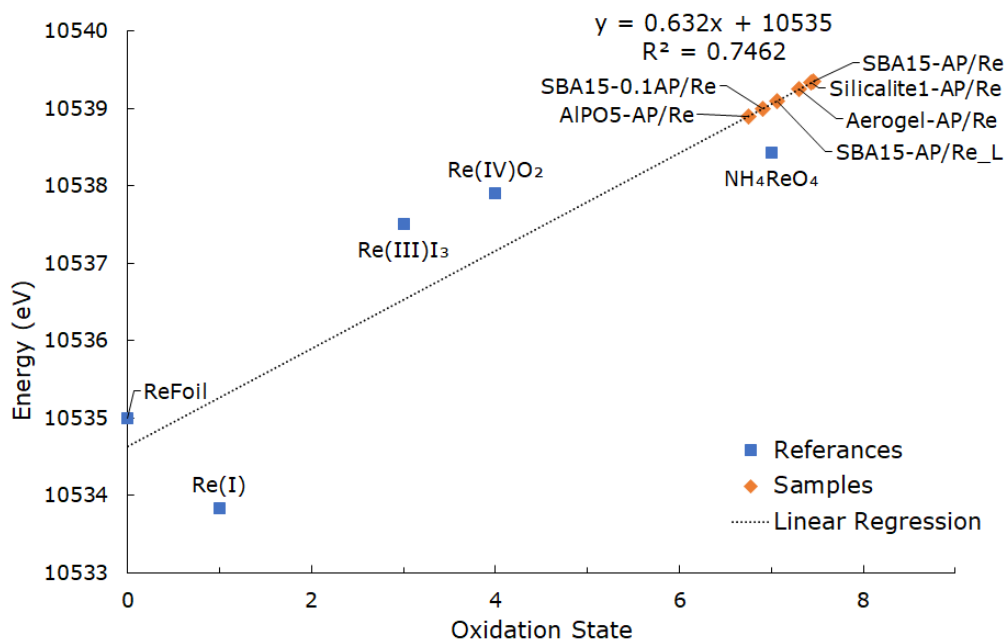
Figure 4.45: Plot of the E_0 for references and samples. A linear regression was applied to the references and oxidation state for the samples was based on the linear regression model of the references.

Oxidation state using peak height was also attempted. An illustration of this whiteline based regression model is shown in Figure 4.46, with the parameters of the peak fittings listen in Table 4.12.

The references peak height had no strong correlation with a R^2 of 0.49 which prevent a clear determination of the oxidation state in the samples. While no clear oxidation state can be elucidated the regression model does indicate the oxidation states. The +6 state would be possible for the ALPO5-AP/Re, however any oxidation state higher then +7 is improbable as the maximum oxidation state for rhenium is +7, therefore these samples are considered at +7. Combining the E_0 and peak height based oxidation state determinations indicate that the samples have a oxidation state of +7.

Linear combination fitting of the samples revealed a difficulty matching any spectrum to one or a combination of reference spectra. A common trend appeared with NH_4ReO_4 composing the majority if the combination fitting with other references having very small or even negative contributions.

Table 4.11: List of the E_0 and oxidation state for all samples. The five upper samples used to make linear regression model applied to the bottom six samples to determine their oxidation state, which is rounded to the closest integer value. The middle two samples deviated significantly from the model and were removed.

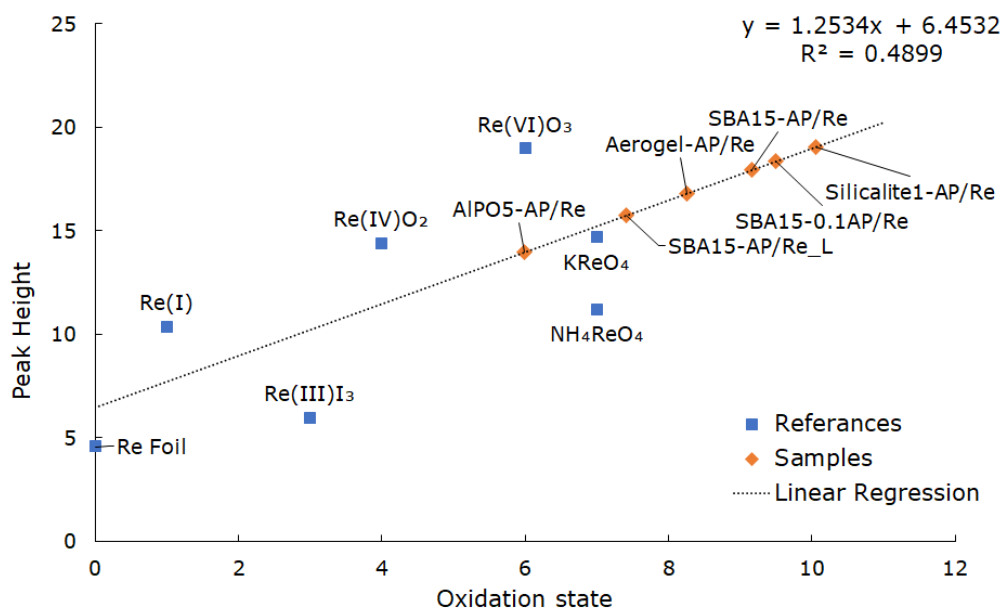| Sample	Oxidation state	E_0
Re foil	0	10535.00
Re(I)	+1	10533.83
Re(III)I_3	+3	10537.50
Re(IV)O_2	+4	10537.90
NH$_4$ReO$_4$	+7	10538.43
Re(VI)O_3	+6	10533.35
KReO$_4$	+7	10534.20
AlPO5-AP/Re	+7	10538.90
Silicalite1-AP/Re	+7	10539.33
Aerogel-AP/Re	+7	10539.25
SBA15-AP/Re	+7	10539.35
SBA15-0.1AP/Re	+7	10539.00
SBA15-AP/Re-L	+7	10539.10

Figure 4.46: Plot of the peak height of both references and samples. Peak height determined by arctan and a Gaussian function, parameters for each peak fitting is listed in Table 4.12.

72

Table 4.12: Peak fitting parameters for the white line of all references and samples. Utilizing arctan and a Gaussian function to calculate fitting. Samples grouped in two areas based on their classification of reference as sample.

Sample	Peak height	Peak center (eV)	Peak area	R-factor
Re-foil	4.6(2)	10541.0	2.9(1)	0.0006391
Re(I)	10.4(2)	10541.5	2.41(2)	0.0001593
Re(III)I$_3$	6.2(2)	10543.8	1.89(4)	0.0001795
Re(IV)O$_2$	14.4(1)	10546.6	3.33(2)	0.0001049
Re(VI)O$_3$	19.0(2)	10542.9	4.12(4)	0.0006621
KReO$_4$	14.7(2)	10542.6	2.58(3)	0.0018591
NH$_4$ReO$_4$	11.2(1)	10547.5	2.56(2)	0.0002806
Aerogel-AP/Re	16.8(2)	10547.7	2.32(2)	0.0002683
Silicalite1-AP/Re	19.1(5)	10540.9	2.30(5)	0.0015639
AlPO5-AP/Re	14.0(2)	10547.5	2.60(2)	0.0001322
SBA15-AP/Re	17.944(7)	10547.7	2.30(7)	0.0000834
SBA15-0.1AP/Re	18.4(2)	10547.6	2.30(2)	0.0002379
SBA15-AP/Re-L	15.7(2)	10547.7	2.35(3)	0.0003264

The LCF of the AlPO5-AP/Re and the SBA15-AP/Re is shown in Figure 4.47 and Figure 4.48 as examples of fits. The AlPO5-AP/Re shows a majority fitting of the NH$_4$ReO$_4$ with a weight of 1.000 and a small contribution from Re(IV)O$_2$ with weight of 0.243 and Re(III)I$_3$ with weight of -0.243. The SBA15-AP/Re shows a similar results as the NH$_4$ReO$_4$ has a weight of 1.000, the minor contribution for the SBA15-AP/Re are from the KReO$_4$ with a weight of 0.141 and the Re(0)-foil with a weight of -0.281. A list of reference weights of all LCF are given in Table 4.13. The LCF for all samples are plotted and can be found in Appendix A.1.

Table 4.13: Overview of the LCF of all samples including three contributing references and the R-factor for each sample. Each contributor also have the weighting for each reference.

| Sample	Contribution 1	Contribution 2	Contribution 3	R-factor
AlPO5-AP/Re	NH$_4$ReO$_4$, 1.000	Re(IV)O$_2$, 0.243	Re(III)I$_3$, -0.243	0.0323607
Silicalite1-AP/Re	NH$_4$ReO$_4$, 1.000	KReO$_4$, 0.164	Re(VI)O$_3$, -0.164	0.1945390
Aerogel-AP/Re	NH$_4$ReO$_4$, 1.000	Re(VI)O$_3$, 0.422	Re(0)−foil, -0.422	0.0909678
SBA15-0.1AP/Re	NH$_4$ReO$_4$, 1.000	KReO$_4$, 0.105	Re(III)I$_3$, -0.105	0.1615925
SBA15-AP/Re	NH$_4$ReO$_4$, 1.000	KReO$_4$, 0.141	Re(0)−foil, -0.281	0.1296650
SBA15-AP/Re-L	NH$_4$ReO$_4$, 1.000	Re(III)I$_3$, 0.412	Re(0)−foil, -0.412	0.0608387
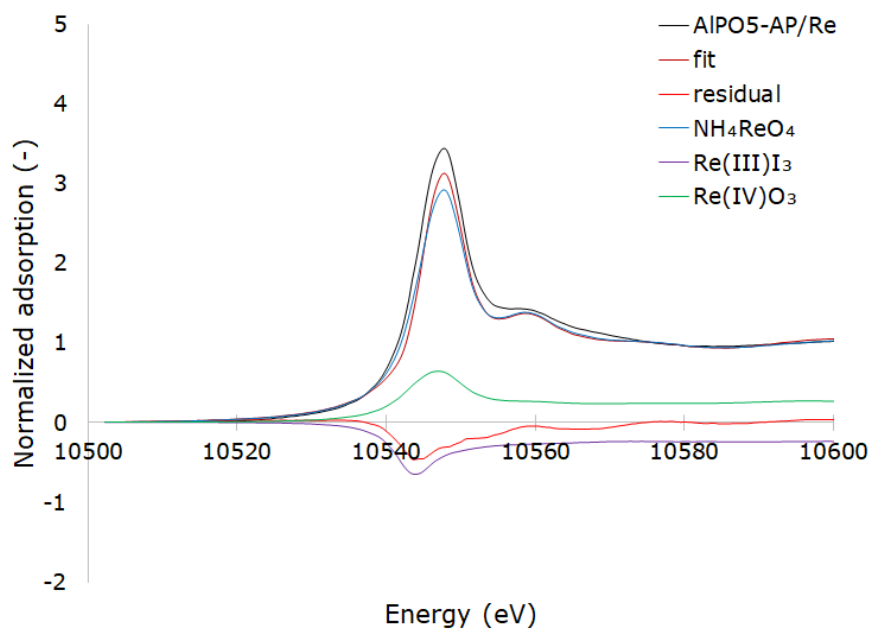
Figure 4.47: Linear combination fitting of a rhenium introduced AlPO5 (AlPO5-AP/Re).
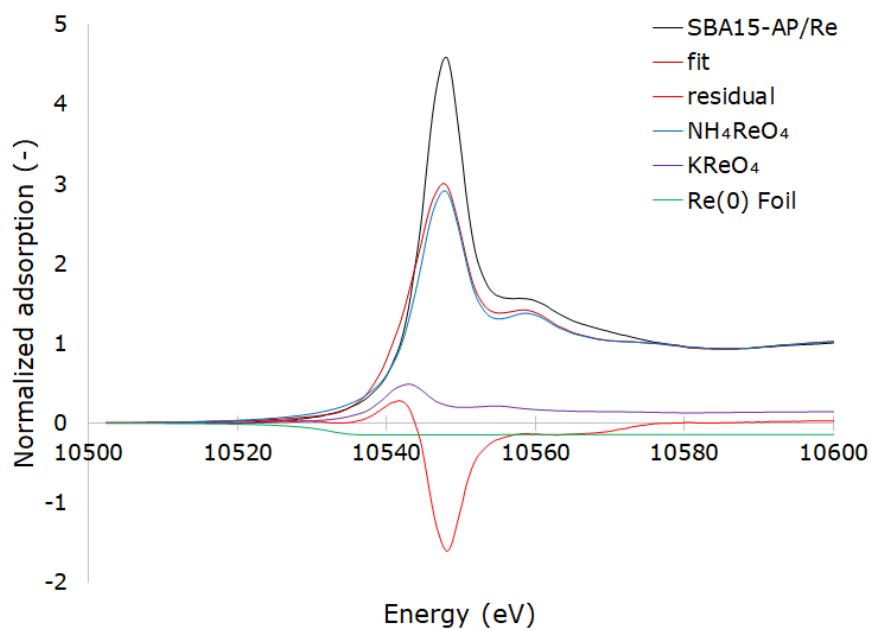

Figure 4.48: Linear combination fitting of a rhenium introduced SBA-15 (SBA15-AP/Re).

4.4.3 EXAFS

A summary of all EXAFS refinement results is given in Table 4.14. The EXAFS refinement for Silicalite1-AP/Re is illustrated in Figure 4.49. This sample was the only sample with unusable data before k-value 4 and usable data after k-value 12, leading to a shifted k-space. The Silicalite1-AP/Re EXAFS had a smooth k-curve, making the fitting of an oxygen shell straightforward. However fitting of the oxygen shell in k^3-space leads to a impossible coordination number of 6.1. Change in the k-weighting did not alleviate this high multiplicity.

Figure 4.49: EXAFS refinement for rhenium introduced Silicalite-1 (Silicalite1-AP/Re), shown in both k-space (k^3-weighting) and R-space.

The AlPO5-AP/Re is illustrated in Figure 4.50. While the signal was worse then that of the Silicalite1-AP/Re, it was decent enough to fit an oxygen shell. The sample appear consistent with the LCF from the XANES indicating a similar environment to NH_4ReO_4. However the fitting in k^3-space lead to a unusable Debye-Waller due to the sine wave not dampening, change to the k^2-space produced a similarly good fit with a reasonable Debye-Waller.

The Aerogel-AP/Re is illustrated in Figure 4.51. The signal was decent and an oxygen shell could be fitted . In k^3-space fitting the oxygen shell produced chemically impossible environments with a negative Debye-Waller and multiplicity of 6.5, while k^2-space managed a decent oxygen shell. The sample remained consistent with the XANES results indicating a similarity with NH_4ReO_4.

Figure 4.50: EXAFS refinement for rhenium introduced AlPO-5 (AlPO5-AP/Re), shown in both k-space (k^2-weighting) and R-space.
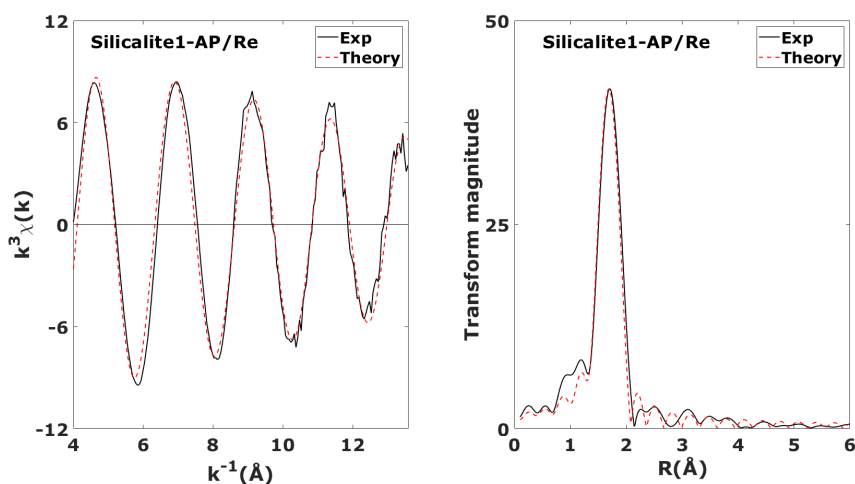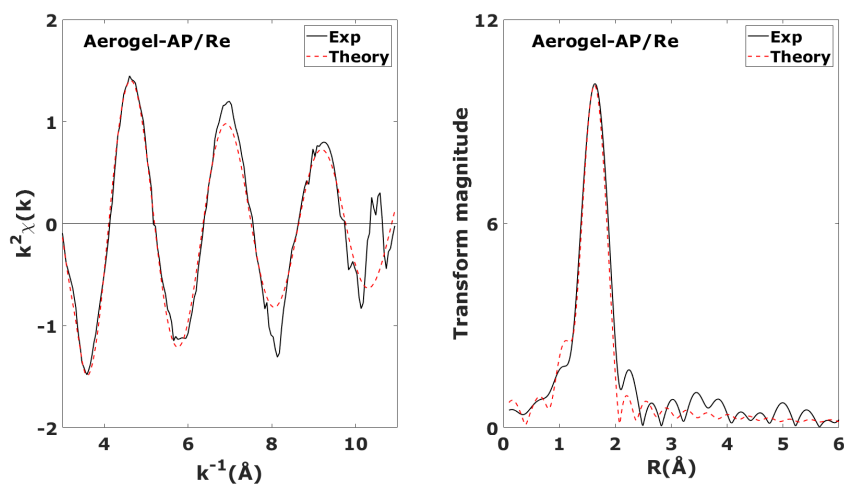

Figure 4.51: EXAFS refinement for rhenium introduced silica aerogel (Aerogel-AP/Re), shown in both k-space (k^2-weighting) and R-space.

The SBA15-AP/Re is illustrated in Figure 4.52. An oxygen shell was successfully fitted. k^2-weighting was attempted to investigate any change to the multiplicity, however change in weighting did not produce any meaningful changes in the EXAFS refinements for this sample. The SBA15-0.1AP/Re is illustrated in Figure 4.53. An oxygen shell was fitted, however this fit was the worst of all the samples. Attempt to refine a reasonable multiplicity for the oxygen shell using k^2-weighting was unsuccessful as no effect was noticed. The sample appear to display a secondary shell,
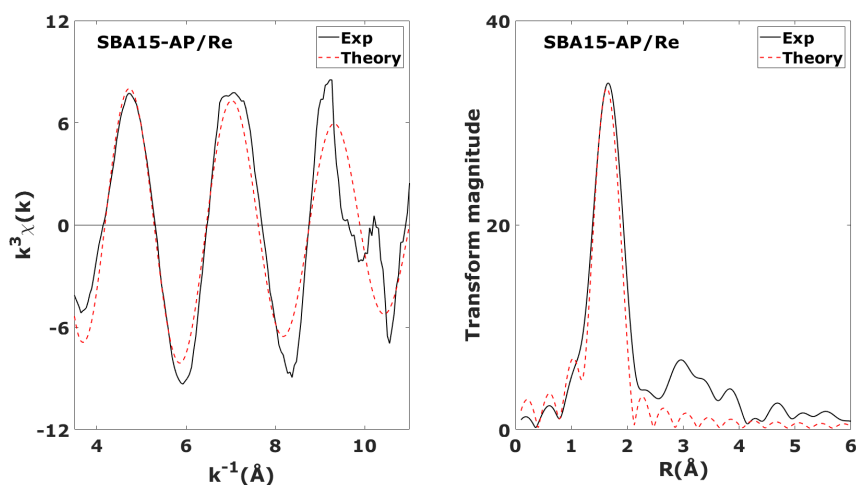
Figure 4.52: EXAFS refinement for rhenium introduced SBA-15 (SBA15-AP/Re), shown in both k-space (k^3-weighting) and R-space.

however attempts to fit this shell via Fourier filtering was ultimately unsuccessful in both k^2 and k^3-weighting. The significant deviations from a sine-wave at higher k^{-1} appear to create the apparent phantom secondary shell. The SBA15-AP/Re-L
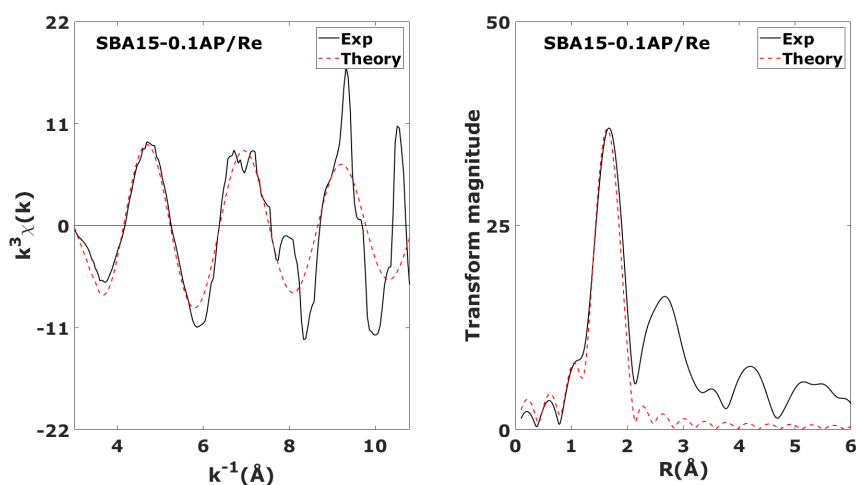
Figure 4.53: EXAFS refinement for rhenium introduced SBA-15 (SBA15-0.1AP/Re), shown in both k-space (k^3-weighting) and R-space.

is illustrated in Figure 4.54. An oxygen shell was fitted, however k^2-weighting was required to achieve a reasonable Debye-Waller factor. The SBA15-AP/Re-L appear as the only SBA15 that benefited from a k^2-weighting compared to k^3-weighting.
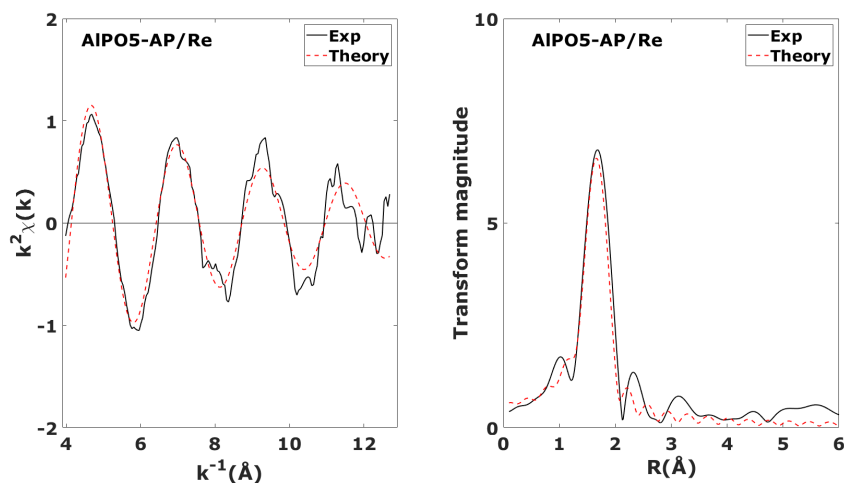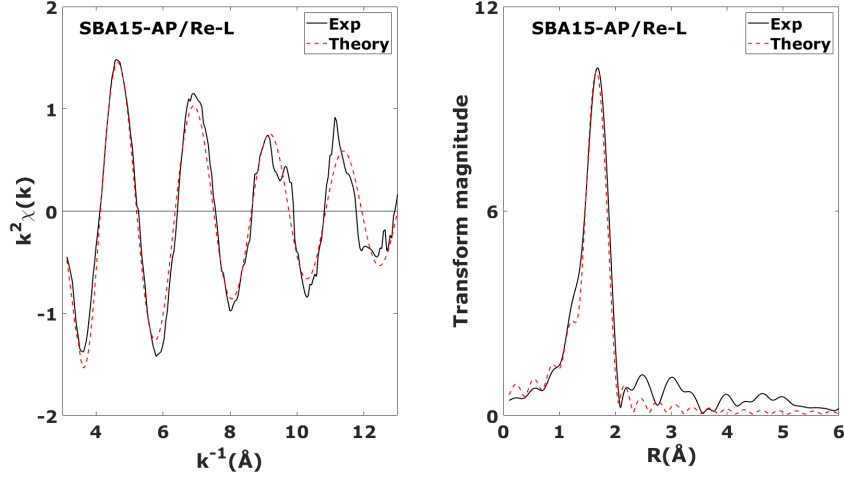
Figure 4.54: EXAFS refinement for rhenium introduced SBA-15 (SBA15-AP/Re-L), shown in both k-space (k^2-weighting) and R-space.

**Table 4.14:** EXAFS refinement derived parameters for rhenium introduced samples. Listed is the identity of scatterer, multiplicity (N), interatomic distance (R), Debye-Waller factor (σ^2), E_0 shift (E_F), k-range, and goodness of fit (R%). All samples refined with a AFAC value of 0.67, derived from the NH_4ReO_4 reference.

Sample	Scatterer	N	R (Å)	$\Delta\sigma^2$	ΔE_F	Δk	R%
Silicalite1-AP/Re	O	6.1(3)	1.731(3)	0.0030(6)	$-16.6(9)$	4-13	17
AlPO5-AP/Re	O	3.7(4)	1.714(7)	0.002(2)	$-11(1)$	4-14	30
Aerogel-AP/Re	O	4.4(3)	1.726(5)	0.0002(15)	$-16.0(7)$	3-11	18
SBA15-AP/Re	O	5.8(7)	1.712(8)	0.005(2)	$-10(2)$	3-11	33
SBA15-0.1AP/Re	O	7(1)	1.73(1)	0.005(4)	$-10(3)$	3-11	45
SBA15-AP/Re-L	O	4.6(2)	1.728(4)	0.0002(9)	$-12.0(7)$	3-12	21

5. Discussion

5.1 Evaluation of the APTES surface modification

All target materials for this thesis was successfully synthesized and APTES modification had a varying impact on their pore networks. For the SBA-15 samples the introduction of the AP groups appear to have lead to a clear decrease in both surface area and pore volumes across all three samples. The decrease in pore area and volume is expected as the addition of surface groups would narrow the pore system. Comparison of the SBA15-0.1AP to the other two SBA-15 samples, SBA15-AP and SBA15-AP-L, indicate a correlation between decreased surface area and pore volume with the amount of APTES in the sample. The silanol amount of all SBA-15 samples should be similar as both synthesis method and calcination procedure was the same, both of which impact textural properties of the SBA-15.[87,88]

The change in surface area and pore diameter for the Aerogel-AP was consistent with the change to the SBA-15 samples, however this decrease can be misleading due to the re-gelation of the gel-network during the APTES modification. The re-gelation of the aerogel and xerogel during suspension in the toluene could have significant impact on pore network due to the subsequent drying, the reduced pressure drying was significantly quicker then the slow heating program which could explain the shrinkage of the aerogel-AP. The Xerogel-AP had a very small increase in surface area of 21 %, as BET measurements have a significant uncertainty it is difficult to ascertain whether the change is due to the measurement uncertainty or an actual increase in micropore surface area due to the small initial micropore surface of $33\,\mathrm{m^2\,g^{-1}}$.

The SBA15-AP and SBA15-AP-L samples had decrease in total surface area of 42 % and 41 percent respectively whereas the decrease for the SBA15-0.1AP,

that was only added 10% of the APTES compared to the others, was 15%. The decrease for the Aerogel-AP was 43 %, which makes the decrease of surface area akin to the two SBA15's decrease. The ordered 1D pore system of the SBA15 compared to the non-ordered 3D pore system in the aerogel does not appear to have any impact on the AP introduction due to their very similar surface area decrease. Interestingly the SBA15-0.1AP only experienced a 15 % decrease, which indicate that the influence of APTES in the pore surface area is not linear with respect to the APTES amount added.

For the AFI zeotypes, the SAPO5-AP and AlPO5-AP, there were a significant difference in the effect of APTES modification on the micropore surface area and micropore volume. After APTES modification the SAPO5-AP did not follow the trend of the SBA-15 with a moderate decrease in surface area, instead the SAPO5-AP had a complete blockage of the micropores. Interestingly the structurally similar AlPO5-AP did not display the same blockage that the SAPO5-AP had. As the difference between these materials is the brønsted acid sites which are only present in the SAPO-5, these brønsted acid sites are considered responsible.

For the AlPO5-AP sample a moderate decrease of the micropore surface area and volume occurred. The decrease was larger then for the SBA15-AP and SBA15-AP-L, but the moderate change indicating that the micropores have sufficient size to not be completely blocked by the APTES reagent. If the pores were too small the system would become obstructed, as with the SAPO5-AP, or there would only be a small change.

The APTES modification on silicalite1-AP had significantly less impact on the micropore surface area and pore volume compared to the other samples. A possible reason is the smaller pore size of around 0.55 nm for the silicalite-1 compared to the larger pores of 0.73 nm in the AFI framework. As the free APTES molecule has a diameter of 0.5 nm it would be very challenging for the APTES to reach the inside of the porous network, this subsequently leads to a insignificant change in the surface area and very few APTES molecules would have entered the pore network.[56]

In general the mesoporous materials appears more suited for the APTES modification, explained by the large pore diameter not being a size limitation on the APTES reagent. From the three SBA-15 samples we do see a correlation between decrease in surface area and APTES amount, however the correlation does not appear to be linear with amount of APTES added. This correlation could be used to tailor the amount of available AP sites on modified materials, however the exact correlation for various pore sizes and materials would need to be investigated further. The aerogel and xerogel having a re-gelation in the organic solvent does

remove any advantage of post-synthetic modification for these materials as the subsequent re-drying process could significantly alter the pore network.

Microporous materials with pore size below 0.7 nm appear unsuited for APTES modification, due to the size of the APTES molecule, above the 0.7 nm there does not appear to be significant issues with the size of the APTES. The surface chemical species also appear important, reactive sites like the brønsted acid sites can prove detrimental. The brønsted acid sites appear to have increased reactivity thus creating a physical APTES plug in the entrance to the pores.

The surface area also changed after the rhenium introduction. This could be either attributed to the introduction process or the rhenium added. The SBA-15 samples and the AlPO-5 all have similar slight decreases for surface area and pore volumes, this could be due to the inherent inaccuracy of the BET method or due to the introduced rhenium. The aerogel the significant increase in surface area and pore volume would be explained by the re-gelation of the material, as the drying gelation and subsequent drying could lead to generation of new mesoporous voids. The silicalite-1 also experiences and increase in surface area and volume which could be explained by the hypothesis of too small pores. If the pore are too small for the APTES widest area, the head group, then some molecules could become stuck in the pore system not free enough to react and not free to leave. The re-dispersion and change of solvent to acetonitrile could have dislodged these molecules, freeing up a small amount of pores previously blocked.

5.2 Rhenium loading

The introduction of rhenium was a exceptional success for the mesoporous materials with varying results for the microporous samples. Even with the high loading of rhenium there does not appear to be consistent amount of rhenium in the samples. The SBA15-AP/Re and SBA15-AP/Re-L should have similar AP amounts based on APTES additions, however there is a significant difference in the rhenium loading for these two samples. The SBA15-0.1AP/Re should have significantly less AP sites compared to the SBA15-AP/Re-L which could be explained by inhomogeneity for rhenium or AP sites in our three SBA-15 samples. Nevertheless comparing the APTES modification and rhenium loading the mesopores of the SBA-15 system appear well suited for this method of anchoring rhenium.

Other than the SBA-15 samples the Aerogel-AP/Re and Xerogel-AP/Re had exceptional rhenium retention of 6.5 wt.% and 8.8 wt.% respectively. Due to the

re-gelation occurring for both the Aerogel and Xerogel samples during the APTES modification and the rhenium introduction the usual pore size categories can not be reasonably applied to these samples. The Xerogel outperforming the Aerogel could be explained by the synthesis procedure of the Aerogel, the added silylation agents which allows for the APD drying method might deny suitable silanol reaction sites for the APTES leading to fewer AP anchors in the Aerogel compared to the Xerogel. Therefore the APD produced Aerogel appear more unsuited for this method of anchoring rhenium, using SCD would remove this issue but be more costly and harder to scale. The difference between Aerogel and Xerogel in the modification and rhenium introduction appear to be more related to the impact silylation agents added during material synthesis have on this APTES modification rather then related to micro- and mesoporosity in the materials.

The entirely microporous materials had significantly lower adsorption of rhenium compared to their mesoporous counterparts. The AlPO-5 achieved a 2.8 wt.% loading, while the structurally similar SAPO-5 only achieved 0.9 wt.%. The difference between these materials after the AP surface modification is the available surface area. During the surface modification the AlPO-5 maintained it's porous network, if the APTES managed to react inside the pore system then the higher loading in AlPO-5 would be explained by the additional adsorption sites on the inside of the pore system. The SAPO-5 had completely blocked pores which is a possible explanation for the lower rhenium retention, without adsorption sites inside the pore system the rhenium has significantly fewer anchor sites to coordinate to.

The Silicalite-1 achieved the lowest loading of all tested materials with a 0.8 wt.% loading, one possible reason for the low loading might be few AP sites inside the material. Silicalite-1 has pores around 0.55 nm, which are the smallest pores tested here. If very little or nothing of the pore network is utilized for adsorption of Rhenium due to APTES not being able to reach the inside of the pores, then the low loading might be a result of few available sites. The loading amount is also comparable to SAPO-5, which gained inaccessible pores after the surface modification limiting adsorption to external adsorption sites. If both the SAPO-5 and Silicalite-1 only achieved AP groups on the external surface area with little or no AP inside the pore network then the low loading could be explained by few AP groups.

The very high retention of rhenium for the mesoporous materials combined with their apparently easy reaction with the organosilane mean that these methods can be used to select desired rhenium loading in a material, after a few initial test. As most of the added rhenium is adsorbed these mesoporous materials would require little work to target specific amounts. However the microporous materials are

overall less suited. The rhenium retention is significantly lower for the microporous materials and the small pore size is limiting for the APTES modification step.

5.3   Assessment of introduced rhenium

While the used rhenium source was the Re_2O_7 the resulting form of rhenium in the samples is less clear. From the XRD the support materials were preserved and no clear reflections of rhenium was detected. However any rhenium nanoparticles would not necessarily be noticeable in the diffractograms as the small particle size would lead to low intensity wide reflections, which would be difficult to distinguish from background noise. Formation of very small rhenium nanoparticles can therefore not be dismissed as a possibility.

The XANES region in the samples showed most similarity with the NH_4ReO_4 reference, which was not unexpected due to Re_2O_7 forming ReO_4^- in solutions and the coordination with the AP groups would make a comparable environment to the NH_4ReO_4. LCF of the samples revealed that all samples were reminiscent of NH_4ReO_4, however as they could not be described with only this one reference they appear to be chemically distinct from the NH_4ReO_4.

Determination of oxidation state was successful even though the goodness-of-fit for both methods employed was low. Both the E_0 based method and the peak fitting of whiteline method indicated an oxidation state around +7 for all samples, keeping the samples consistent with the XANES comparison and LCF which indicated similarity with the NH_4ReO_4 reference. The determination of oxidation state proved challenging for the samples due to the non-linearity of oxidation state when compared to the E_0 and whiteline for these rhenium compounds. While the Re L_{III}-edge has a lesser pronounced shift in energy compared to the K-edge or the L_I-edge a stronger correlation should have been possible to establish.[70] The lack of linearity could arise from multiple sources. The amount of noise for all samples indicate a systemic issue in the measurement setup, however this effect should shift all results equally instead of scattering the results.

The EXAFS analysis revealed some differences between the various samples. The refinement proved challenging with the Debye-Waller factor for multiple samples being significantly lower then anticipated from other EXAFS refinements for rhenium.[12,89] If a sample has an error with the Debye-Waller factor the multiplicity

calculation would also be deceiving, as the Debye-Waller and multiplicity is correlated the fitted curve would compensate for lowered Debye-Waller by increasing the multiplicity to achieve a good fit. Some samples got better results by switching to the k^2-weighting from the standard k^3-weighting. Using k^2 does mean that lighter backscatteres like oxygen contribute more and might eclipse smaller rhenium contributions, however as only oxygen shells are fitted and no intentional reduction of samples were performed usage of the k^2-weighting should not be an issue.

The Silicalite1-AP/Re shows a solid fit with an oxygen shell at $1.73\,\text{Å}$, which is a bit shorter then the theoretical bond length of NH_4ReO_4 toward the bond length of $1.714\,\text{Å}$ of the refined NH_4ReO_4. While the bond distance matches the oxygen shell equal to NH_4ReO_4 the coordination of 6.1 is not consistent with the 4 coordination of NH_4ReO_4, instead this multiplicity is indicating of a ReO_3 similarity. However the oxidation state, LCF, and bond lengths all serve as signs that the multiplicity is misleading, possibly related to the issues with low Debye-Waller for all samples during the refinement.

The AlPO5-AP/Re had a OK fit with an oxygen shell at $1.714\,\text{Å}$, which is identical to the refined bond length of the NH_4ReO_4 reference. The multiplicity of the AlPO5-AP/Re at 3.7 is slightly below the expected value of 4 but within range considering the uncertainty. The Aerogel-AP/Re had similar results to the AlPO5-AP/Re with a good multiplicity for an perrhenate oxygen shell and a distance in between the refined NH_4ReO_4 of $1.714\,\text{Å}$ and the theoretical NH_4ReO_4 of $1.74\,\text{Å}$.

The three SBA-15 samples showed varying issues during the EXAFS refinement procedure. All SBA-15's appear similar to other samples fitting an oxygen shell at around $1.7\,\text{Å}$, however the multiplicity for these samples vary significantly. The SBA15-AP/Re-L appear most consistent with the XANES results and the EXAFS results of other samples with a multiplicity slightly above 4, this sample also benefited from k^2-weighting as observed for the Aerogel-AP/Re and AlPO5-AP/Re. The SBA15-AP/Re had similar refinement as the Silicalite1-AP/Re with bond length consistent with perrhenate but a significantly higher multiplicity. Considering the oxidation state, LCF, and XANES similarity the SBA15-AP/Re multiplicity was considered misleading as was done with the Silicalite1-AP/Re sample.

The SBA15-0.1AP/Re had some unique refinement results, it possessed the highest refined multiplicity with an significant uncertainty this multiplicity. A apparent secondary shell was also present, but no good fits could be found during Fourier filtering of this secondary shell. Both the high multiplicity and lack of good fits for the secondary shells was present for both k^3-weighting and k^2-weighting. A possible

explanation of the phantom shell is that the significant deviations from a dampened sine wave in the k-space at higher k-values hides an actual secondary shell from being identified. The higher k-values is where heavier atoms would appear in the signal, therefore this secondary shell might be a combination of a minor secondary rhenium shell and the significant noise but without a way to remove this noise no conclusion regarding a secondary shell can be made.

All the samples appear consistent with the XANES result indicating a NH_4ReO_4 similarity, with the notable exception of the multiplicity for several samples. There does not appear to be any significant elongated Re-O shell that would indicate a bonding to the support materials oxygen for any of the tested materials.[12] The rhenium speciation appear to be independent of both the structure of the support material and the assumed location of the rhenium in the pores. Comparing a SBA-15 to a AlPO-5 there are significant changes in the properties of the support, however there does not appear to be any change in the rhenium speciation for these samples. Similar to the insensitivity to the material, the rhenium location appear irrelevant. Based on APTES modification the silicalite-1 would have significant rhenium loading on external surface area but the rhenium speciation appear consistent with samples like the SBA-15 or the AlPO-5 where the rhenium is assumed to inhabit the internal surface area of the pores.

6. Conclusion

The aim of this thesis was synthesis, post-synthetic modification, and then a subsequent introduction of rhenium to a variety of porous support materials, overall the goal of the thesis was achieved with several materials achieving significant amounts of rhenium.

The method to introduce rhenium in this work can be tailored to specific rhenium loading, depending on the material selection. The SAPO-5, Silicalite-1, and to a lesser degree the AlPO-5 proved less suited for APTES modification which significantly reduced the rhenium adsorption for these samples. The mesoporous SBA-15 and the Silica Aerogel and Xerogel was highly suited for the APTES modification and managed to adsorb up to 9.4 wt.% rhenium, exceeding expectations significantly. The Aerogel and Xerogel is however less versatile due to re-gelation during modification that alters the pore network after synthesis. The SBA-15 appear most suited out of all the material for the purposes of introducing rhenium without significant impairment of its pore system.

The method proved relatively benign to the chosen support material as the post-synthetic modification with APTES and the subsequent rhenium introduction did not alter any crystalline or amorphous phase in PXRD. The only impact appear to be on the internal and external surface areas of the material, where mesopores are favored over micropores. The speciation of rhenium was determined as independent of the properties of the chosen support materials as well as the location of the rhenium on the interior or exterior of the pore network, for all samples the rhenium retained was Re(VII) with an oxygen shell similar to that of the NH_4ReO_4

The high rhenium loading of materials in this work should therefore be transferable to other support materials if desired. Provided the support possess a sufficiently large pore size, preferably larger then 0.7 nm in diameter, APTES modification should be possible and not affect anything other the surface area and volume of the pores. The rhenium speciation would not be affected by choice of support material,

allowing significant freedom in choosing the most appropriate support. However some considering regarding surface groups in the support must be made, where groups like the brønsted acid sites are unfavorable.

7. Future work

It would be highly beneficial to determine catalytic properties of rhenium in the materials synthesized. The employed method of introducing rhenium appear might hinder the catalytic properties by shielding the rhenium from reactants or prevent key steps in catalytic mechanisms. If the method hinders catalytic properties these materials would only be useful to extract rhenium from solutions.

The method used in this work could be expanded to other common catalyst supports, e.g., alumina and zirconia. Getting more indication of suitable support materials would determine whether this modification is limited to the specific materials used in this work or viable for other systems. A APTES modification of other SAPO-class materials should also be investigated with focus on the mechanism behind pore system blockage. To confirm if the p-ethyltoluene causes the blockage of the SAPO-5 pore system a different solvent than toluene should be used.

The APTES and subsequent rhenium introduction could be used to introduce highly dispersed rhenium. Using the APTES as anchors throughout the material the rhenium should be highly dispersed, if the material it then subjected to calcination the APTES would be removed potentially while leaving the rhenium spread throughout the material. Using this method organosilane modification might be a valuable method of increasing dispersion of active materiel in catalysts with high affinity towards the various functional groups found in organosilanes.

References

[1] Noddack, W. V.; Tacke, I. *Die Naturwissenschaften* **1925**, *13*, 567–574.

[2] Davenport, W. H.; Kollonitsch, V.; Kline, C. H. *Industrial and Engineering Chemistry* **1968**, *60*, 10–19.

[3] Guczi, L. *et al. Catalysis Today* **2002**, *77*, 237–243.

[4] Ryashentseva, M. A. *Uspekhi Khimii* **1998**, *67*, 193–196.

[5] Cheremisinoff, N. P. *et al. Handbook of Pollution Prevention and Cleaner Production - Best Practices in The Petroleum Industry*; 2009; pp 1–97.

[6] Mol, J. C. *Catalysis Today* **1999**, *51*, 289–299.

[7] Yuan, Y.; Shido, T.; Iwasawa, Y. *Chemical Communications* **2000**, 1421–1422.

[8] Kusakari, T.; Sasaki, T.; Iwasawa, Y. *Chem Commun* **2004**, *6*, 992–993.

[9] Hayashi, F.; Iwamoto, M. *Microporous and Mesoporous Materials* **2011**, *146*, 184–189.

[10] Greenwood, N. N.; Earnshaw, A. *Chemistry of the Elements*, 2nd ed.; Elsevier, 1997; pp 1040–1069.

[11] Kojima, R. *et al. Applied Catalysis A: General* **2003**, *246*, 311–322.

[12] Rønning, M.; Nicholson, D. G.; Holmen, A. *Catalysis Letters* **2001**, *72*, 141–146.

[13] Mishra, G. S.; Machado, K.; Kumar, A. *Journal of Industrial and Engineering Chemistry* **2014**, *20*, 2228–2235.

[14] Tafjord, J. *Introduction of rhenium into porous supports*; 2017; p 98.

[15] Shahbazi, A.; Younesi, H.; Badiei, A. *Chemical Engineering Journal* **2011**, *168*, 505–518.

[16] Malhis, A. A. *et al. Adsorption Science and Technology* **2018**, *36*, 270–286.

[17] Zhang, G. *et al. Journal of CO2 Utilization* **2018**, *24*, 22–33.

[18] Mishra, G. *et al. Catalysts* **2018**, *8*, 114.

[19] Rouschias, G. *Chemical Reviews* **1974**, *74*, 531–566.

[20] Sims, C. A History of Superalloy Metallurgy for Superalloy Metallurgists. 2012.

[21] Wahl, J.; Harris, K. *MATEC Web of Conferences* **2014**, *14*, 4–9.

[22] Giamei, A. F.; Anton, D. L. *Metallurgical Transactions A* **1985**, *16*, 1997–2005.

[23] Huang, M.; Zhu, J. *Rare Metals* **2016**, *35*, 127–139.

[24] Argyle, M. D.; Bartholomew, C. H. *Catalysts* **2015**, *5*, 145–269.

[25] Liu, L.; Corma, A. *Chemical Reviews* **2018**, *118*, 4981–5079.

[26] Murata, K. *et al. Angewandte Chemie - International Edition* **2017**, *56*, 15993–15997.

[27] Yang, Y. *et al. Applied Catalysis B: Environmental* **2014**, *145*, 91–100.

[28] Chorkendorff, I.; Niemantsverdriet, H. *Concepts of Modern Catalysis and Kinetics*, 3rd ed.; WILEY-VCH Verlag: Weinheim, 2017; p 505.

[29] Rouquerol, J. *et al. Pure and Applied Chemistry* **1994**, *66*, 1739–1758.

[30] Corma, A.; Martinez, A. *Advanced Materials* **1995**, *7*, 137–144.

[31] Boscoboinik, J. A. *et al. Microporous and Mesoporous Materials* **2013**, *165*, 158–162.

[32] Qinhua, X.; Aizhen, Y. *Progress in Crystal Growth and Characterization of Materials* **1991**, *21*, 29–70.

[33] Baerlocher, C.; McCusker, L. B.; Olson, D. H. *Atlas of Zeolite Framework Types*; 2008; pp 94–95.

[34] McCusker, L. B.; Liebau, F.; Englehardt, G. *Microporous and Mesoporous Materials* **2003**, *58*, 3–13.

[35] Flanigen, E. M.; Patton, R. L.; Wilson, S. T. *Studies in Surface Science and Catalysis*; 1988; Vol. 37; pp 13–27.

[36] Blackwell, C. S.; Patton, R. L. *Journal of Physical Chemistry* **1988**, *92*, 3965–3970.

[37] Flanigen, E. M. *et al. Nature* **1978**, *271*, 512–516.

[38] Zhao, D. *et al. Science* **1998**, *279*, 548–552.

[39] Zhao, D. *et al. Chemistry of Materials* **2000**, *12*, 275–279.

[40] Linton, P.; Alfredsson, V. *Chemistry of Materials* **2008**, *20*, 2878–2880.

[41] Zhao, D. *et al. Journal of Physical Chemistry B* **2005**, *109*, 8723–8732.

[42] Pinto, V. H. A. *et al. Applied Catalysis A: General* **2016**, *526*, 9–20.

[43] Ahmed, K. *et al. Microporous and Mesoporous Materials* **2016**, *236*, 167–175.

[44] Aerogel. 2008; `http://goldbook.iupac.org/A00173.html`.

[45] Xerogel. 2008; `http://goldbook.iupac.org/X06700.html`.

[46] Kistler, S. S. *Nature* **1931**, *127*, 741–741.

[47] Gurav, J. L. *et al. Journal of Nanomaterials* **2010**, *2010*.

[48] Feldman, M.; Desrochers, P. *Industry and Innovation* **2003**, *10*, 5–24.

[49] Pellett, J. D. *et al. Accelerated Predictive Stability* **2018**, 383–401.

[50] Miller, J. M. *Chromatography: Concepts & contrasts*, 2nd ed.; WILEY-VCH Verlag: Hoboken, New Jersey, 2009.

[51] Soleimani Dorcheh, A.; Abbasi, M. H. *Journal of Materials Processing Technology* **2008**, *199*, 10–26.

[52] Scherer, G. *Encyclopedia of Materials: Science and Technology*; Elsevier, 2001; pp 9797–9799.

[53] Prakash, S. S. *et al. Nature* **1995**, *374*, 439–443.

[54] Alothman, Z. A. *Materials* **2012**, *5*, 2874–2902.

[55] Brinker, C. J.; Scherer, G. W. *Journal of Non-Crystalline Solids* **1985**, *70*, 301–322.

[56] Munguía-Cortés, L. *et al. Chem. Soc* **2017**, *2017*, 273–281.

[57] Ahmed, M.; Sakthivel, A. *Journal of Porous Materials* **2018**, *0*, 0.

[58] Bragg, W. H.; Bragg, W. L. *Proceedings of the Royal Society* **1913**, *88*.

[59] Atkins, P.; Paula, J. d. *Atkins' Physical Chemistry*, 10th ed.; Oxford University Press: Oxford, United Kingdom, 2014.

[60] International Center for Diffraction Data. `http://www.icdd.com`.

[61] Crystallography Open Database. `http://www.crystallography.net`.

[62] Brunauer, S.; Emmett, P. H.; Teller, E. *Journal of the American Chemical Society* **1938**, *60*, 309–319.

[63] Sing, K. S. W. *Pure and Applied Chemistry* **1982**, *54*, 2201–2218.

[64] Thommes, M. *et al. Pure and Applied Chemistry* **2015**, *87*.

[65] Weller, M. *et al. Inorganic Chemistry*, 6th ed.; Oxford University Press: Oxford, United Kingdom, 2014.

[66] Newville, M. *Reviews in Mineralogy and Geochemistry* **2014**, *78*, 33–74.

[67] Koningsberger, D. C. *et al. Topics in Catalysis* **2000**, *10*, 143–155.

[68] Hubbell, J. H.; Seltzer, S. M. X-Ray Mass Attenuation Coefficients. 2019; `https://www.nist.gov/pml/x-ray-mass-attenuation-coefficients`.

[69] Haynes, W. M. *CRC Handbook of Chemistry and Physics*, 97th ed.; CRC Press: Boca Raton, FL 33487-2742, 2016.

[70] Tougerti, A. *et al. Physical Review B - Condensed Matter and Materials Physics* **2012**, *85*, 1–8.

[71] Ebashi, T. *et al. Journal of Physical Chemistry C* **2010**, *114*, 6518–6526.

[72] Calvin, S. *XAFS for Everyone*; CRC Press: Boca Raton, FL 33487-2742, 2013.

[73] Stern, E. A. *Journal of Synchrotron Radiation* **2001**, *8*, 49–54.

[74] Sayers, D. E.; Stern, E. A.; Lytle, F. W. *Physical Review Letters* **1971**, *27*, 1204–1207.

[75] Bordiga, S. *et al. Chemical Reviews* **2013**, *113*, 1736–1850.

[76] Cao, G.; Wang, Y. *Nanostructures and Nanomaterials*; World Scientific Series in Nanoscience and Nanotechnology; WORLD SCIENTIFIC, 2011; Vol. 2.

[77] Guth, J. L.; Kessler, H.; Wey, R. *Studies in Surface Science and catalysis* **1986**, *28*, 121–128.

[78] Bhagat, S. D. *et al. Solid State Sciences* **2007**, *9*, 628–635.

[79] Ravel, B.; Newville, M. *Journal of Synchrotron Radiation* **2005**, *12*, 537–541.

[80] Tomic, S. *et al. Council for the Central Laboratory of the Research Councils* **2005**, 1–10.

[81] Sing, K. S. W. *Pure and Applied Chemistry* **1985**, *57*, 603–619.

[82] Llewellyn, P. L. *et al. Langmuir* **1993**, *9*, 1852–1856.

[83] Suzuki, T.; Okuhara, T. *Microporous and Mesoporous Materials* **2001**, *43*, 83–89.

[84] Walendziewski, J.; Trawczyński, J. *Industrial and Engineering Chemistry Research* **1996**, *35*, 3356–3361.

[85] Ogunbadejo, B. A. *et al. Catalysis Today* **2015**, *243*, 109–117.

[86] Zibrowius, B.; Löffler, E.; Hunger, M. *Zeolites* **1992**, *12*, 167–174.

[87] Benamor, T. *et al. Microporous and Mesoporous Materials* **2012**, *153*, 100–114.

[88] de Oliveira, M. S. M. *et al. Materials Research* **2019**, *22*.

[89] Bare, S. R. *et al. Journal of Physical Chemistry C* **2011**, *115*, 5740–5755.

A. Additional XAS plots

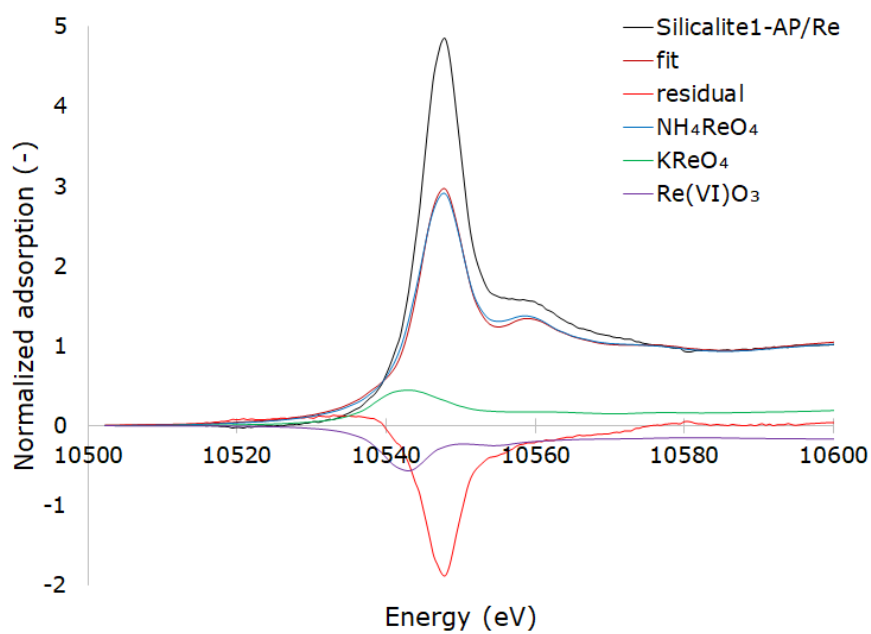## A.1   Linear combination fittings of all samples

Figure A.1: Linear combination fitting of a rhenium introduced Silicalite-1 (Silicalite1-AP/Re).
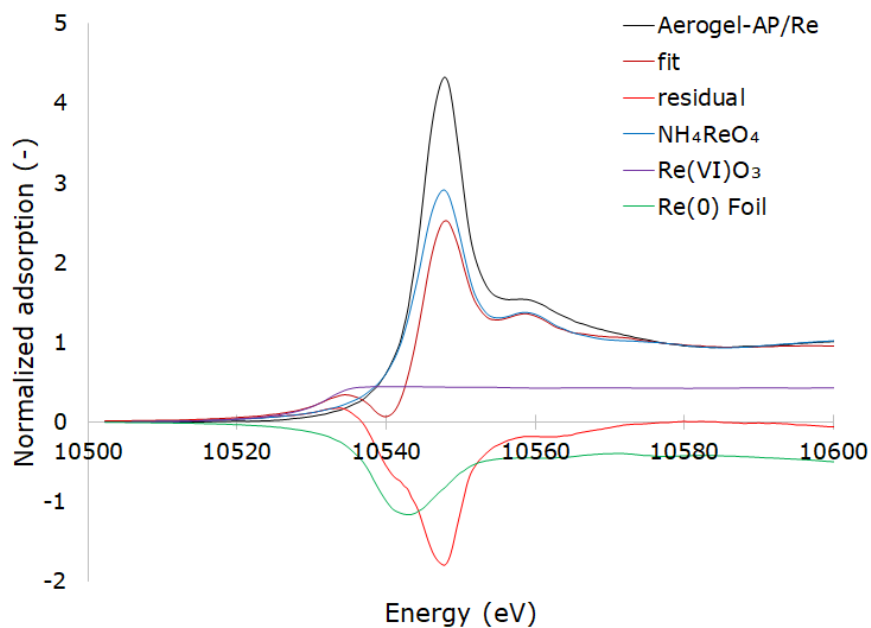
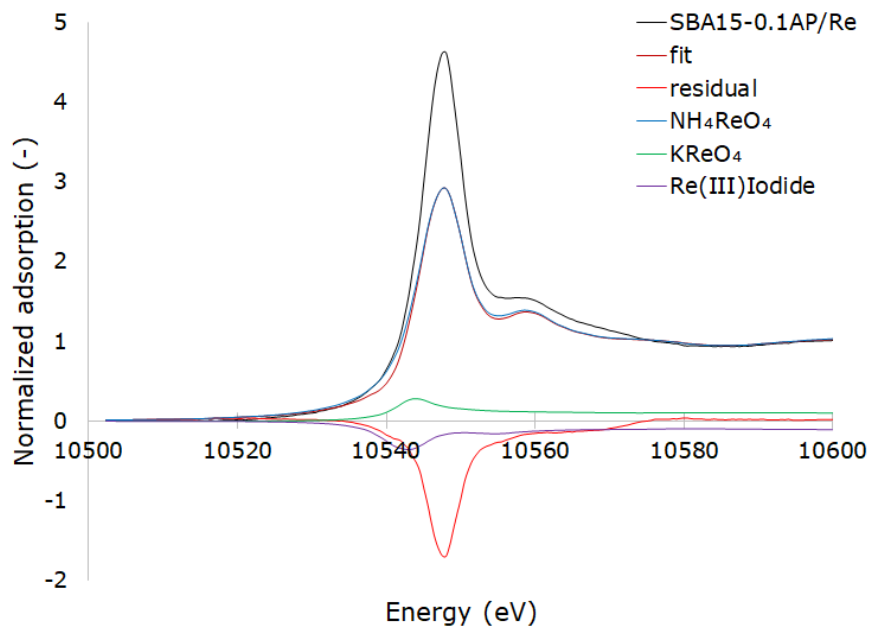**Figure A.2:** Linear combination fitting of a rhenium introduced silica aerogel (Aerogel-AP/Re).
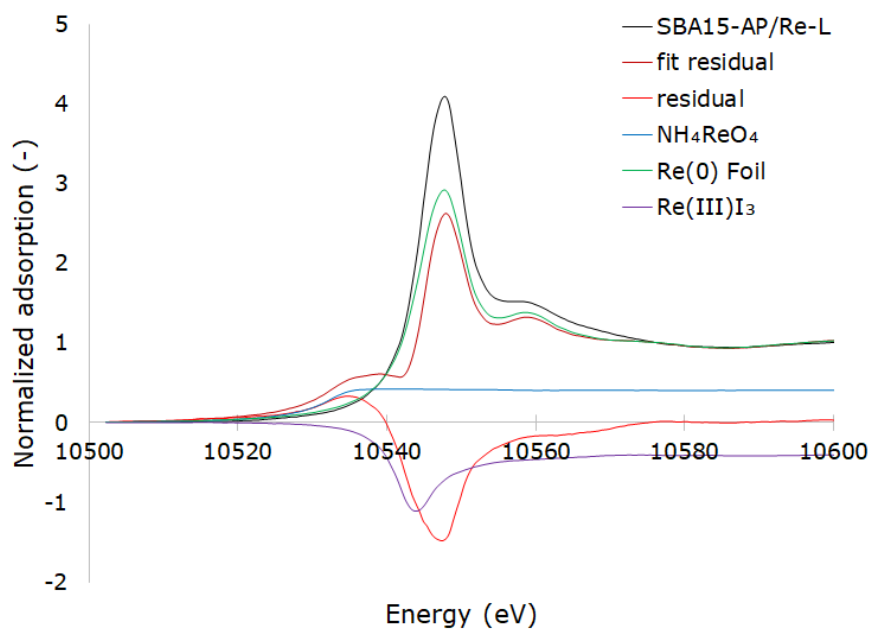

Figure A.3: Linear combination fitting of a rhenium introduced SBA-15 (SBA15-0.1AP/Re).

II

Figure A.4: Linear combination fitting of a rhenium introduced SBA-15 (SBA15-AP/Re-L).
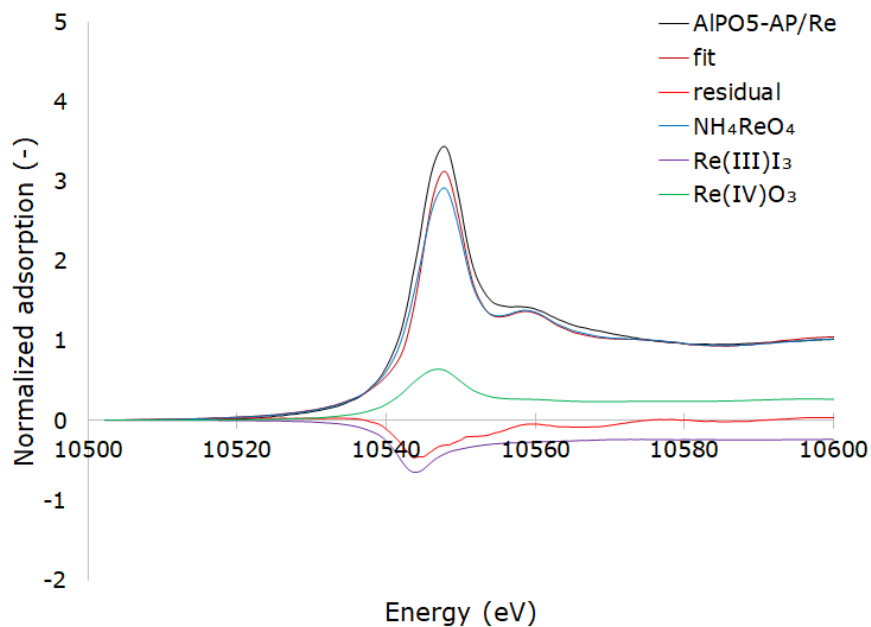

Figure A.5: Linear combination fitting of a rhenium introduced AlPO5 (AlPO5-AP/Re).
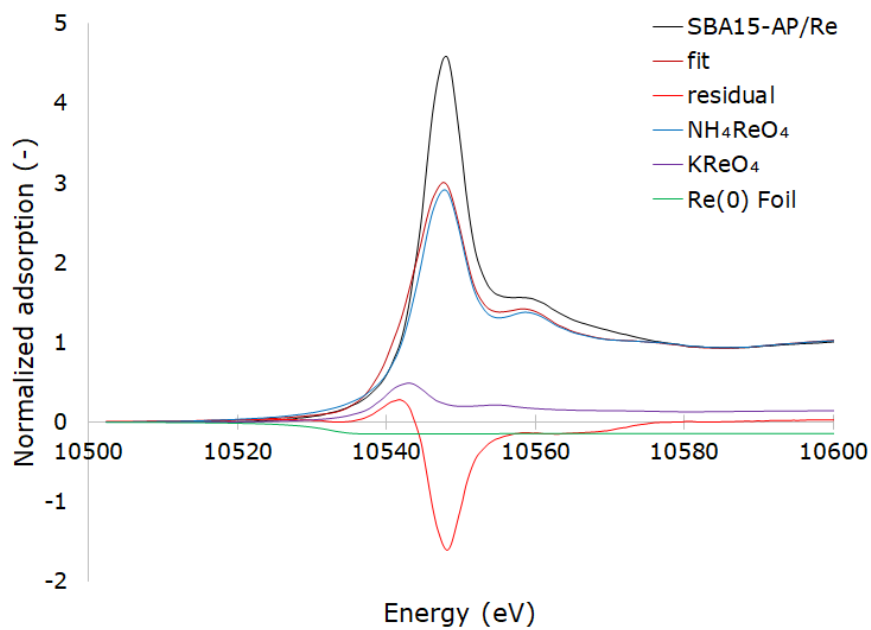
III

Figure A.6: Linear combination fitting of a rhenium introduced SBA-15 (SBA15-AP/Re).